

Numerical simulations of dwarf galaxies in the Fornax Cluster

Michele Mastropietro



university of
groningen

Numerical simulations of dwarf galaxies in the Fornax Cluster

PhD thesis

to obtain the degree of PhD at the
University of Groningen
on the authority of the
Rector Magnificus Prof. C. Wijmenga
and in accordance with
the decision by the College of Deans.

This thesis will be defended in public on

Friday 1 October 2021 at 14:30 hours

by

Michele Mastropietro

born on 14 September 1988
in Pisa, Italy

Supervisors

Prof. M. Biehl
Prof. R. F. Peletier
Prof. S. De Rijcke

Assessment Committee

Prof. Frazer Pearce
Prof. Arjen van der Wel
Prof. John McKean
Prof. Hugues Talbot

Written in 2021 by Michele Mastropietro.

Copyright © The template for the layout of this thesis was inspired by my colleague Sam Verstocken who used the template of the dissertation of Ken Arroyo Ohori, which was released into the public domain using the Creative Commons code. To view a copy of the code, visit:
<http://creativecommons.org/publicdomain/zero/1.0/>

Colophon Most of the figures were created using Ipe (Copyright © 1993-2020 Otfried Cheong). The source code of this thesis is available at:
<https://github.com/elehcim/phd-thesis>

Cover Above: full fledged simulation of a MoRIA galaxy falling into a simulated Fornax-like Cluster and a galaxy in the simulation box, both rendered with glnemo2 software (Lambert, 2012). Below: two jellyfish-like simulated galaxies in our simulation setup rendered with Splotch (Dolag et al., 2008).

This research was funded by the European Union's Horizon 2020 research and innovation programme under the Marie Skłodowska-Curie grant agreement N. 721463 to the SUNDIAL ITN network.



*To my professor of physics:
Mauro dell'Orso*

Acknowledgements

I'd like to thank first of all my professor Sven De Rijcke who believed in me doing a PhD in physics, since the first email in February 2017. I thank you Sven for showing me what science is, how can it be beautiful and difficult and how it is a fantastic gym to train in complex thinking, deep honesty and integrity. Thank you for the many things I learned from you and for being a mirror for me in our meetings, and always pushing me up even in my down moments. Thank you also because you showed me how to cope with work and life difficulties (especially in these pandemic times) in a very mature and ironic way.

The SUNDIAL project has been one of the nicest group of people I've ever met. I'll never forget the high quality of people, their professionalism, attention and kindness for all of us. Thanks to prof. Michael Biehl for your availability in this joint PhD journey, and to prof. Peter Tiño for showing me again the beauty of mathematics and that in the end it is always useful. Thank you prof. Reynier Peletier, a supervisor for all of us, for being always frank and available to investigate new ideas: it's been very inspiring seeing how you live education of young scientists and astronomical research as a calling. Thanks to all of the ESRs, the ones I had the privilege to work directly with: Marco, Abol, Bahar, and each one of the others: Caroline, Thanh, Nushkia, Shiv, Maria Angela, Aleke, Alex, Alan, Teymoor, Mohammad. All the best with your future. The collaboration among us ESRs ended up in very good friendships, and I'll always remember the many memorable moments we lived together (in Naples, La Palma, Ghent...).

I thank my fellow astronomer colleagues at S9, the ones who are there, the ones who left during these years and the ones who just arrived. I've learned so much from you academically and also how nice and beneficial is a happy work environment like the one you created. You all have been so welcoming and nice towards me, it's been an honour to work in the same place as you. The Belgian "old guard" and the others: Maarten, Seba, Wouter, Peter, Sam, Marjorie, Dries, Robbert, doctor Bert, Ilse, Arjen, Sharon, fellow Bert. Thanks to Ana and Goran for the many beautiful moments shared together in our common expats life. Thanks to Francesco and Martina and Aurora, Marco and Leonardo: I've learned so much from you all in these years we both were in Gent, much more than you think. Caro and Pablo, thank you for all the support, dinners, good food, sharing and friendship. Thank you office mates: Caroline, Sara, Anand and Yolan for the nice discussions, fruit breaks and activities done together. I also thank the group of the Maxwell Demons: wonderful people for playing minivoetbal with a fantastic team spirit. Thank you Daniela and Andrea, young fellows of survival in lockdown times: I had so many great moments with you. Thank you Shivangee, companion of the SUNDIAL adventure, of the office and of the life in Gent in the happy moments as well as in the difficult times of the PhD far from home: for your constant welcoming attitude and for the many times you asked how it was going on for me and carefully listening. It meant a lot. Thanks to Gianmarco (Jimmy), for showing me many times what true friendship means, and for being at the same time guest and host in our house in Belgium which became yours. I thank Angelos, a real "Sam" for me, in the sense of the Lord of the Rings: for helping me and pulling me out of my down moments with frank conversations (is it a perk of living in Frank Baurstraat? ;P), sharing insights about life, cooking delicious Greek food (with a sustainable amount of garlic) and being the fuel of many parties and gatherings, with a lot of attention to everyone.

Thanks to my friends at Sint Jacobs in Gent: Davide and Ana (with the newly arrived Bea), Maria and Esteban (with the newly arrived Jose), Caique and Daniela, Valeria, Joshi, Pawel, Eligio and Luca: thank you for the improvised dinners, singing, beers, holidays, sharings and deep friendship.

Many thanks to Pinco and the community of the Apostoline for helping me in many ways in these years: thank you for your wisdom and the constant example of free giving, gratuità.

I thank my family: babbo e mamma, grazie for your constant support and for always being there when I needed. Anto for the crystalline confrontations and the enormous sensitivity, Fra for the innumerable funny stories and deep thoughts. Nonna Lida per essere una roccia salda per tutti, always.

After this beautiful and hard journey of the PhD shared in many ways with all of you, my desire is to keep searching for my personal way to be fruitful. The presence of each of you has been very precious for keeping me oriented in this. Thank you.

Gent, 14th September 2021
Michele Mastropietro

Analysis of data and plots have been made possible thanks to open-source software: PYNBODY (Pontzen et al., 2013), NUMPY (Harris et al., 2020), SCIPY (Virtanen et al., 2020), PANDAS (Reback et al., 2020), MATPLOTLIB (Hunter & Elmegreen, 2004), ASTROPY (The Astropy Collaboration et al., 2018), STATMORPH (Rodriguez-Gomez et al., 2019).

Summary

Dwarf galaxies are the most numerous type of stellar systems in the Universe and due to their low mass, they are very sensitive to the surrounding environment. Because of this, they offer a privileged platform to study and isolate the different physical phenomena affecting galaxy observables. They can be used as probes to characterize the complex interplay between internal processes and the environment in which galaxies evolve.

We carried out simulations of the evolution of dwarf galaxies falling into a Fornax-like Cluster. We selected prototypical dwarf galaxies from the MoRIA suite of simulations and injected them one by one on different orbits. We were interested in following the journey of the galaxies into the cluster and characterize their size, star formation rate, gas and dark matter content, stellar dynamics and evolution, depending on the orbit and the initial mass at the time of orbital injection. To do so, we implemented the Moving Box simulation technique in our in-house simulation code. This allows us to simulate the dwarf-cluster interaction at high resolution while keeping an affordable run time.

We found that during infall, generally, galaxies undergo some “phase transition” happening mainly around pericenter passages. Some of the galaxies are effectively transformed into Ultra Diffuse Galaxies (UDG) while some others are allowed to be briefly identified as “jellyfish”. It is therefore possible to hypothesize that the jellyfish phenomenon is a relatively short transitory phase of a dwarf galaxy along its orbit, and it’s likely a precursor of the transformation of a dwarf galaxy into an UDG.

Serendipitously we realized that our simulations produce galaxies whose morphology is similar to a galaxy in the Fornax Cluster with a peculiar HI tail and an arrow-shaped stellar body oriented in different directions: NGC 1427A. Multiple formation scenarios have been proposed for this galaxy, but a consensus was still lacking in the literature. We identified that gaseous and stellar tails pointing in different directions are explainable given that they are subject to different environmental effects (ram-pressure stripping and tidal forces). This idea finds support in our simulations and we developed a procedure to quantitatively assess the properties of simulated galaxies from a catalogue of simulations. We were also able to provide some falsifiable predictions on the position of the galaxy with respect to the center of the Cluster and its projected orbital direction.

Finally, we have contributed to the development of a technique to study low dimensional-manifolds in the simulations. We found that the technique can be very useful to isolate the physical properties of filaments

in N-body simulations. In particular we concentrated on the analysis of gaseous tails of simulated jellyfish galaxies with the aim of investigating regions of recent star formation and mixing between the galactic gaseous material and the hot gas of the cluster.

Samenvatting

Dwerggalaxieën zijn het talrijkste type sterrenstelsels in het heelal en door hun lage massa zijn zij zeer gevoelig voor hun omgeving. Daarom bieden zij een bevorrecht platform om de verschillende fysische fenomenen die de waarneembare eigenschappen van sterrenstelsels beïnvloeden, te bestuderen en te isoleren. Ze kunnen worden gebruikt als laboratoria om de complexe wisselwerking tussen interne processen en de omgeving waarin galaxieën evolueren te onderzoeken en te karakteriseren.

Wij hebben simulaties uitgevoerd van de evolutie van verschillende dwerggalaxieën die in een Fornax-achtige Cluster vallen. We selecteerden prototypische dwerggalaxieën uit de MoRIA-simulatiesuite en injecteerden ze één voor één op verschillende banen. We waren geïnteresseerd in het volgen van de reis van de melkwegstelsels in de cluster en het karakteriseren van hun grootte, stervormingssnelheden, hun inhoud aan gas en donkere materie, hun interne dynamica en hun evolutie, afhankelijk van de baan en de initiële massa op het moment van de injectie in de baan. Daartoe hebben wij de Moving-Box-simulatietechniek aangepast aan onze noden en geïmplementeerd in onze eigen simulatiecode. Dit maakt het mogelijk om de dwerg-clusterinteractie met zeer hoge resolutie te simuleren binnen een haalbare totale runtijd.

We ontdekten dat tijdens de inval, over het algemeen, melkwegstelsels enkele faseovergangen ondergaan, die voornamelijk plaatsvinden bij peri-centerpassages. Sommige van de stelsels worden getransformeerd in Ultra Diffuse Galaxies (UDG), andere worden kortstondig geïdentificeerd als “jellyfish”. Het is daarom mogelijk te veronderstellen dat het “jellyfish”-fenomeen een relatief korte overgangsfase is van een dwergmelkwegstelsel langs zijn baan, en waarschijnlijk een voorloper is van de transformatie van een dwerggalaxie in een UDG.

Dankzij enige serendipiteit realiseerden we ons dat onze simulaties melkwegstelsels produceren waarvan de morfologie vergelijkbaar is met die van een welbepaald melkwegstelsel in de Fornax Cluster met een eigenaardige HI staart en een pijlvormig stellair lichaam die in verschillende richtingen georiënteerd zijn: NGC 1427A. Voor dit sterrenstelsel zijn meerdere formatiescenario's voorgesteld, maar in de literatuur was er nog geen consensus over. Wij stelden vast dat gasvormige en stellaire staarten die in verschillende richtingen wijzen verklaarbaar zijn, aangezien zij onderhevig zijn aan verschillende omgevingseffecten (ramdruk en getijdekrachten). Dit wordt ondersteund door onze simulaties en wij hebben een procedure ontwikkeld om de eigenschappen van gesimuleerde melkwegstelsels kwantitatief te beoordelen aan de hand van een catalogus van simulaties. We

waren ook in staat om enkele falsifieerbare voorspellingen te doen over de positie van het melkwegstelsel ten opzichte van het centrum van de Cluster en zijn geprojecteerde baanrichting.

Tenslotte hebben we bijgedragen aan de ontwikkeling van een techniek om laagdimensionale manifolds in simulaties te bestuderen. We ontdekten dat de techniek zeer nuttig kan zijn om de fysische eigenschappen van filamenten in N-body-simulaties te isoleren. In het bijzonder hebben we ons geconcentreerd op de analyse van gasvormige staarten van gesimuleerde ‘jellyfish’-sterrenstelsels met het doel regio’s van recente ster-vorming en ver menging tussen het galactische gasachtige materiaal en het hete gas van de cluster te onderzoeken.

Sommario

Le galassie nane sono i sistemi stellari più numerosi dell’Universo e, a causa della loro piccola massa, sono molto sensibili all’ambiente che sta loro intorno. Per questo motivo, offrono una piattaforma privilegiata per studiare e isolare i diversi fenomeni fisici che influenzano le caratteristiche osservabili delle galassie. Possono essere utilizzati come sonde per caratterizzare la complessa interazione tra i processi interni e l’ambiente in cui le galassie si evolvono.

Abbiamo effettuato simulazioni dell’evoluzione delle galassie nane che cadono in un ammasso con caratteristiche simili a quello della Fornace. Con alcune galassie prototipali, selezionate dalla suite di simulazioni MORIA, le abbiamo lanciate su diverse orbite. È di interesse scientifico seguire il viaggio delle galassie nell’ammasso e caratterizzare le loro dimensioni, la formazione stellare, il contenuto di gas e materia oscura, la dinamica stellare e la sua evoluzione, a seconda dell’orbita e della massa iniziale al momento dell’iniezione orbitale. Per fare ciò, abbiamo implementato la tecnica di simulazione chiamata “Moving Box” e inclusa nel codice sviluppato negli anni nel nostro dipartimento. Questo ci ha permesso di simulare l’interazione tra la galassia nana e l’ammasso ad alta risoluzione con un tempo di calcolo accettabile.

Abbiamo trovato che durante l’orbita, generalmente, le galassie subiscono alcune “transizioni di fase” che avvengono principalmente attorno al passaggio per il pericentro. Alcune galassie vengono effettivamente trasformate in Galassie Ultra Diffuse (UDG), mentre altre possono essere identificate brevemente come “galassie medusa” (jellyfish). È quindi possibile ipotizzare che il fenomeno delle galassie medusa sia una fase transitoria relativamente breve di una galassia nana lungo la sua orbita, e che costituisca probabilmente un precursore della trasformazione di una galassia nana in una UDG.

Abbiamo notato che le nostre simulazioni producono galassie la cui morfologia è simile a quella di una galassia dell’ammasso della Fornace con una peculiare coda HI e un corpo stellare a forma di freccia, orientate in diverse direzioni: la NGC 1427A. Di questa galassia sono stati proposti molteplici scenari di formazione, ma manca ancora un consenso in letteratura. Abbiamo identificato che le code gassose e stellari che puntano in direzioni diverse sono spiegabili dato che ognuna è soggetta a diversi effetti ambientali (pressione e forze di marea). Questa idea trova supporto nelle nostre simulazioni. Abbiamo quindi sviluppato una procedura per valutare quantitativamente le proprietà delle galassie simulate partendo

da un catalogo di simulazioni. Siamo stati anche in grado di fornire alcune previsioni falsificabili sulla posizione della galassia rispetto al centro dell'ammasso e la sua direzione orbitale proiettata.

Infine, abbiamo contribuito allo sviluppo di una tecnica per studiare le varietà (manifold) con una dimensionalità bassa che si possono trovare in dataset come quelli delle simulazioni. Abbiamo scoperto che questa tecnica può essere molto utile per isolare le proprietà fisiche dei filamenti nelle simulazioni a N corpi. In particolare, ci siamo concentrati sull'analisi delle code gassose delle galassie medusa simulate, con l'obiettivo di indagare le regioni di recente formazione stellare e di mescolamento tra il materiale gassoso galattico e il gas caldo dell'ammasso.

Contents

1	Introduction	1
1.1	Falling into a galaxy cluster	2
1.2	Motivations	4
1.3	This work	4
2	Simulations	9
2.1	General assumptions	9
2.2	N-Body systems	12
2.3	Smoothed Particles Hydrodynamics	14
2.4	Dwarf galaxies models	16
2.5	Moving box	22
2.6	Simulating the Fornax cluster environment	30
3	Simulation results	33
3.1	Becoming an Ultra Diffuse Galaxy (UDG)	35
3.2	Star formation	44
3.3	Colour Magnitude	50
3.4	H α size mass relation during infall	50
3.5	Kinematics	56
4	A tale of two tails: on the formation of NGC 1427A	65
4.1	Observed properties of NGC 1427A	67
4.2	Simulations	70
4.3	Constraining the orbital phase of NGC 1427A	70
4.4	Discussion	81
4.5	Conclusions	84
5	Low-dimensional manifolds	87
5.1	Introduction	87
5.2	Methodology	89
5.3	Experiments on a simulated jellyfish galaxy	92

Contents

5.4	A multi-manifold analysis of a dwarf jellyfish galaxy	95
5.5	Evolution of quantities along the jellyfish tails	97
6	Conclusions and future work	105
6.1	Conclusions	105
6.2	Ongoing research efforts	106

Introduction

1

The Dark Energy plus Cold Dark Matter (Λ CDM) cosmological model is the current “standard model” which satisfactorily reproduces the present-day observations of the large scale structure of the Universe, of the Cosmic Microwave Background (CMB) and of supernovae indicating an accelerating expansion of the Universe (Riess et al., 1998). According to Λ CDM, the Universe was formed 13.8 Gyr ago, through the so called Big Bang, when the Universe was a hot plasma. After a phase of sudden expansion, the consequent cooling allowed the radiation to decouple from the ordinary matter. The last radiation scattered before the Universe became transparent is called the Cosmic Microwave Background and it is observable now in the microwave range as an uniformly distributed radiation of a black body of 2.7 K. Since black body spectra are produced by opaque objects CMB brings the information that the early Universe was opaque (Ryden, 2003).

However, at the beginning of the XX century, various measurements found that the amount of visible (baryonic) matter was not enough to justify observations of galaxy motion and their rotation. Zwicky (1933) first recognized the discrepancy and the missing matter by observing the rotation velocity of the galaxies in the outskirts of the Coma cluster (Zwicky, 1937). He therefore hypothesized the existence of dark matter, a kind of matter which does not interact with the electromagnetic forces but only with gravity. All these observations showed that in the Universe, the amount of dark matter is around five to six times more than baryonic matter. Another observational fact coming from supernovae, is the accelerating expansion of the Universe. The current accepted model is the presence of an large scale unknown form of energy, called Dark Energy (or Λ), which constitutes around 68% of all the mass-energy content of the Universe. The Λ CDM model also assumes that the dark matter is “cold”, i.e. it has negligible thermal velocity and does not suppress structure formation on any scale relevant for galaxy formation (Bullock & Boylan-Kolchin, 2017). Baryonic and dark matter gravitationally collapsing slowly formed filaments along which gas could become dense enough to create self-supporting gravitational systems cradle of stars: the first galaxies. These filaments

have been observed in large surveys like the Sloan Digital Sky Survey (SDSS), see Figure 1.1.

The study of galaxies has seen its development only very recently. Less than one century ago, current recognized galaxies were thought to be small luminous clouds (and thus called *nebulae*) belonging to our Galaxy, the Milky Way, the only known Galaxy. In 1923 Edwin Hubble, measuring the distance of the *nebulae* by observing their variable stars Cepheids, from the observatory of Mount Wilson in California, realized they were systems far away from the Galaxy (Hubble, 1929). His observations have completely changed the view of the Universe. The scientific research on galaxies took off from Hubble's works and even the morphological classification of galaxies took his name.

In this thesis we are particularly interested in small galaxies, the so called *dwarf galaxies*. They are the most numerous type of stellar systems in the Universe and due to their low mass, they are very sensitive to the surrounding environment. For this they offer a privileged platform to study and isolate the different physical phenomena affecting galaxies observables. They can be used as probes to characterize the complex interplay between internal processes and the environment in which they evolve.

1.1 Falling into a galaxy cluster

The evolution of galaxies in dense environments has been shown to be markedly different from that of more isolated galaxies, with mass being a prominent factor in determining how profoundly environmental influences affect a galaxy (Boselli & Gavazzi, 2006; Grossi, 2018). The well-known morphology-density relation, according to which early-type galaxies are mostly found in high-density environments (Dressler, 1980; Dressler et al., 1997), is especially pronounced for low-mass systems, such as dwarf galaxies (McConnachie, 2012). Indeed, while actively star-forming late-type dwarf galaxies are found almost exclusively in low-density environments, truly isolated quiescent early-type dwarf galaxies, on the contrary, are exceedingly rare (Binggeli et al., 1990; Karachentseva et al., 2010; Geha et al., 2012).

An effective way of shutting down the star formation in a galaxy is to rob it of the raw material for building stars: gas. When a galaxy enters on an orbit in a galaxy cluster or group, it is subjected to the tidal forces of the cluster potential and of its galaxies. Its interstellar medium experiences the ram pressure (Gunn & Gott, 1972), basically a supersonic “headwind”, exerted by the intracluster medium. The combination of the two effects can lead to interesting tail geometries like the one shown in Figure 1.2.

Ram pressure is a well known phenomenon and many studies have been devoted to simulating its effects on galaxies (e.g.: Mori & Burkert, 2000; Mayer et al., 2006; Roediger & Brüggen, 2008; Roediger et al., 2015; Steinhauser et al., 2016; Yun et al., 2019; Steyrlleithner et al., 2020). If the ram pressure is sufficiently vigorous, the galaxy's diffuse interstellar medium can be pushed out of its gravitational well, forming a tail of escaping H_I gas in the galaxy's wake. The much more clumpy molecular gas is not as easily removed by the ram pressure and remains behind while being consumed by star formation (Abramson & Kenney, 2014; Lee et al., 2017; Wang et al., 2020). Inside the tail, gas can cool and form knotty condensations, leading to a complex stellar system, with a head consisting of the galaxy's stellar body (and what remains of its gas) and a tail of twisting swirls of stripped gas, beaded with knots of star formation.

The term *jellyfish galaxies* (Ebeling et al., 2014) neatly fits this description. The term applies to galaxies with star formation activity within the gaseous tails. Jellyfish galaxies exhibit tentacles of material that appear to be stripped from the galaxy body (Poggianti et al., 2017, 2019; Ramatsoku et al., 2020). Signatures of the newly born stars within those gaseous tails are easily found observationally in UV or blue images (Cortese et al., 2007; Smith et al., 2010).

As already noted by many authors (Mayer et al., 2001, 2007; Mastropietro et al., 2005) ram pressure stripping (Gunn & Gott, 1972; Roediger & Brüggen, 2008; Roediger et al., 2015) and tidal interaction can cooperate to change the morphology of the galaxy. Recent studies using cosmological simulations deal with dwarf galaxies infalling into a galaxy cluster. Smith et al. (2015) evolve a large population of early type galaxies and take into account tidal interactions and harassment effects but with no gas physics.

Using the cosmological simulation TNG100, Yun et al. (2019) visually inspect infalling galaxies in simulated clusters to characterise jellyfish galaxies. Interestingly, they also found a dearth of jellyfish galaxies within one fourth of the cluster virial radius. This is consistent with current catalogues of cluster galaxies (Lisker et al., 2006; Venhola et al., 2019).

De Rijcke et al. (2010), from dynamical models of the Fornax Cluster as a whole, could explain the radially increasing late-to-early-type dwarf ratio in the cluster. In the Virgo cluster, Boselli et al. (2008) highlights that low mass galaxy at the first infall lose most of their H_I and are quenched. After, these objects become red and quiescent. Ruggiero & Lima Neto (2017), using RAMSES simulations constrain how much of the gas disc of a Milky Way-like galaxy will be converted into stars and how much of it will be lost, after a single cluster crossing. They find star formation bursts on infall and remark that the survival of the galaxy is independent on the

1 Introduction

galaxy orbit and cluster mass if the cluster has a cool core. The removal of the gas has been studied for example by Calura et al. (2020) who follow the evolution of a massive pressure-confined, star-forming neutral gas cloud moving through a hot intracluster medium (ICM). They find that generally cold clouds survive with a final cold gas fractions generally greater than 0.75 on time-scales of the order of 1 Gyr. But while the removal of cold gas is a quick process (a time scale ≤ 1 Gyr), a few Gyr are required to quench the galaxy and reach the red sequence (Cortese & Hughes, 2009).

1.2 Motivations

In this work we would like to follow the dwarfs' journey into a Fornax-like cluster environment by tracking their star formation rates, their size, stellar distribution, and stellar dynamics. We would like to investigate the two major effects on a dwarf galaxy falling into a cluster: tidal stirring and ram-pressure stripping.

Venhola et al. (2018) show that number density of dwarfs in the Fornax cluster decreases going towards the centre of the cluster. A possible scenario suggests that some infalling galaxies do not survive the passage around the centre of the cluster. Further investigation is needed to assess whether the disrupted galaxies then contribute to the Intra-Cluster Light (ICL) or become Ultra Diffuse Galaxies (UDG) or both.

One of the motivations for this work is trying to shed light on how easily dwarfs are being dissolved around the cluster centre, and then create a catalogue/database to allow the comparison of the simulation output with recent and ongoing surveys such as the SAMI High Resolution Survey of Fornax Dwarf Galaxies, (Owers et al., 2019; Scott et al., 2018) the Fornax Deep Survey (Venhola et al., 2018), and the Fornax MeerKAT survey (Loni et al., 2021).

We would also try to investigate the applicability of topological analysis with identification of low-dimensional manifolds as a method to analyze the tails of a simulated jellyfish galaxy.

1.3 This work

To the best of our knowledge our work is the first to apply the Moving Box technique (see Section 2.5) to a galaxy cluster setup, using high definition simulations. In comparison to earlier works our simulations take into account gas-rich realistic late-type galaxies. To our knowledge none of them include such a high definition simulation starting from realistic late-type

dwarf models. In Chapter 2 we introduce the techniques used for this kind of simulations and in Chapter 3 we present the main results. A catalogue of results of simulations can also be found online: <http://moria-fornax.herokuapp.com/>.

In Chapter 4 (Mastropietro et al., 2021) we take advantage of our simulation setup to propose a formation scenario for the galaxy NGC 1427A in the Fornax Cluster, including some falsifiable predictions. Chapter 5 (Canducci et al., 2022) we show the fruits of the collaboration with the Birmingham node within the SUNDIAL Innovative Training Network which has lead to the formulation of new techniques usable by astronomers to study low-dimensional manifolds in simulated “jellyfish galaxies”. Chapter 6 gives an overview of the work and briefly present some ongoing research efforts.

1 Introduction

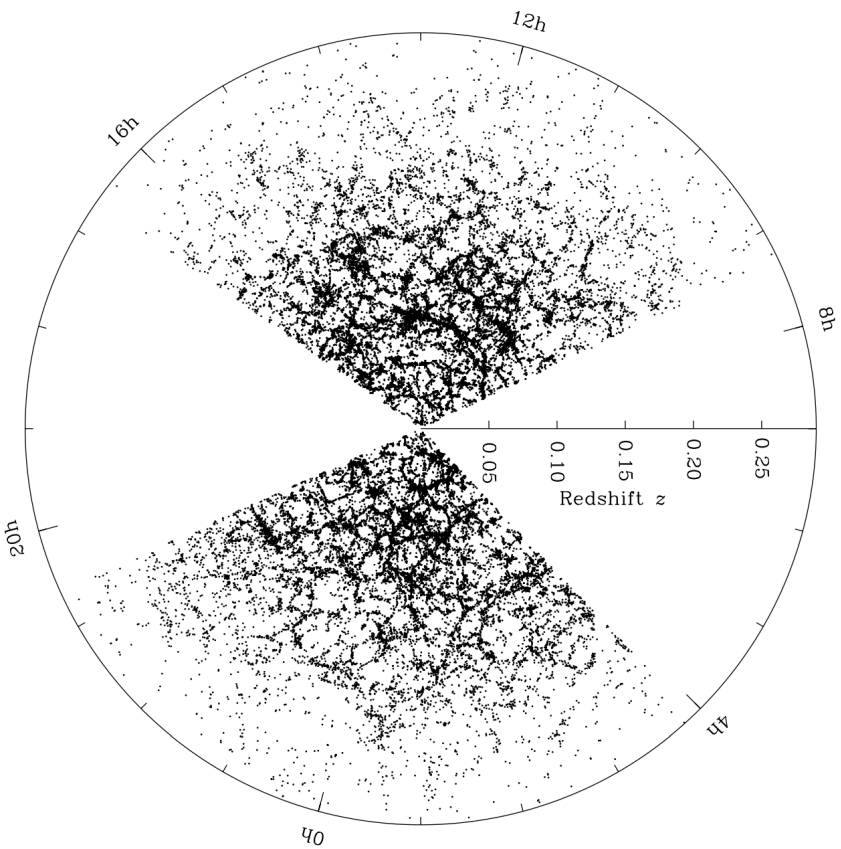


Figure 1.1: From Zehavi et al. (2011), it is shown the SDSS main galaxy sample, with galaxy within ± 1.25 deg of the celestial equator, in the north Galactic cap. The large supercluster at $z \sim 0.08$, cutting across the center of the Northern cap is the “Sloan Great Wall” the largest coherent structure detected in the SDSS (Gott III et al., 2005).

Ram pressure stripping + Tidal interactions

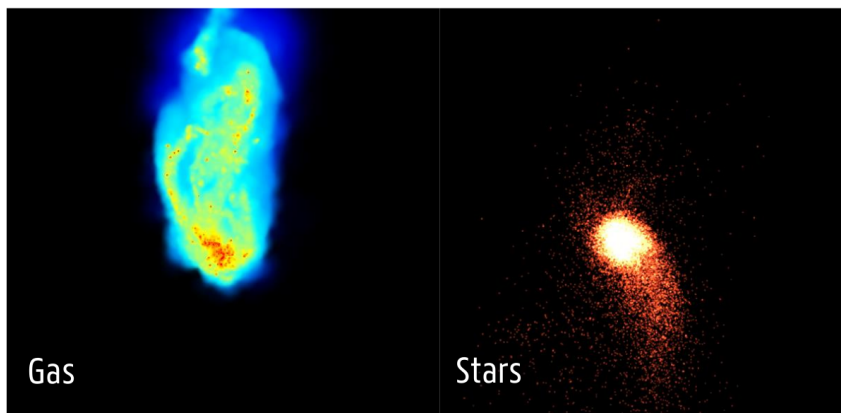


Figure 1.2: On the left the gaseous component of a simulated dwarf galaxy, color coded with projected density. On the right the stellar particles of the same galaxy. Different physical processes (of ram pressure stripping and tidal interactions) affecting the galaxy can lead to the creation of the curious effect of gaseous and stellar tails oriented in almost opposite directions.

Numerical simulations have emerged as a new tool to investigate nature, alongside theory and experiments. This is particularly valid for astronomy where, unlike laboratory-based disciplines, astronomers may not exert full control over their study objects (Heng, 2014).

Computer simulations are essentially tools to solve complex systems of equations which are intractable with analytic techniques, or only tractable with very coarse level of approximation (Springel, 2015). This allows an unprecedentedly detailed exploration of the consequences of assumed models for physical systems. In this sense, the reproduction of observations through computer simulations is a way to validate scientific hypotheses. The main mathematical model used in galaxy simulations is the fluid model, a branch of continuum mechanics which deals with materials represented as continuous mass as opposed to discrete particles. In fact, we are not interested in the motion of each molecule in detail, rather we will use a statistical approach. In the following we will be dealing with hydrodynamics, given that the main components of galaxies are successfully described in terms of fluids.

2.1 General assumptions

We will assume the Cold Dark Matter (CDM) paradigm (in a Λ CDM cosmology), which has gained consensus among the scientific community throughout the years even if up to now, there has been no detection of it (see e.g. Einasto, 2010, for an extensive and historical overview). In a dwarf galaxy simulation three kind of fluids are generally taken into account, each following different models: dark matter, gas and star. The latter two are so called *baryonic* matter.

Dark matter is hypothesized to consist of small particles that are orders of magnitude smaller than the typical distance scales in our galaxies, so that they constitute a collisionless fluid. Similarly, the cross section of stars is small compared to galactic scales, and makes them collisionless as

well. Stars, though, affect the gas by pumping energy and metals into their surroundings. Dark matter and stars are therefore sensitive only to gravity, a weak, conservative, long-range force which is caused by a generally smooth potential.

On the other hand, as we shall see, gas is collisional and its behaviour at any point is affected by short-range interactions, whose modeling requires other assumptions (see below Sections 2.4.2 and 2.4).

2.1.1 Boltzmann Equation - Equations of motion

The Boltzmann Equation is the general equation which governs the behaviour of a fluid. From it, the equations of motions can be derived and solved to assess the evolution through time of the fluid.

For simplicity, in this section we assume a single-species fluid, a generalization to multiple species being straightforward. For each point of the fluid we would like to know its position and velocity. Following a statistical approach, at any given time t we can write the distribution function

$$f(\mathbf{x}, \mathbf{u}, t) \quad (2.1)$$

which describes the number of molecules lying within a spatial volume $d^3\mathbf{x}$ about \mathbf{x} and with velocity lying in a velocity-space volume $d^3\mathbf{u}$ about \mathbf{u} . These elementary volumes $d^3\mathbf{x}$ and $d^3\mathbf{u}$ are finite volume elements which are large enough to contain a very large number of molecules and still small enough to be considered as infinitesimal when compared to macroscopic dimensions (Huang, 1987).

The number density $n(\mathbf{x}, t)$ in physical space is obtained by integrating over all possible velocities at a position \mathbf{x} :

$$n(\mathbf{x}, t) = \int f(\mathbf{x}, \mathbf{u}, t) d^3\mathbf{u}. \quad (2.2)$$

The spatial density is then simply $\rho(\mathbf{x}, t) = m_p n(\mathbf{x}, t)$, where m_p is the mass of the elementary molecule of the fluid. From this we can define an average value in the position space of a generic quantity $A(\mathbf{x}, \mathbf{u}, t)$:

$$\bar{A}(\mathbf{x}, t) = \frac{1}{\rho(\mathbf{x}, t)} \int A(\mathbf{x}, \mathbf{u}, t) m_p f(\mathbf{x}, \mathbf{u}, t) d^3\mathbf{u} \quad (2.3)$$

It is useful to define the averaged (*bulk*) velocity \mathbf{v} as:

$$\mathbf{v}(\mathbf{x}, t) \equiv \bar{\mathbf{u}}(\mathbf{x}, t) = \frac{1}{\rho(\mathbf{x}, t)} \int \mathbf{u}(\mathbf{x}, \mathbf{u}, t) m_p f(\mathbf{x}, \mathbf{u}, t) d^3\mathbf{u} \quad (2.4)$$

For each elementary spatial volume d^3x we can write the local velocity as the sum: $\mathbf{u} = \mathbf{v} + \mathbf{w}$, where \mathbf{v} is the average particle velocity and \mathbf{w} a term corresponding to the random movement of the particle with respect to the bulk flow velocity.

Assuming that the microscopic particles do not collide, the number density in phase space is conserved in time, i.e. no particles are destroyed or created out of nothing in phase space. This gives immediately the collisionless Boltzmann equation (a.k.a. Vlasov equation):

$$\frac{df}{dt} = \frac{\partial f}{\partial t} + \mathbf{u} \frac{\partial f}{\partial \mathbf{x}} + \mathbf{a} \frac{\partial f}{\partial \mathbf{u}} = 0, \quad (2.5)$$

where $\mathbf{a} = \frac{d\mathbf{u}}{dt}$ is the acceleration.

In the case of collisions, the Boltzmann equation is modified to:

$$\frac{df}{dt} = \left. \frac{df}{dt} \right|_c, \quad (2.6)$$

where the right term represents discontinuous motion of molecules through phase space because of collisions.

Euler's equations

After computing the zeroth, first and second velocity moments of equation (2.6) —by multiplying by m_p , $m_p \mathbf{u}$ and $m_p \|\mathbf{u}\|^2$ and by integrating over the entire velocity space— it is possible to retrieve the equations of hydrodynamics (continuity, momentum and energy) (Huang, 1987, and Vandenbroucke (2016) for an extended derivation).

In the following we make the assumption that collisions do not create or destroy molecules at a fixed position (they only shift them in velocity space), they conserve momentum and energy. Consequently in the case of the continuity, momentum and energy equations the right-hand side of equation (2.6) vanishes. We also neglect diffusive terms (heat conduction and viscous stress tensor) which are often small compared to dynamical effects (an important exception though are shocks, for example).

The hydrodynamical equations (a.k.a. Euler equations) are therefore:

$$\begin{aligned} \frac{d\rho}{dt} &= \frac{\partial \rho}{\partial t} + \mathbf{v} \cdot \nabla \rho = -\rho \nabla \cdot \mathbf{v}, \\ \frac{d\mathbf{v}}{dt} &= \frac{\partial \mathbf{v}}{\partial t} + (\mathbf{v} \cdot \nabla) \mathbf{v} = \mathbf{a} - \frac{\nabla p}{\rho}, \\ \frac{d\varepsilon}{dt} &= \frac{\partial \varepsilon}{\partial t} + \mathbf{v} \cdot \nabla \varepsilon = -\frac{p}{\rho} \nabla \cdot \mathbf{v}. \end{aligned} \quad (2.7)$$

2 Simulations

where we defined the pressure as

$$p(\mathbf{x}, t) = \rho \frac{1}{3} \text{tr}(\mathbf{w}\mathbf{w}^T) = \rho \frac{1}{3} \|\mathbf{w}\|^2,$$

assuming an isotropic medium, and the specific internal energy (internal energy per unit mass) as

$$\varepsilon(\mathbf{x}, t) = \frac{1}{2} \|\mathbf{w}\|^2.$$

These definitions implicitly fix an equation of state

$$p = \frac{2}{3} \rho \varepsilon. \quad (2.8)$$

Usually a more general equation of state is assumed $p = (\gamma - 1)\rho\varepsilon$. For a monoatomic gas: $\gamma = \frac{5}{3}$, so equation (2.8) is returned.

Also, the internal energy is related to the temperature via the Boltzmann constants k_B :

$$\varepsilon = \frac{1}{\gamma - 1} \frac{k_B T}{m_p}.$$

For a monoatomic gas $\varepsilon = \frac{3}{2} \frac{k_B T}{m_p}$.

Equations (2.7) describe the dynamics of a perfect monoatomic gas.

2.1.2 Gravity

Acceleration in each phase-space position is due to the gravitational field.

In case of self-gravity the source of the acceleration field is the mass density $\rho(\mathbf{x}, t)$:

$$\nabla \cdot \mathbf{a} = -4\pi G \rho(\mathbf{x}, t). \quad (2.9)$$

The gravitational potential $\mathbf{a} = -\nabla\Phi$ can therefore be found through the Poisson's equation:

$$\nabla^2 \Phi(\mathbf{x}, t) = 4\pi G \rho(\mathbf{x}, t). \quad (2.10)$$

2.2 N-Body systems

The direct numerical solution of the Boltzmann equation, a non-linear PDE in seven dimensions, is not feasible. It is interesting to note that in this description the particles have basically completely vanished and have been replaced with a continuum fluid description. In order to solve

the Boltzmann equation (or equivalently the Euler's equations), we represent the fluid by N mass elements (particles), that are conceptually different from the microscopic particles (molecules) constituting the fluid. The main idea is to discretize the equations above introducing particles. These are therefore fiducial macro particles that sample the phase-space in a Monte-Carlo fashion (Springel, 2015). Thus, in practice an N -body method is a tool for solving the Boltzmann equation.

The equation of motion for particles, following equations (2.10) can be written as follows:

$$\mathbf{a}_i = -\nabla_i \Phi(\mathbf{x}_i), \quad (2.11)$$

$$\Phi(\mathbf{x}_i) = -G \sum_{j=1}^N \frac{m_j}{\sqrt{(\mathbf{x}_i - \mathbf{x}_j)^2 + \epsilon^2}}. \quad (2.12)$$

where we introduced the softening length ϵ , effectively using a Plummer sphere potential for each particle (Plummer, 1911). It's worthwhile to note, though, that particles interact with each other as a point mass and a Plummer potential, not as Plummer spheres with each other.

The purpose of the force softening is to avoid the numerical expense that would be needed to integrate the orbits with sufficient accuracy around the singularity in the $\sim 1/r$ potential. Also, if two particles get very close their gravitational attraction will explode, leading to the possibility of the formation of bound particle pairs, strongly violating the collisionless behaviour. The softening length is also called force resolution because we cannot resolve gravitational forces below that distance. The value of the gravitational resolution is important when trying to follow the collapse of dense gas clouds where star formation is about to occur, as we shall see in Section 2.4.1. In our simulations we use a softening length of $\epsilon = 30$ pc. An estimate of this smoothing length is obtained by requiring that in the simulated gas clouds with the highest density, ϵ is about equal to the average distance between the gas particles (Schroyen et al., 2013). Given that in the densest gas clouds star formation occurs at a density of $n \approx 100$ amu/cm³, when a galaxy is simulated with gas particles of $4000 M_\odot$, the average distance between the particles in that gas cloud will be of the order of 11 pc.

As Bate & Burkert (1997) and Springel (2005) discuss, in order for SPH to produce the correct results in problems involving self-gravity, the hydrodynamic smoothing length and gravitational softening length must always be less than the local *Jeans length* (see Section 2.4.1). However, a gravitational softening much smaller than the SPH smoothing length can lead to artificial convergence of SPH particles. This can be avoided if the force resolution is greater than the hydrodynamical resolution at the scale of high density clumps.

2.3 Smoothed Particles Hydrodynamics

Smoothed Particles Hydrodynamics (SPH) is a finite volume, Lagrangian particle based numerical method to solve the Navier-Stokes equation of motions for a fluid. It is a Lagrangian method because the elements carrying information about the fluid move along the fluid itself.

A different approach to discretize the fluid domain is to use an Eulerian approach, like grid based Adaptive Mesh Refinement (AMR). Recently, so called *moving-mesh* methods have emerged. They combine both approaches and are more flexible but come with their own difficulties (Springel, 2010; Vandenbroucke & De Rijcke, 2016; Weinberger et al., 2019). Usually simple test problems (Sod tube, Sedov blast-wave (Sedov, 1946), Kelvin-Helmholtz instabilities, Noh test (Noh, 1987), Gresho vortex (Gresho & Chan, 1990)), which can be solved analytically, serve as a benchmark for the accuracy of the numerical solution, (e.g. by measuring the distance of the two solution with an L₂-norm in the whole domain, Borrow et al., 2020). Numerical solutions are always a trade-off between accuracy and practicality. It is interesting to see how a certain gain in accuracy is translated in an increase of time-to-solution (Borrow, 2019).

2.3.1 Density Estimation from particles ensemble

SPH has been originally developed as a probabilistic particle method for simulating astrophysical problems (Lucy, 1977; Gingold & Monaghan, 1977b; Monaghan, 2005)¹.

The main idea of the SPH formalism is to write the equations of motion of the fluid for the sampling particles, solve them and then computed physical quantities in every point of the domain trough the so called SPH interpolation.

This kind of interpolation is the same as the one used for the calculation of probability distributions from samples (Parzen, 1962; Wang et al., 2009). Given a kernel $W(x, h)$ function of the spatial coordinate x with smoothing length h , the interpolation $A_I(\mathbf{r})$ of a quantity $A(\mathbf{r})$ is given by:

$$A_I(\mathbf{r}) = \int A(\mathbf{r}') W(\|\mathbf{r} - \mathbf{r}'\|, h) d\mathbf{r}'. \quad (2.13)$$

Any function which follow these two assumptions can be used as the smooth-

¹In a lecture given at Monash University in 2018 <https://youtu.be/tAXHCAEgSuE>, prof. Monaghan retraces the origin of the SPH method, recalling that the inspiration for the particle methods to estimate density in fluids comes from David George Kendall, a statistician he collaborated with in Cambridge.

ing kernel:

$$\lim_{h \rightarrow 0} W(x, h) = \delta(x),$$

$$\int_{-\infty}^{\infty} W(x, h) dx = 1$$

An example of the kernel is a Gaussian:

$$W(x, h) = \frac{1}{h\sqrt{\pi}} e^{-x^2/h^2} \quad (2.14)$$

In general, it's much more practical to use a finite support approximation of a Gaussian. The most often used for SPH are the Schoenberg B-spline functions (Schoenberg, 1946), generated as the Fourier transform (Monaghan, 1985, 2005; Price, 2012):

$$M_n(r, h) = \frac{1}{2\pi} \int_{-\infty}^{\infty} \left(\frac{\sin(kh/2)}{kh/2} \right)^n \cos(kr) dk. \quad (2.15)$$

By increasing n we obtain progressively better approximations of a Gaussian (see Section 13.3 of Easton, 2010). It is convenient to require continuity in at least the first and second derivatives. Accordingly, the most widely used B-spline for SPH is the lowest order B-spline with these features which is the cubic spline kernel M_4 :

$$M_4(q) = \frac{1}{\pi h^3} \begin{cases} \frac{1}{4}(2-q)^3 - (1-q)^3, & 0 \leq q < 1; \\ \frac{1}{4}(2-q)^3, & 1 \leq q < 2; \\ 0, & q \geq 2, \end{cases} \quad (2.16)$$

where $q = r/h$ is the distance normalized by the smoothing length.

To apply the interpolation (2.13) to a fluid we proceed as follows:

$$A_I(\mathbf{r}) = \int \frac{A(\mathbf{r}')\rho(\mathbf{r}')}{\rho(\mathbf{r}')} W(\|\mathbf{r} - \mathbf{r}'\|, h) d\mathbf{r}' \approx \sum_i A_i \frac{m_i}{\rho_i} W(\|\mathbf{r} - \mathbf{r}_i\|, h) \quad (2.17)$$

where we used the approximation that an element of mass $m = \rho(\mathbf{r}')d\mathbf{r}'$. The summation is on all the particles in the domain. That's why a finite support kernel is useful, so that a limited amount of particles is needed to compute the interpolation. It's important to note that in eq. (2.17), two approximations are at play: the first is the fact that the result is $A_I(\mathbf{r}) \approx A(\mathbf{r})$ given that the kernel W only approximates a delta function; the second being that the integral has been substituted with a finite summation.

In case of the density the interpolation simplifies to:

$$\rho_I(\mathbf{r}) = \sum_i m_i W(\|\mathbf{r} - \mathbf{r}_i\|, h). \quad (2.18)$$

Projected interpolation In order to analyze the results of an SPH simulation, it is common to produce maps of interpolated quantities as seen from a particular point of view. To do so the only extra step to perform is the integration of the smoothing kernel along the line of sight. If we are viewing along z , the projected kernel \tilde{W} is :

$$\begin{aligned}\tilde{W} = \int W(\|\mathbf{r} - \mathbf{r}_i\|, h) dz' = \\ \int W\left(\sqrt{(x - x_i)^2 + (y - y_i)^2 + (z - z_i)^2}, h_i\right) dz'\end{aligned}\quad (2.19)$$

2.4 Dwarf galaxies models

We make use of the MoRIA (Models of Realistic dwarfs In Action) suite of N -body/SPH simulations of late-type isolated dwarf galaxies. They are ~ 30 simulations that cover the dwarf galaxy regime (ranging from $10^{6.5} M_{\odot}$ to $10^9 M_{\odot}$ in stellar mass at $z = 0$) with different mass assembly histories in a cosmological setting with added Pop III feedback (Verbeke et al., 2017). Isolated proto-galaxies, starting at $z = 13.5$, merge over time along a cosmologically motivated merger tree (Cloet-Osselaer et al., 2014).

MoRIA dwarfs are the sum of multiple researchers work, starting with the implementation of models for star formation and chemical enrichment (Valcke et al., 2008). Then, in addition to the mass, rotation has been found to have a significant influence on the evolution and appearance of dwarf galaxies and their star formation (Schroyen et al., 2011). Later, the addition of advanced prescriptions for cooling has allowed to increase the resolution when simulating the formation of cold, neutral, high-density clouds suitable for star formation (De Rijcke et al., 2013). MoRIA models could then be used to investigate and reproduce a whole range of observational properties of dwarfs in the field. Studies have been devoted to characterize their cosmological evolution (Cloet-Osselaer et al., 2012), their star formation evolution (Verbeke et al., 2015), their neutral gas contents and kinematics (Koleva et al., 2014). This has helped to shed light onto the “Too big to fail” problem (Verbeke et al., 2017).

Physical characteristics MoRIA dwarfs, have a virial mass at $z = 0$ of $M_{200} \approx 10^{10} - 10^{11} M_{\odot}$. The dark particle mass is $m_{\text{dm}} = 2 \cdot 10^4 M_{\odot}$ whereas the baryonic particle mass m_b follows from the relation $\Omega_b/\Omega_{\text{dm}} = 0.2115$ (Planck Collaboration et al., 2016). The typical number of particles is $n_b = n_{\text{dm}} = 5 \cdot 10^5 - 2 \cdot 10^6 M_{\odot}$.

2.4.1 Sub-grid models

For a review see Verbeke et al. (2017); Vandenbroucke (2016).

Star Formation Star particles are formed in converging, cold and dense regions of gas. The following three conditions must be true for a gas particle to be eligible to become a star particle.

$$\begin{aligned} T_g &< 15000 \text{ K}, \\ \rho_g &> 100 \text{ amu/cm}^3, \\ \nabla \cdot \mathbf{v} &< 0. \end{aligned}$$

The conversion into star particles of gas particles which meet the above conditions is governed by a Schmidt relation (Schmidt, 1959)

$$\dot{\rho}_\star = -\dot{\rho}_g = c_\star \frac{\rho}{t_g}. \quad (2.20)$$

Following Stinson et al. (2006) we assume the characteristic time of formation as the dynamical time $t_g = (4\pi G \rho_g)^{-1/2}$, whereas c_\star is the star formation efficiency which can be adjusted to match observations.

From this, we can solve the simple differential equation:

$$\rho_\star = 1 - e^{c_\star \frac{t}{t_g}}. \quad (2.21)$$

We can then use a stochastic method to determine if an eligible gas particle has to be turned in a gas particle. The Monte Carlo threshold probability of star formation event:

$$P_\star = 1 - \exp\left(-\frac{c_\star \delta t}{t_g}\right), \quad (2.22)$$

where δt is the integration time step. Given a random number $X \in \mathcal{U}(0, 1)$ a star can form if $X < P_\star$. Several authors (Stinson et al., 2006; Revaz et al., 2009; Cloet-Osselaer et al., 2012) have pointed out that since the star formation is a self-regulating process the star formation rate is weakly dependent on the choice of c_\star above 0.1. In our case we use $c_\star = 0.25$. The new star particle inherits the position, velocity and metallicity of its gas particle progenitor. In all effects, star particles represent a stellar population with single age and metallicity (SSP, Single Stellar Population) with a Chabrier initial-mass function, Chabrier (2003).

In a self gravitating gas sphere with a diameter greater than the Jeans length, pressure cannot counteract the gravitational collapse and dense

2 Simulations

regions start to fragment into smaller clumps at the core of which stars may form. The Jeans length is defined as (Jeans, 1902):

$$\lambda_J = c_s \sqrt{\frac{\pi}{G\rho}}, \quad (2.23)$$

where c_s is the local sound speed $c_s = \sqrt{k_B T / \bar{\mu}}$ and $\bar{\mu}$ is the mean molecular mass and ρ and T the local density and temperature respectively.

Following Jeans criterion, smaller scales are stable but given that is Jeans stable, but given that cooling by radiation scales quadratically with the density, while the pressure only scales linearly, the cloud will effectively become unstable. The contraction won't give rise to enough pressure to counteract the gravitational collapse, thus the fragmentation. This highlight the importance of having cooling curves which can be used at high density, and low temperature (De Rijcke et al., 2013).

Also, Bate & Burkert (1997) show that SPH produces in problems involving self-gravity, numerical results are only trustworthy so long as the minimum resolvable mass is always less than a Jeans mass (which is just the mass contained in a sphere of diameter λ_J). Previous versions of the code used directly the Jeans length as a criterion for dynamical instability. But since this requires the comparison between the dynamical time (or free-fall time) of collapse and the local sound crossing time ($t_s = h/c_s$ where h is the smoothing length), the criterion introduced a dependency on the number of particles in the simulations, becoming not practical (Valcke et al., 2008; Stinson et al., 2006). That's why a fixed high density threshold has been used.

Stellar feedback A *feedback mechanism* is any process that allows to exchange energy, matter and/or momentum between galaxy components. Stars have a huge influence on the interstellar medium (ISM). They pump energy and matter in the surrounding gas and enrich the ISM with newly formed metals.

The first type of feedback comes from supernova events. Two main supernova types are important in simulations. For massive stars, when all the fusion fuel is consumed, gravitation overcome the internal hydrodynamic pressure. The core of the star collapses, generating a shock wave which blows away most of the star's outer atmosphere in a massive explosion, leaving behind only a small fraction of its mass, locked up in a remnant (a neutron star or a black hole). This type of core-collapse supernova is called SNII (type II supernova). After an event of this kind happens, the feedback originates from the death of the most massive stars of the

ones sampled by the particle's SSP, until the death of the least massive stars which are still capable of going supernova ($> 8 M_{\odot}$): 0.005 – 0.043 Gyr.

For less massive stars, a Type Ia supernova occurs in a binary star system made by a red giant and a white dwarf. The gas from a red giant overflows onto a white dwarf and when a critical mass is reached, the white dwarf can no longer be supported and collapses, then rebounds. Neutrinos are thought to play an important role in this expansion (Wongwathanarat et al., 2017). Because it involves less massive stars and demands a period of steady accretion, the feedback of SNIA is returned 1.54–1.87 Gyr after the birth of the star particle. Energy injection of SNIA is delayed by a normally distributed offset-time following Strolger et al. (2004). Feedback from supernova events of type Ia (SNIA) and II (SNII) inject 10^{51} erg into the surrounding ISM. For more details, the reader is referred to Valcke et al. (2008).

Supernovae events increase the metal content of the ISM. In our simulations these effects are taken into account by keeping track of two independent abundances as properties of the gas particles: [Mg/Fe] and [Fe/H]. [Mg/Fe] corresponds to a fast contribution by the supernova explosions of massive stars (SNII), whereas [Fe/H] to a slow contribution by intermediate mass binary systems with mass transfer (SNIA) (De Rijcke et al., 2013). The ratio of α -elements to iron, $[\alpha/\text{Fe}]$ (in our case we use magnesium Mg as α -element tracer), can be used to trace the star formation timescale because it is directly linked to the ratio of SNII to SNIA events that have occurred up to the current time (Tolstoy et al., 2009).

A second type of feedback is the stellar wind from young O and B stars. Stellar wind is taken into account as a uniformly spread energy injection of 10^{50} erg in the ISM for 31 Myr, i.e. from the birth of the star particle until the last massive star ($m = 8 M_{\odot}$) turns SNII.

2.4.2 Extended gas physics

Radiative cooling The gas in the inter-stellar medium is a plasma of ionized elements and free-electrons. When for example a free electron is captured by a ion of hydrogen or is decelerated by another charge (in the process called bremsstrahlung), it can emit photons. If the surrounding is not dense, such photons can escape from the gas cloud, effectively removing energy from the gas. This implies a cooling of the gas and a relative decrease of temperature. In high density regions, the interstellar radiation field generated by stars can photo-ionize the gas, whereas low density gas clouds the Ultraviolet Background (UVB) is the dominant ionization factor. The cooling rate depends strongly on the gas chemical composition,

its ionization balance, temperature, electron density. Taking into account all these ingredients, it is possible to compute self-consistently the cooling rate (Maio et al., 2007). The chemical evolution model of our simulations is built from the observation that a few parameters are enough to capture all the fundamental processes at play. In particular, following De Rijcke et al. (2013), two parameters are used to obtain the abundance of all other chemical elements: [Mg/Fe] and [Fe/H]. They are tracers of the particle overall chemical composition. We then tabulate a small number of possible two-element compositions covering the range that can occur in a simulation. The cooling and heating rates can then be interpolated for each gas particle given its density, temperature, [Mg/Fe], [Fe/H] and the cosmic redshift (which is necessary to weight the contribution of the UVB, see the last paragraph of this section).

Ionization aware equation of state In an ideal gas with a single type of constituents, the pressure is given by the equation of state:

$$p = nk_B T. \quad (2.24)$$

From (Vandenbroucke, 2016, p. 161), in a multiphase, multicomponent gas with species S , this becomes:

$$p = \left(\sum_S n_s + n_e(T) \right) k_B T = \frac{\rho k_B T}{\bar{\mu}}, \quad (2.25)$$

where we introduced the mean constituent mass $\bar{\mu}$. This quantity depends on the chemical composition of the gas, its ionization state and the temperature. As such, following models from De Rijcke et al. (2013), we can precompute and tabulate it as a function of:

$$\bar{\mu} = \bar{\mu}(T, [\text{Fe}/\text{H}], [\text{Mg}/\text{Fe}], z, \rho).$$

Modified equation of energy when considering ionization We assume a gas of ${}^1\text{H}$ with an ionization fraction x . We consider the internal energy to be composed by a (thermal) kinetic part and a ionization part:

$$\varepsilon = \varepsilon_{\text{kin}} + \varepsilon_{\text{ion}}. \quad (2.26)$$

The kinetic term (directly linked with the temperature) is defined as

$$\varepsilon_{\text{kin}} = \frac{3}{2} k_B T / \bar{\mu}, \quad (2.27)$$

whereas the ionization energy is

$$\varepsilon_{\text{ion}} = \frac{\chi_H}{m_H} x, \quad (2.28)$$

with χ_H and m_H the ionization energy and atomic mass of ^1H .

Assuming no temporal composition changes in the gas (i.e. assuming the gas in ionization equilibrium), the ionization fraction is a function only of the temperature (i.e. the internal kinetic energy) $x = x(T) = x(\varepsilon_{\text{kin}})$, which allows the temporal derivative of equation (2.26) to be written as:

$$\frac{d\varepsilon}{dt} = \frac{1}{1 + X_{\text{ukin}}} \frac{d\varepsilon_{\text{kin}}}{dt}, \quad (2.29)$$

where we defined $X_{\text{ukin}} \equiv \frac{\chi_H}{m_H} \frac{dx}{d\varepsilon_{\text{kin}}}.$ ²

Instead of evolving the total thermal energy, we can hence evolve the kinetic thermal energy, and adapt the thermal energy equation by applying the correction term X_{ukin} . This can be precomputed and tabulated as a function of $(T, [\text{Fe}/\text{H}], [\text{Mg}/\text{Fe}], z, \rho)$.

In galaxy simulations this ionization-aware equation of state has the effects of absorbing energy of modeled supernovae explosions. This has been shown in a Sedov-Taylor blast wave by Vandenbroucke et al. (2013), where the ionization potential absorbs a significant fraction of the energy injected spent ionizing the gas rather than heating it. This process can alter the effects of thermal energy injection by supernovae explosions, an important phenomenon to take into account in simulations of galaxies.

Ultraviolet background The cosmic UV background (UVB) is a photoionizing radiation field due to young UV bright stars or e.g. to QSO whose spectra gets filtered by the Gunn-Peterson effect. It is responsible for preventing gas from cooling in low-mass halos at high redshift (Efstathiou, 1992; Navarro & Steinmetz, 1997). In our simulations, the UVB is taken into account in the look-up-tables for gas cooling/heating, for the ionization equilibrium and the mean molecular mass. Its dependence on redshift is implemented following the model by Faucher-Giguère et al. (2009). Since in dense neutral regions of gas the UVB's photons are absorbed by outer layers of gas, the gas is self shielding. To capture this effect, in De Rijcke et al. (2013), the intensity of the UVB is modeled with an exponential decay for neutral hydrogen regions with number density

$$n_{\text{H}_1} \geq 0.007 \text{ amu cm}^{-3}.$$

²The term X_{ukin} comes from the the convention of writing the internal energy as u . In this thesis we adopted another notation, using ε to represent the internal energy.

2.5 Moving box

Using SPH it is computationally challenging to simulate an entire cluster of hot gas while at the same time having the resolution to properly treat the interactions at the interface between the interstellar and intra-cluster medium (or ICM) that cause ram pressure stripping.

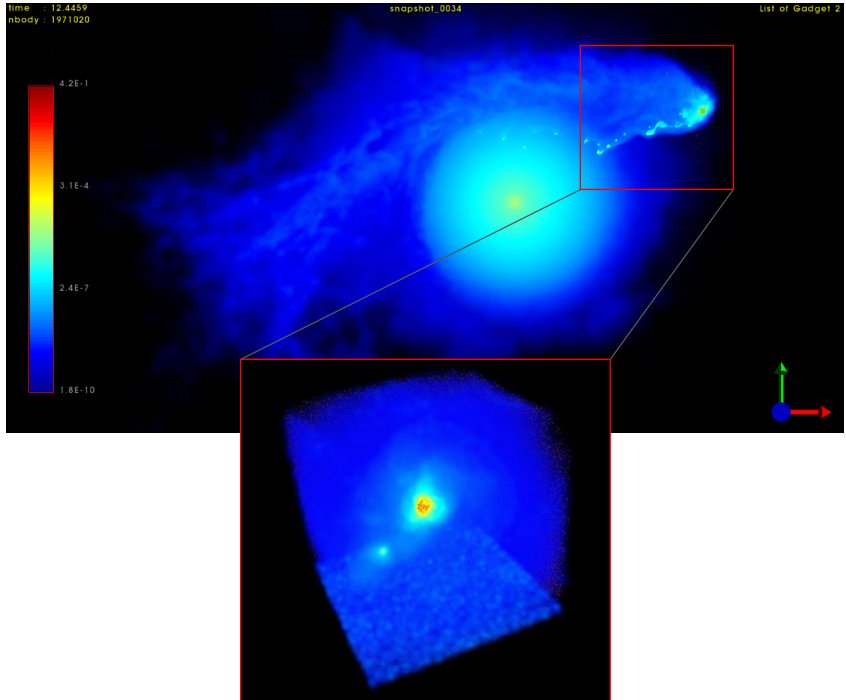


Figure 2.1: An illustration, top panel, of a full fledged simulation of a dwarf galaxy with a Fornax-like cluster. Colors show the gas density (using the glnemo2 software Lambert, 2012). Note the number of particles involved, almost 2 millions. The moving box technique, represented in the boxy inset, allows to concentrate resources on the interesting part of the simulation. Also, at the dwarf-cluster interface an increased resolution is possible, better resolving the stripping.

We have opted to use the moving-box technique described by Nichols et al. (2015) and further developed by Hausammann et al. (2019). As shown in Figure 2.1, we enclose the MoRIA dwarf in a 60 kpc wide moving simulation box, as in a wind tunnel simulation. The box rotates as the galaxy

orbits the cluster, in a way that a side is always facing the dwarf's direction of motion. Gas is injected from the open "bottom" side of the box (see inset in Figure 2.1) and its density and temperature vary with position, as discussed below in Section 2.6. This mimics the hot wind of the cluster halo gas as it streams past the orbiting dwarf galaxy. Given the rotation and the orbital motion of the moving box, additional fictitious forces on the particles are included following a well defined system of reference frames and a consequent rewrite of the equations of motion, as explained more in details in the following Section 2.5.2. This allows us to simulate the combined effects of tidal forces and ram-pressure stripping (as studied by Mayer et al., 2006) which are acting simultaneously on the dwarf without the necessity of simulating a galaxy cluster worth of intra-cluster gas.

2.5.1 Quaternions

For completeness, we briefly introduce quaternion algebra (Hamilton, 1866). Following Graf (2008), a quaternion is a set of four parameters, a real value q_0 and three imaginary values $q_1\mathbf{i}, q_2\mathbf{j}, q_3\mathbf{k}$ with $q_1, q_2, q_3 \in \mathbb{R}$ usually represented as:

$$\mathbf{q} = q_0 + q_1\mathbf{i} + q_2\mathbf{j} + q_3\mathbf{k}. \quad (2.30)$$

The core of quaternion algebra is Hamilton's rule for multiplication of the imaginary units $\mathbf{i}, \mathbf{j}, \mathbf{k}$:

$$\mathbf{i}^2 = \mathbf{j}^2 = \mathbf{k}^2 = \mathbf{ijk} = -1, \quad (2.31)$$

from which a complete set of non commutative multiplication rules can be derived. In fact, noting for example that by left multiplying the last equality in eq. (2.31) by \mathbf{i} : $\mathbf{i}\mathbf{ijk} = -\mathbf{jk} = -\mathbf{i}$, the product of the imaginary parts are:

$$\mathbf{ij} = \mathbf{k}, \mathbf{jk} = \mathbf{i}, \mathbf{ki} = \mathbf{j}. \quad (2.32)$$

Another useful representation of a quaternion is as a pair $\mathbf{q} = (q_0, \vec{q})$ of a scalar part $q_0 \in \mathbb{R}$ and a vector part $\vec{q} \in \mathbb{R}^3$ (also called real and imaginary parts, respectively).³ Its conjugate $\bar{\mathbf{q}}$ is defined as:

$$\bar{\mathbf{q}} = (q_0, -\vec{q}), \quad (2.33)$$

and its norm as:

$$\|\mathbf{q}\| = \sqrt{q_0^2 + q_1^2 + q_2^2 + q_3^2}. \quad (2.34)$$

³Only in this section, to distinguish between quaternions and three dimensional-space vectors, we'll use boldface \mathbf{q} for quaternions and \vec{q} for \mathbb{R}^3 vectors. In the other sections the difference among the two will be clear from the context.

From eqs. (2.31) and (2.32) in particular we can write the general formula for the non commutative quaternion multiplication, i.e. given two quaternions \mathbf{q} and \mathbf{p} :

$$\mathbf{q}\mathbf{p} = (q_0 p_0 - \vec{q} \cdot \vec{p}, q_0 \vec{p} + p_0 \vec{q} + \vec{q} \times \vec{p}). \quad (2.35)$$

From (2.33) it follows that $\mathbf{q}\bar{\mathbf{q}} = \|\mathbf{q}\|^2 \equiv (\|\mathbf{q}\|^2, \vec{0})$. For unit quaternions ($\|\mathbf{q}\| = 1$), we can write $\bar{\mathbf{q}} = \mathbf{q}^{-1}$.

Quaternions and rotations Unit quaternions are also called *rotation quaternions*. They can be used to completely describe a rotation of an angle φ around the axis \vec{q} .

Let's consider a unit quaternion \mathbf{q} . It can be always written as:

$$\mathbf{q} = (q_0, \vec{q}) = \left(\cos \frac{\varphi}{2}, \sin \frac{\varphi}{2} \hat{n} \right), \quad \text{with } \|\hat{n}\| = 1, \quad (2.36)$$

where $\hat{n} \equiv \vec{q}/\|\vec{q}\|$ is the versor of \vec{q} .

A vector in three-dimensional space $\vec{x} \in \mathbb{R}^3$ can be expressed as a *pure quaternion*, a quaternion with no real part: $\mathbf{x} = (0, \vec{x})$.

The vector \vec{x}' resulting from the rotation of \vec{x} of an angle φ around the axis \vec{q} is given by the conjugation operation:

$$\mathbf{x}' = \bar{\mathbf{q}} \mathbf{x} \mathbf{q} \quad (2.37)$$

where $\mathbf{x}' = (0, \vec{x}')$ (for a proof, see e.g. Graf, 2008, sec. 1.4).

It is interesting to note that given two unit vectors \hat{v}_1, \hat{v}_2 , the inverse operation of finding a quaternion \mathbf{q} which rotate \hat{v}_1 into \hat{v}_2 can be found as:

$$\mathbf{q} = \frac{\mathbf{q}^*}{\|\mathbf{q}^*\|} \quad \text{with } \mathbf{q}^* = (\hat{v}_1 \cdot \hat{v}_2 + 1, \hat{v}_1 \times \hat{v}_2). \quad (2.38)$$

In fact, $\hat{v}_1 \cdot \hat{v}_2 = \cos \varphi$ (with φ the angle between \hat{v}_1 and \hat{v}_2) is double the angle of the rotation required by equation (2.36). To get the correct rotation we summed the “no rotation” quaternion $(1, \vec{0})$ to it and normalized the result. In the special case that $\hat{v}_1 = -\hat{v}_2$, the resulting quaternion is $(0, \hat{v}_1^\perp)$ with \hat{v}_1^\perp any unit vector perpendicular to \hat{v}_1 (i.e. a rotation of π around any orthogonal vector).

In the following sections we'll write equations that involve the rotation a quaternion by a vector. With a slight abuse of notation we will write directly $\mathbf{x}' = \bar{\mathbf{q}} \mathbf{x} \mathbf{q}$, considering that the vector indicated in boldface \mathbf{x} should be understood to be the pure quaternion $(0, \vec{x})$.

2.5.2 Velocity and acceleration of the particles in the moving box

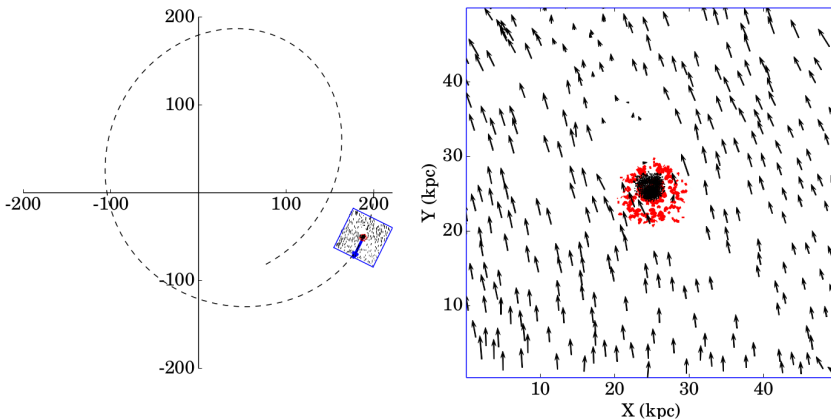


Figure 2.2: From Nichols et al. (2015). On the left it is shown the the moving box trajectory. The blue arrow represents the instantaneous box (and therefore dwarf galaxy) velocity. On the right, gaseous particles are injected from the bottom side of the box. In red, dark matter density contours, and arrows indicate the wind particles velocity.

Reference frames In a moving box simulation we define the inertial reference frame where the cluster is at the origin. Relative to that, the box moves and rotates, as shown in Figure 2.2. Following the convention in Nichols et al. (2015), capital letters are used for vectors in the inertial frame whereas small letters for vectors in the moving box (rotating frame).

Let \mathbf{q} be the quaternion which at each point in time maps the $-y$ axis of the rotating reference frame to the direction of the velocity of the box in the inertial frame, \mathbf{V}_p . Therefore, a vector \mathbf{X} in the inertial frame, corresponds to $\mathbf{x} = \bar{\mathbf{q}} \mathbf{X} \mathbf{q}$ in the rotating frame. A fixed point inside the moving box is taken as a reference point, the so called pivot, whose coordinates relative to the box are \mathbf{x}_p and its velocity and acceleration in the inertial frame relative to the cluster are denoted with \mathbf{V}_p and \mathbf{A}_p , respectively. The pivot represents the position in the box of minimum specific energy (the average position of the 64 particles with minimum total potential and kinetic energy) at the start of the simulation and is used to track the velocity and the acceleration of the box.

For a generic particle, the velocity in the moving box reference frame is:

$$\mathbf{v} = \mathbf{q} \mathbf{V}_p \bar{\mathbf{q}} - \boldsymbol{\omega} \times (\mathbf{x} - \mathbf{x}_p), \quad (2.39)$$

and its acceleration:

$$\mathbf{a} = \mathbf{q} \mathbf{A}_p \bar{\mathbf{q}} - 2\boldsymbol{\omega} \times \mathbf{v} - \boldsymbol{\omega} \times (\boldsymbol{\omega} \times (\mathbf{x} - \mathbf{x}_p)) - \dot{\boldsymbol{\omega}} \times (\mathbf{x} - \mathbf{x}_p). \quad (2.40)$$

2.5.3 Critically damped oscillator

The acceleration of the pivot point is due mainly to the gravitational attraction of the cluster. The dwarf galaxy experiences also a low intensity drag due to the gas impinging the galaxy. In order to keep the galaxy at the center of the box, an *ad hoc* corrective acceleration \mathbf{A}_p^{hoc} is added to it as it moves. This translates to adding an acceleration term to the pivot $\mathbf{A}_p = -\nabla\Phi(\mathbf{X}_p) + \mathbf{A}_p^{hoc}$.

In Nichols et al. (2015), the correction term is intended to become zero when not needed. In practice, the 64 particles with lower total energy (kinetic plus potential) are tracked at each timestep and their average position (\mathbf{X}_{64}) is taken as the center of the galaxy. The goal of the ad hoc acceleration is to move the box to follow the center of the galaxy and so compensate the drift of these particles from the pivot. In the original implementation, \mathbf{A}_p^{hoc} is put to zero as soon as the velocity of the central low energy particles is again directed towards the pivot point (i.e. $(\mathbf{X}_{64} - \mathbf{X}_p) \cdot (\mathbf{V}_{64} - \mathbf{V}_p) < 0$). This understandably is done to minimize the total impulse due to the ad hoc term. But this sudden acceleration removal can cause active particles during the numerical time integration to be kicked away unnaturally, because of the particle acceleration in equation (2.40).

An improvement in our implementation of the moving-box method is the use of a critically damped oscillator for the *ad hoc* acceleration.

$$\mathbf{A}_p^{hoc} = 2\zeta\omega_0\mathbf{V}_p + \omega_0^2\mathbf{X}_p, \quad (2.41)$$

where ω_0 is the undamped angular frequency of the oscillator, and ζ the damping ratio.

We start by noting empirically that for our typical galaxy size a sufficient acceleration requires that $\omega_n^2 \approx 10 \text{ Gyr}^{-2}$. Given that we want to damp the oscillation as fast as possible. We use a critically damped oscillator for which $\zeta = 1$. Therefore the viscous coefficient $2\zeta\omega_0$ is simply 6.3 Gyr^{-1} . A typical behaviour of the *ad hoc* acceleration is shown in Figure 2.3.

2.5.4 Recovering the correct kinematics from a moving box simulation

Essential to the analysis of the kinematics of simulated galaxies, is the recovery of the velocity in the correct reference frame. Only after this pro-

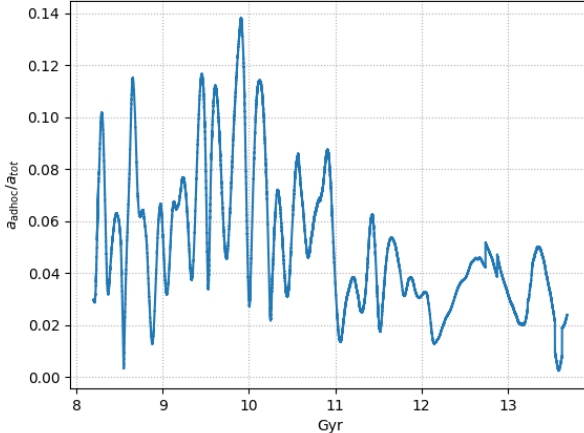


Figure 2.3: Adhoc acceleration relative to the total gravitational acceleration of the simulation ID 69 with pericenter 200 kpc.

cessing, the simulation snapshots are ready to be analyzed. To do so, we have to invert the transformations explained in the previous sections.

We are therefore interested in finding the expression of the velocity \mathbf{V} in the inertial frame at a certain position \mathbf{x} in the moving box, knowing its velocity in the rotating frame \mathbf{v} . Let Ω be the angular velocity of the box in the inertial frame which can be computed as:

$$\Omega = (\mathbf{V}_p \times \mathbf{A}_p) / V_p^2. \quad (2.42)$$

In the rotating frame the angular velocity of the box can be expressed as:

$$\omega = \bar{\mathbf{q}} \Omega \mathbf{q}. \quad (2.43)$$

We can then transform back from rotating to inertial coordinates by applying this transformation:

$$\mathbf{V} = \mathbf{V}_p + \mathbf{q} (\mathbf{v} + \omega \times (\mathbf{x} - \mathbf{x}_p)) \bar{\mathbf{q}} \quad (2.44)$$

where \mathbf{x} and \mathbf{v} are position and velocity of the particle in the rotating frame, respectively, and \mathbf{V} its velocity in the inertial frame.

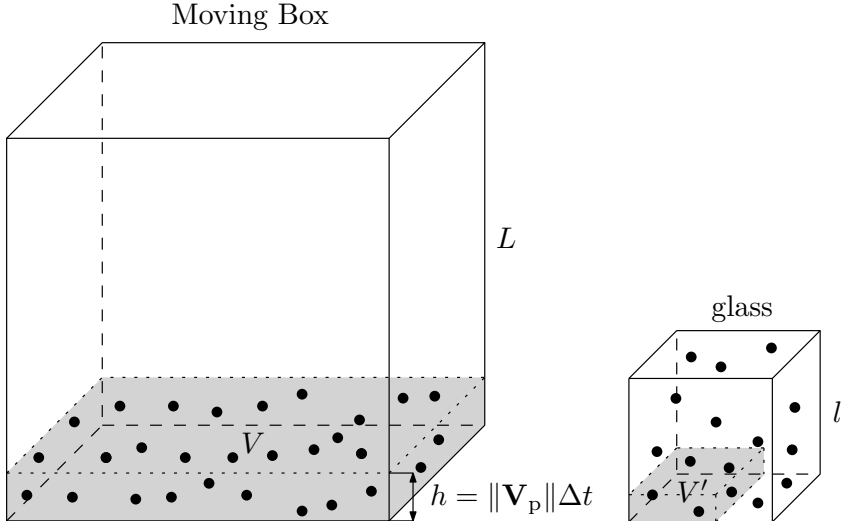


Figure 2.4: Injection of new particles in the box from a “cartridge” of particles in a glass.

2.5.5 Injecting and removing particles in the moving box

The wind of the moving box is due to particles belonging to the cluster injected with correct velocity, density and temperature in the box. We assume the cluster gas to have the density and pressure of the Fornax cluster as described by Paolillo et al. (2002) and in Section 2.6.1. We also assumed zero metallicity and α -abundance (which means no Fe or Mg content in our simulations, cf. Section 2.4.2).

The cluster gas is injected using a sort of “cartridge” of particles previously computed as a unit sized cubic glass structure of $N_{\text{glass}} \approx 18000$ particles. The glass is generated from a random distribution of particles letting them evolve in a periodic box with negative gravitational attraction (effectively being a repulsive force). The resulting low energy distribution of particles guarantees a low probability of injecting dense clumps of particles which may have high kinetic energy once released.

At each timestep we inject new particles to the moving box with the correct cluster density $\rho_c(r)$ at the instantaneous orbital radius r . The number of particles N_c needed to fill up the moving box of size L with density $\rho_c(r)$ is:

$$N_c = \frac{\rho_c(r)L^3}{m_g}. \quad (2.45)$$

Analogously, the total number of particles in the cubic glass N_{glass} of size $l = 1$ is linked to the density of the glass by the same relation:

$$N_{\text{glass}} = \frac{\rho_{\text{glass}} l^3}{m_g}. \quad (2.46)$$

At each timestep Δt the correct amount of new particles N_c^{new} needed to fill the volume $V = L^2 h = L^2 \|\mathbf{V}_p\| \Delta t$ in the moving box, see Figure 2.4, can be computed as:

$$N_c^{\text{new}} = \frac{\rho_c(r) V}{m_g}. \quad (2.47)$$

We now want to compute the volume V' in the glass that corresponds to N_c^{new} :

$$V' = \frac{N_c^{\text{new}} m_g}{\rho_{\text{glass}}}. \quad (2.48)$$

The particles in V' will be selected, their positions scaled and then injected into the moving box.

Substituting equations (2.46) and (2.47) into (2.48), we find an expression for the volume:

$$V' = \frac{l^3 h}{L} \frac{N_c}{N_{\text{glass}}}. \quad (2.49)$$

We define $\xi = \frac{N_c}{N_{\text{glass}}}$, and we note that the number of particles in the glass should be chosen in order for $\xi < 1$ for all the timesteps. Since $l = 1$, the dimensions of $V' = x' \times y' \times z'$ are defined as:

$$\begin{cases} x' &= \sqrt[3]{\xi} \\ y' &= \frac{\|\mathbf{V}_p\| \Delta t}{L} \sqrt[3]{\xi} \\ z' &= \sqrt[3]{\xi} \end{cases} \quad (2.50)$$

At the next step the new volume in the cartridge is taken starting from y' of the previous timestep, so that new particles are used. After a considerable number of steps, when the top of the glass is reached, the process is repeated in a periodic fashion, starting to take particles again from the bottom of the cartridge.

The density and the temperature of the new particles are set according to the instantaneous radial distance r of the galaxy in orbit, the pressure and energy computed using the equation of state (cf. paragraph 2.4.2). By construction the new particles have velocity $\|\mathbf{V}_p\|$ directed towards the local moving box axes $+y$.

2 Simulations

If a particle of any kind gets closer than $L/100$ from the rear edge of the box, it gets deleted. The lateral edges of the box are periodic for gas particles, to keep a constant flow around the galaxy, but dark matter or stellar particles are removed if closer than $L/500$ from any lateral edge of the box. This “death zone” on some edges of the box was introduced by Nichols et al. (2015) and Hausammann et al. (2019) to avoid the spurious build-up of particles at the edges of the box. Using the same parameters we checked that no such build up occurred in our simulations, and that gas, stars and dark matter flows smoothly out of the box.

2.6 Simulating the Fornax cluster environment

2.6.1 Cluster model

Dark matter

The simulations take into account both ram pressure stripping and the tidal interaction with the cluster. The latter is simulated as a single spherically symmetric static NFW potential profile (Navarro et al., 1996) with mass $M = 10^{14} M_{\odot}$ (Drinkwater et al., 2001):

$$\Phi(r) = \frac{GM}{r} \frac{\log(1 + r/R_s)}{\log(1 + c) - \frac{c}{1+c}} \quad (2.51)$$

with scale length $R_s = 120$ kpc and $c = 8.15$ derived from scaling relations in e.g. Gentile et al. (2004); Wechsler et al. (2002):

$$c \simeq 20 \left(\frac{M}{10^{11} M_{\odot}} \right)^{-0.13}, \quad R_s = \frac{1}{c} \left(\frac{M}{\frac{4}{3}\pi 200 \rho_c} \right)^{\frac{1}{3}}, \quad (2.52)$$

with $\rho_c = 127.3 M_{\odot} \text{ kpc}^{-3}$ the critical density of the universe at $z = 0$ for a cosmology with Hubble constant $h = 0.67$ and $\Omega_m = 0.31$ (Planck Collaboration et al., 2016).

The cluster virial radius of the model is $R_{\text{vir}} = cR_s = 978$ kpc.

Intra-Cluster Medium (ICM)

Following Paolillo et al. (2002), we use the superposition of three spherically symmetric beta-models, $\rho(r) = \rho_0(1 + (r/r_0)^2)^{-3\beta/2}$, to construct the gas density profile in the Fornax cluster, as shown in Figure 2.5. They identify three contributions to the hot gas distributions: a central component (dominating for $r < 5''$), coincident with the optical galaxy NGC1399; a

less dense and more extended galactic component ($50'' < r < 400''$); and a cluster component ($r > 400''$). We assume the gas to be in hydrostatic equilibrium with temperature $T(r)$ computed as:

$$T(r) = \frac{m_p}{k_B \rho(r)} \int_r^\infty \rho(r') \frac{GM(r')}{r'^2} dr' \quad (2.53)$$

where $M(r)$ is the mass of the gas, stars and dark matter beyond radius r , m_p is the proton mass, G and k_B the gravitational and Boltzmann constants.

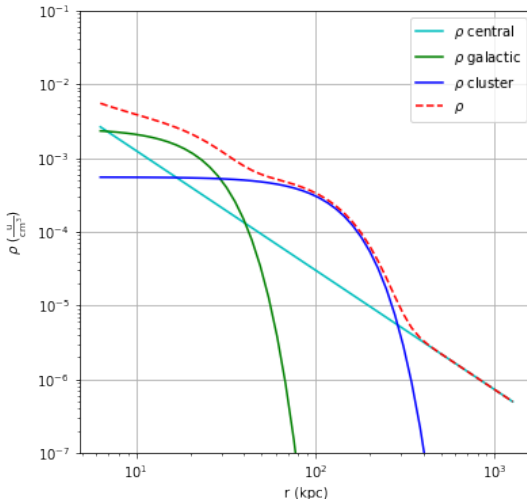


Figure 2.5: Gas density profile $\rho(r)$ of the Fornax Cluster model as a superposition of three beta models from measurements described in Paolillo et al. (2002), from which we also adopt the nomenclature for the different beta models.

These two radial profiles allow us to inject particles with the proper density and temperature in the moving box, hence recreating the environmental condition of the cluster as the dwarf orbits through it.

2.6.2 Simulation parameters

We carried out a set of simulations starting from five MoRIA models of late-type galaxies taken at $z = 0.5$. The overall goal in setting up the simulations is to study the evolution of late-type galaxies in a cluster environment. The choice of the redshift of infall has been motivated by the fact

2 Simulations

Sim ID	$\log_{10}(M_*/M_\odot)$	R_e (kpc)	σ_* (km/s)
62	6.66	0.8	11.4
71	7.58	1.9	21.9
68	7.96	2.6	15.6
69	8.04	2.3	24.6
41	8.78	1.7	30.4

Table 2.1: Features at time of infall ($z = 0.5$) of the selected MoRIA dwarf models used in this work

that the number of red dwarfs in the Fornax cluster has increased significantly since $z = 0.5$ (Stott et al., 2007; De Rijcke et al., 2010). That indicates that the conversion of late-type to early-type dwarfs (and hence the acquisition of late-type dwarfs by clusters) is probably a recent event.

We selected dwarfs models covering the stellar mass range of $10^{7.5} - 10^9$ and we injected each of them on 5 different orbits with pericenter distances of 50, 100, 150, 200, and 300 kpc and with a fixed apocenter of 800 kpc. The starting point of the infall is always at a radial distance of 600 kpc. We chose a lower radial distance of the starting position with respect to the virial radius given the very low cluster density in that region and the low orbital velocity of the dwarf near apocentre. In this way, simulations could be concentrated on the infall and the pericenter passages of the simulated dwarfs. We evolved the galaxies for 5.5 Gyrs up to $z = 0$. The initial stellar masses are reported in Table 2.1. All simulations presented in this paper, at time of injection have exponentially declining SB profiles with Sersic index around 1.0. Every 10 Myr a snapshot is saved, yielding around 560 snapshots for each simulation. This high snapshot cadence has proven to be important for the following analysis (see Section 4.3.1). Adhering to the simulation goal of following the evolution of a gas-rich late-type dwarf in a Fornax-like cluster, the initial snapshot of the most massive dwarf (ID 41) has been taken at $z = 0.4$ because at $z = 0.5$ it was still undergoing a major merger event. This is equivalent to having this galaxy falling into the cluster more recently. No sizeable effect has been noted in simulations results highlighting a different behaviour with respect to the other galaxies (which underwent their last merger before infalling to the cluster at $z = 0.5$, see e.g. Cloet-Osselaer et al., 2014). This has had the only implication of a lower number of snapshots used in the technique explained in Section 4.3.1, but, as we shall see in the following, given that first pericenter passage turns out to be the most significant orbital phase, no notable bias is expected.

Simulation results

3

We present here the results of the simulations performed using the technique described in the previous Chapter. We will concentrate on following the journey of the galaxy into the cluster and characterize its evolution depending on the initial mass at the time of injection and its orbit. Generally, galaxies will undergo some “phase transitions” which will happen mainly at pericenter passages. Some of the galaxies will effectively be transformed into Ultra Diffuse Galaxies (as shown in Section 3.1), some others will be allowed to be briefly identified as “jellyfish” (Section 3.2).

In Table 3.1 we present the final value of some physical values at the end of the simulations which were performed from 8.5 Gyr to ≈ 14 Gyr¹. Before starting the exposition, we have to introduce a couple of concepts which revealed particularly useful in the analysis and allowed for better comparison among the different MoRIA galaxies and the orbits introduced above.

Radial period Pericenter passages, as explained in the following, are important moments for the life of the simulated dwarf. In order to compare different orbits, we normalise the simulation time by the orbital radial period T_r , i.e. the time between two pericenter passages, (Binney & Tremaine, 2008, p. 146):

$$T_r = 2 \int_{r_p}^{r_a} \frac{dr}{\sqrt{2[E - \Phi(r)] - J^2/r^2}} \quad (3.1)$$

where r_p, r_a are the pericenter and apocenter distance respectively, E and J the orbital energy and angular momentum per unit mass, $\Phi(r)$ the potential at radius r of the NFW halo around which the galaxy is orbiting.

By defining the time of pericenter passage as $t_p : r(t_p) = r_p$, we can introduce the normalized time:

$$\tau = \frac{t - t_p}{T_r}, \quad (3.2)$$

¹We highlight that each simulation required on average ≈ 25 days of wall clock runtime on dedicated computing nodes with 32 cores.

3 Simulation results

name	peric. (kpc)	$\log_{10}(M_*)$	R_e (kpc)	$\sigma^*/$ (km/s)	M_V (mag)	$M_{V'}$ (mag)	n	$\bar{\mu}_{e,\gamma'}$ (mag/arcsec 2)
62	50	6.50	1.6	6.7	-9.7	-10.1	1.1	28.7
62	100	6.57	1.6	8.0	-9.9	-10.2	1.0	28.5
62	150	6.59	1.6	9.1	-9.9	-10.2	1.4	28.6
62	200	6.59	1.7	8.3	-10.0	-10.3	1.2	28.5
62	300	6.64	1.7	8.6	-10.1	-10.4	1.0	28.2
71	50	6.26	6.7	21.6	-9.5	-9.8	0.0	31.8
71	100	6.82	6.2	6.5	-10.9	-11.2	0.5	30.5
71	150	6.79	6.4	0.8	-10.7	-11.0	0.5	30.5
71	200	6.85	6.9	0.8	-11.0	-11.3	0.2	30.4
71	300	6.85	7.2	1.8	-11.0	-11.4	0.2	29.7
69	50	6.81	7.6	1.6	-10.6	-11.0	0.2	30.7
69	100	7.53	7.1	17.8	-12.5	-12.9	0.1	28.4
69	150	8.05	4.3	11.6	-14.2	-14.4	0.3	26.8
69	200	8.34	3.3	18.4	-15.0	-15.3	1.0	25.0
69	300	8.42	1.8	23.9	-15.5	-15.7	0.9	23.5
68	50	6.27	8.0	nan	-9.1	-9.4	0.0	32.3
68	100	6.85	7.3	2.5	-10.6	-10.9	0.1	31.2
68	150	6.85	7.3	nan	-10.6	-10.9	0.1	31.2
68	200	7.02	7.4	nan	-11.4	-11.7	0.1	30.0
68	300	8.09	3.8	11.5	-14.5	-14.8	0.8	26.2
41	50	8.93	3.5	16.5	-16.2	-16.5	1.0	23.9
41	100	8.94	2.5	26.0	-16.4	-16.7	1.0	23.0
41	150	8.99	1.7	28.5	-16.6	-16.8	0.8	22.2
41	200	8.97	2.2	29.4	-16.6	-16.8	0.8	22.5
41	300	9.04	1.8	33.7	-17.0	-17.2	0.7	21.8

Table 3.1: Features of the selected MoRIA galaxies at $z = 0$.

3.1 Becoming an Ultra Diffuse Galaxy (UDG)

which is 0 or 1 for first or second pericenters respectively, and 0.5 for apocenter passages.

In the following we will compare the effects of orbit and initial mass using the set of 25 simulations we have carried out.

Tidal radius As we shall see, the cluster gravitational potential is able to strip material from the galaxy. Some of the simulations, depending on the orbit they are on, will become gravitationally unbound dominated by the cluster potential. We chose to define the event of becoming unbound using the condition on the tidal radius King (1962): namely when it becomes smaller than the effective radius. This criterion tests whether the stellar body of the galaxy would become unbound and dissolved, which is what an observer would consider for the detection of a “galaxy”. Physically, also this implies that orbits of the stars in the outskirts of the galaxy are influenced by the cluster potential more than they are by the galactic halo potential. Tidal radius r_t is computed as follows:

$$r_t = r \sqrt[3]{\frac{M_g}{M_c(r)(3+e)}}, \quad (3.3)$$

where $e = (r_a - r_p)/(r_a + r_p)$ is the eccentricity of the orbit computed, r_a , r_p the apocenter and pericenter radii respectively; $M_c(r)$ is the enclosed cluster mass at radius r , and M_g the instantaneous total mass of the galaxy. As a convention we measure the galaxy mass as the total mass (baryonic and dark matter) within 10 kpc from the center of the galaxy.

In Figure 3.1 we show an example of r_t evolution along the orbit. We define a galaxy to become unbound when the condition

$$R_e > r_t \quad (3.4)$$

first occurs.

3.1 Becoming an Ultra Diffuse Galaxy (UDG)

Faint Low Surface Brightness (LSB) galaxies have been detected in galaxy clusters since the 1980s (e.g. Sandage & Binggeli, 1984).

LSB galaxies are defined as having (Venhola et al., 2017):

$$\begin{cases} \mu_{0,r'} > 23 \text{ mag/arcsec}^2 \\ M_{r'} > -19 \end{cases} \quad (3.5)$$

3 Simulation results

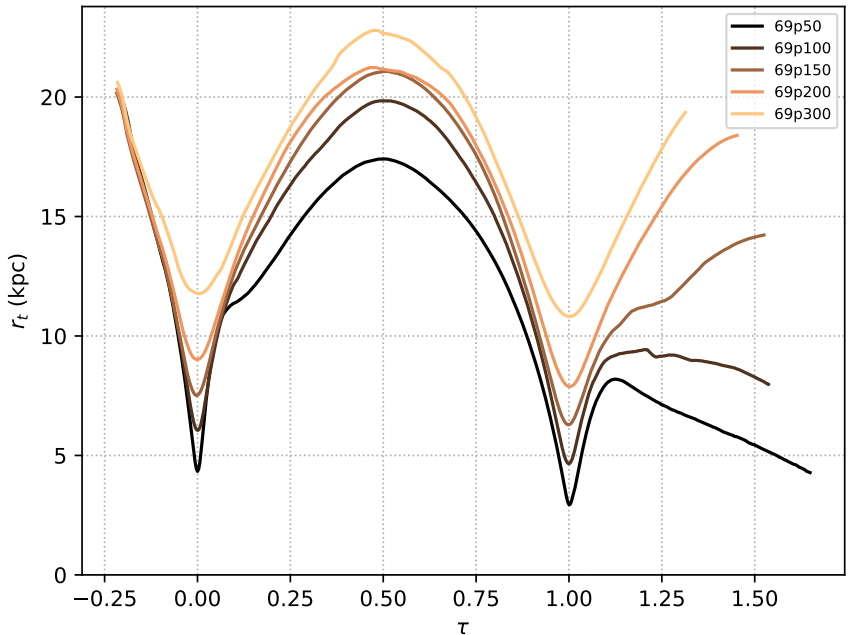


Figure 3.1: Evolution of the tidal radius for the simulations ID 69.

In 2015 Van Dokkum et al. (2015) introduced a size criterion to distinguish between LSB galaxies and more compact ‘normal’ dwarfs (Sales et al., 2021): UDG are therefore defined as large ($R_e > 1.5$ kpc) low surface brightness galaxies.

The majority of studies indicate that they have the properties of large dwarf galaxies (Sandage & Binggeli, 1984; Roman & Trujillo, 2017; Venhola et al., 2017; Saifollahi et al., 2021). Three main mechanisms are hypothesized as possible formation scenarios for UDGs:

- dwarf galaxies which undergo strong tidal stripping (Venhola et al., 2017; Carleton et al., 2018; Rong et al., 2020b);
- gas outflows driven by stellar feedback with extended dark-matter halo and faint and diffuse stellar component (Di Cintio et al., 2017; Mancera Pina et al., 2019),
- or failed L_* galaxies² in high mass dark halos with ceased star formation in the early universe.

Some UDGs have earlier been identified as disrupted early-type galaxies. Koch et al. (2012) is indeed able to reproduce a typical S-shape tidal tailed UDG HCC-087 in the Hydra I cluster via simulations considering only the cluster potential. It is worth noting that in their simulations they find an orientation of the tidal tails perpendicular to the orbit, which will be important in Chapter 4.

The cluster alignment of UDGs is also a quantity which in various cluster has been measured. The signs of elongation, which will be discussed further in Section 3.1.4, have been used to infer the origin of UDGs. In the Coma and Abell 1314 clusters (Yagi et al., 2016; Mancera Pina et al., 2019) UDGs are preferably aligned towards the cluster center. This suggesting that they may be the products of strong tidal interaction with the cluster. In the Fornax cluster, however, the low statistics do not allow for a conclusive analysis. On the other hand at least two of the detected UDGs in Fornax show sign of elongation towards a nearby dwarf galaxy (with $M_r' > -19$ mag, see Venhola et al., 2017). As shown by Rong et al. (2020a), for the Abell 2634 cluster, the minor axes of UDGs tend to be aligned with the major axis of the central dominant galaxy. It is implied therefore that, in this case, UDGs are possibly very recent infallers, still retaining signs of their primordial alignment in the closest large-scale filament they came from.

²An L_* galaxy has a luminosity equal to the characteristic luminosity of the Schechter luminosity function (Press & Schechter, 1974). Its value is about $L_* \approx 3 \times 10^{11} L_\odot$, cf. Cooray & Milosavljević (2005).

UDGs in Fornax Venhola et al. (2017) found nine UDGs candidates within an area of 4 deg^2 centered in NGC1399. The ratio of UDGs to dwarf galaxies in Fornax is consistent with that in the Coma and Virgo clusters. Also, the number of UDGs within the virial radius are correlated with the virial mass of the cluster. In the size-magnitude parameter space, UDGs in Coma form a continuous distribution, whereas in Fornax two of them are remarkably luminous, and can be considered as outliers. Also, UDGs in Fornax are among the more luminous galaxies and their colour correlates with surface brightness, becoming redder with increasing surface brightness. They follow the same color-magnitude relation as dwarfs, which suggests a link between UDGs and dwarf galaxies (cf. Section 3.3). As opposed to the ones in the Coma cluster, their alignment with respect to the cluster potential is not evident: in Coma UDGs are oriented towards the cluster center, whereas in Fornax, as mentioned above, there's no correlation. It is interesting to note that larger UDGs are more elongated as opposed to UDGs in Coma.

3.1.1 Size and magnitudes

Once approaching the pericenter, energy is transferred to the galaxy, according to the virial theorem. Stars thus migrate to more energetic and hence wider orbits. In addition, mass is lost due to tides, making the gravitational well even more shallow and leading to potentially large increases in radius. We compute the 3D effective radius shown in Figure 3.2. This radius is independent of the orientation of the galaxy, and it has been computed as the radius of the sphere which contains half the total luminosity of the galaxy. Tidal heating affects the size of the galaxies as they pass near the cluster center, with low mass galaxies affected most.

3.1.2 M_h/M_\star

We computed the stellar and dark-matter mass inside a sphere of radius 10 kpc centered on the dwarf and the masses inside the entire moving box. While stars get formed around pericenter passages, dark matter instead is pulled out by tidal forces who elongate the halo, effectively stripping dark-matter particles out of the moving box of our simulation setup. This is confirmed for example by comparing the amount of dark matter inside the 10 kpc region around the dwarf with the whole dark matter present inside the moving box. As shown in Figure 3.3, there is an inflow of dark matter towards the dwarf galaxy due to tidal squeezing and compression, soon followed by an expansion, resulting in a dearth of dark matter after the

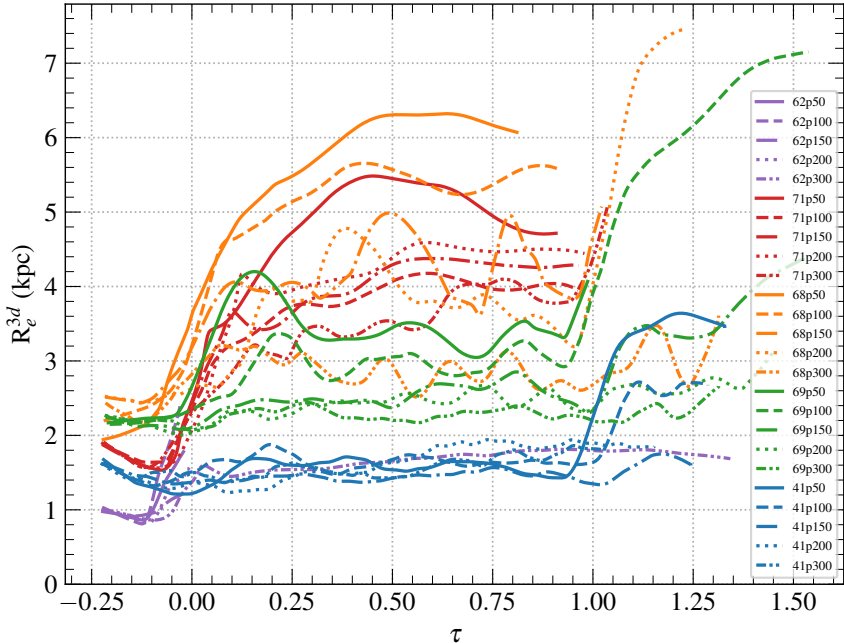


Figure 3.2: 3d effective radius evolution with time normalised with the radial period of the orbit. Curves are smoothed using a rolling average of 0.2 Gyr and are truncated as soon as condition (3.4) is verified.

first pericenter passage. For very radial orbits, around first infall, central halo mass increases more than the stellar mass created by the starburst, Figure 3.4.

3.1.3 Central stellar velocity dispersion

We measured the central (within 250 pc) stellar velocity dispersion for all the simulations on their orbits, as shown in Figure 3.5. For simplicity we adopted a common point of view for all the orbits, and the line-of-sight velocity dispersion is computed assuming the observer laying in the orbital plane. As tidal interactions stir the particles in the center of the galaxies, at the pericenter passages a bump in the central velocity dispersion (denoted by σ) can be seen. The following temporary decrease in central velocity dispersion can be linked to the variations of M_h/M_* . Tidal squeezing increase σ while subsequent mass loss can dramatically lower it.

69

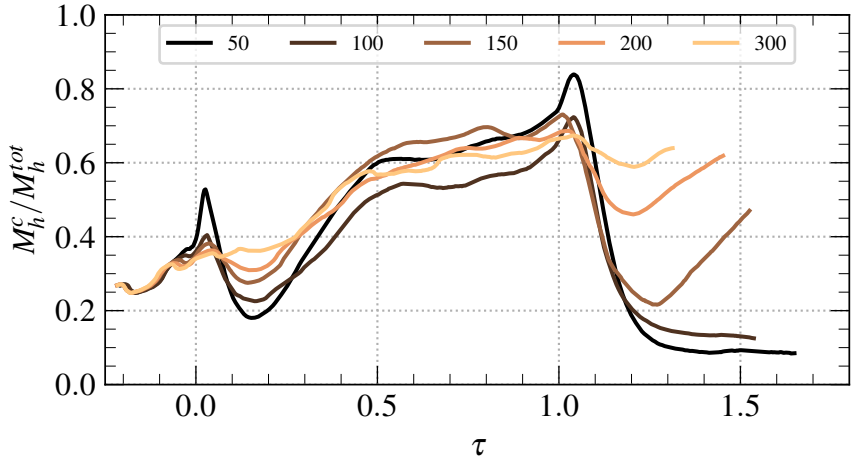


Figure 3.3: Relative amount of central dark matter M_h^c (computed as the mass inside a sphere of 10 kpc of radius around the galaxy) with respect to the dark matter in the simulation box (M_h^{tot}) for sim ID 69. Colours indicate the pericenter distances of the different orbits.

We checked the dynamical mass estimation which can be computed from the velocity dispersion using the Wolf et al. (2010) relation:

$$M_{est}^{dyn} = \frac{3}{G} \sigma_e^2 R_e, \quad (3.6)$$

where σ_e is the luminosity-weighted line-of-sight velocity dispersion within an effective radius R_e , and G the gravitational constant. The result three representative simulations is shown in Figure 3.6. For the low mass galaxy (simulation ID 71), the estimation is not reliable anymore as soon as the galaxy becomes unbound (dashed line in Figure 3.6), i.e. the condition (3.4) does not hold anymore. The method of equation (3.6) overestimates the mass by $\approx 20 - 50\%$ depending on the orbital phase. Given the simplicity of the method, this relation between the estimated value and the ground truth mass is quite remarkable. From this, we can learn that despite some conditions required for the application of the method — such as equilibrium and sphericity — not being fulfilled, the dark-matter content estimates with this method are reliable within an acceptable relative range.

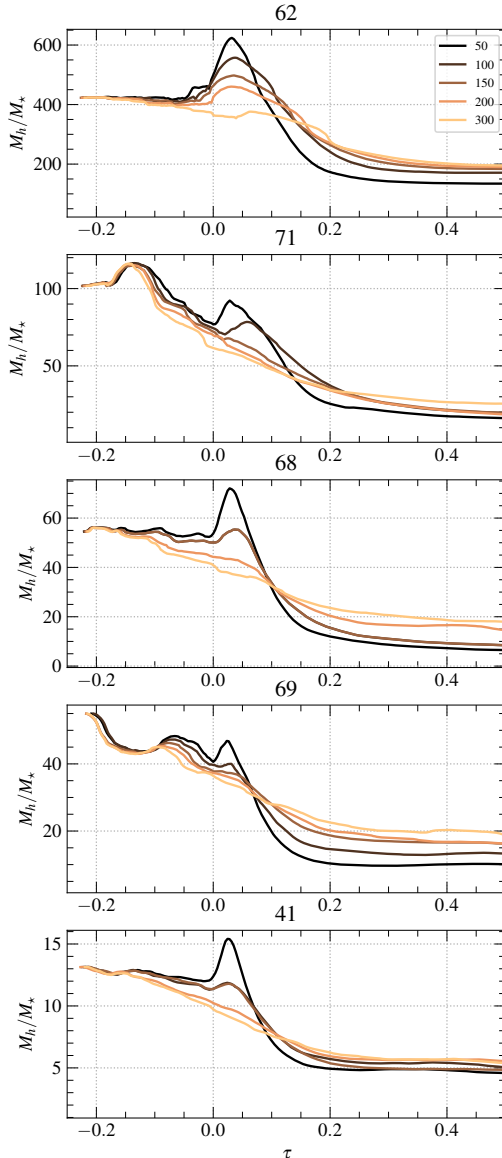


Figure 3.4: M_h/M_* around first infall. Halo and stellar mass are computed in a 10 kpc sphere around the galaxy. The different orbits with the respective pericenters are color coded as shown in the legend.

3 Simulation results

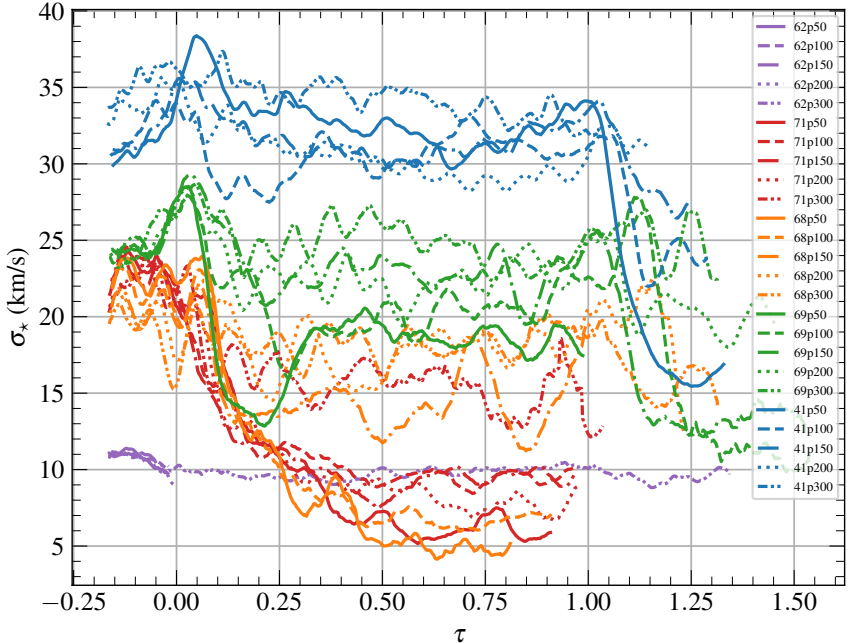


Figure 3.5: The evolution as a function of time (normalized with orbital radial period) of the line-of-sight velocity dispersion (σ_*) of star particles within a 250 pc from the galactic center. Curves are smoothed using a rolling average of 0.2 Gyr.

3.1.4 3D ellipticity

We computed the 3D ellipticity of the stellar component of the galaxies using the Principal Components Analysis (PCA, Pearson, 1901). The first principal component w_2 is the direction of highest elongation (largest variance of the star particle positions) computed via PCA³.

Around pericenter the main elongation direction of the ellipsoid (w_2) is aligned with the cluster center; then it undergoes a “slingshot effect” after pericenter and it aligns with the cluster center also around apocenter before falling back in. This behaviour is shown in Figure 3.7. Around the second pericenter passage, for radial orbits, the galaxy ends up being dispersed and not anymore gravitationally bound.

³ w_2 is defined as the eigenvector corresponding to the largest eigenvalue of the covariance matrix $C = \frac{1}{(N-1)} AA^T$, where A is the matrix of the position of the star particles centered on the barycenter of the stars, and N the number of particles.

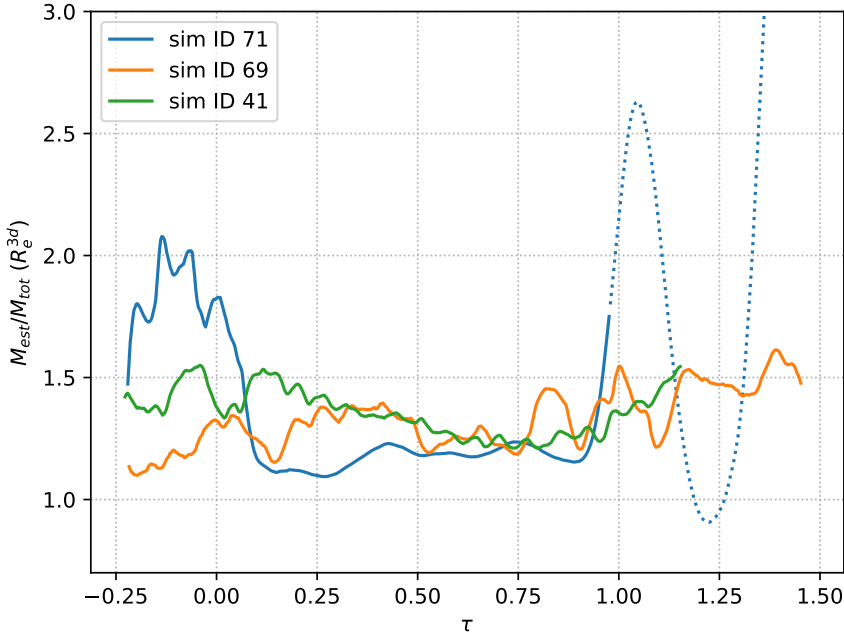


Figure 3.6: The estimated mass from velocity dispersion with equation (3.6) relative to the total mass within an effective radius computed from simulation particles, for simulation ID 69, 71, 41 on an orbit with 200 kpc pericenter. Dashed line indicates unbound snapshots (i.e. for which the condition (3.4) is not verified anymore).

In Figure 3.8, we show quantitatively the relative orientation between w_2 and the clustercentric direction for simulation ID 69. Around both pericenter passages the galaxy becomes aligned with the cluster center. The maximum alignment is obtained at a delayed time depending on the radiality of the orbit. Also, for all the orbits, the galaxy shows an alignment of an angle < 30 deg if the orbital phase lays within a quarter of the radial period soon after pericenter, i.e. $\tau \in [0, 0.25] \cup [1, 1.25]$. Except for the orbit with 100 kpc pericenter, it is possible to see how at apocenter the main elongation is perpendicular to the cluster center.

Analogously, we can compute the angle between the elongation direction and the instantaneous velocity along the orbit. As shown in Figure 3.9, because of the high relative speed and the delay in the formation of tidal tails, around pericenter passages the angle between w_2 varies significantly. Interestingly, just before the pericenters, velocity is almost perpendicular

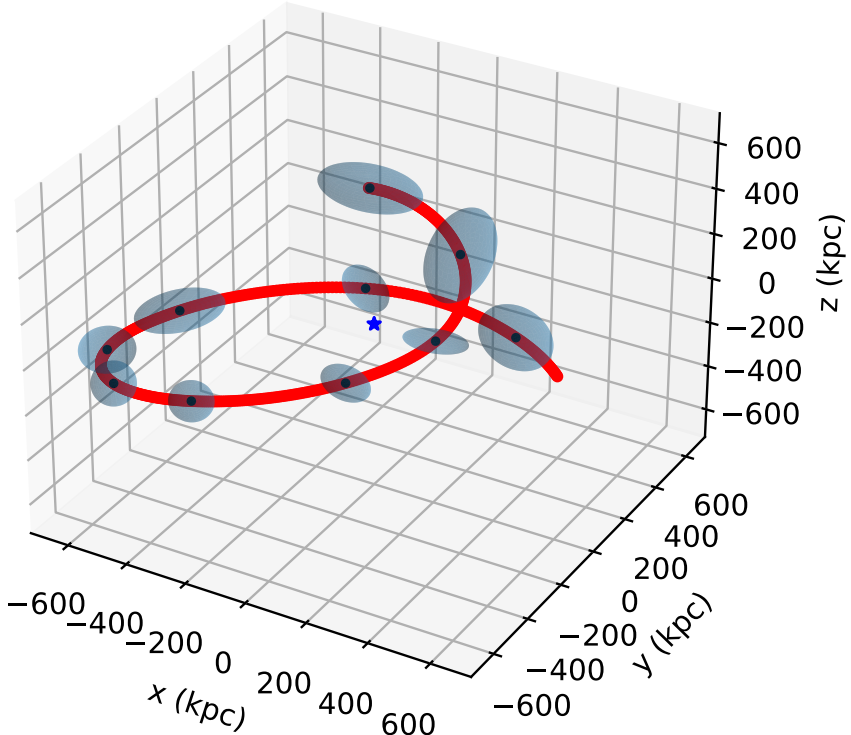


Figure 3.7: Qualitative overview of the principal components ellipsoids for the stellar particle positions of the galaxy along its orbit. In red the orbit of the galaxy, ID 69 with pericenter of 200 kpc.

to the direction of elongation. At the same time, stripping intensity is at its peak (see Figure 4.7) creating a gaseous tail aligned with the instantaneous velocity of the galaxy. This misalignment between the tails is shown in detail in Chapter 4 and can be used to infer orbital properties of observed galaxies in cluster.

3.2 Star formation

As shown in the previous section, elongation of material around low clustercentric distances may create grooves in the potential well which lead to angular-momentum transport. In turn this helps funneling gas towards

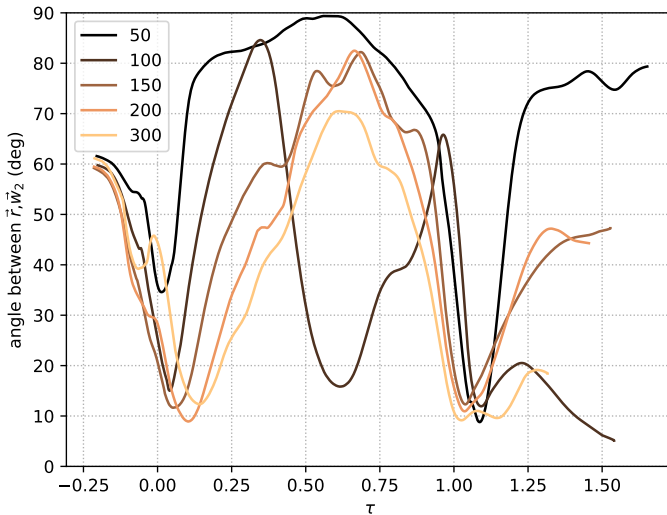


Figure 3.8: Angle between the largest principal component \mathbf{w}_2 and the direction to the cluster center for simulation ID 69. The galaxy shows an alignment of an angle < 30 deg soon after pericenter passages i.e. if the orbital phase $\tau \in [0, 0.25] \cup [1, 1.25]$.

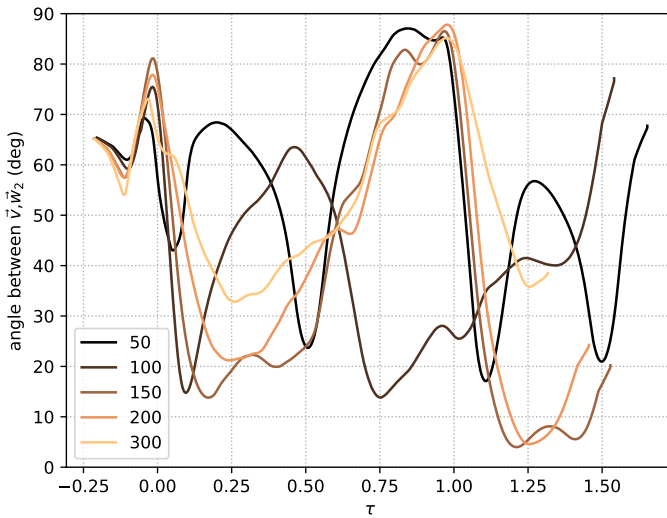


Figure 3.9: Angle between the largest principal component \mathbf{w}_2 and the instantaneous velocity for simulation ID 69.

the center of the galaxy which is squeezed and can cool to create stars. The total content of star forming gas is shown in cyan in Figure 3.10 alongside with the specific star formation rate. It is interesting to note that for an intermediate mass dwarf, the stripping phenomenon is highly nonlinear. For example for simulation ID 68, as shown in the corresponding panel in Figure 3.10, the relatively small change of orbit from 150 kpc pericenter to 100 kpc makes the dwarf completely stripped of its reservoir of cold gas. Due to the stripping, after a burst, star formation stops.

3.2.1 Where do stars form?

In Figure 3.11 we show the average position of the star forming particles for each simulation snapshot. The galaxy is moving in the $-y$ direction (the direction of the instantaneous velocity, see Section 2.5) around pericenter. For each simulation snapshot the number of new stars with respect to the previous snapshot (10 Myr before) is counted and their average position in the xy plane is plotted⁴. In this projection the instantaneous velocity of the galaxy is always directed towards the $-y$ axis. The ram pressure is therefore pushing in the vertically upwards direction in these diagrams, causing gas to be stripped and stars to be formed in the upper part of the panels.

In correspondence of pericenter passage an intense star formation activity is registered in the gaseous tail. These galaxies can therefore be defined *jellyfish* galaxies (Ebeling et al., 2014): the term applies, in fact, to galaxies with star formation activity within the stripped gaseous tails. Star formation flickers on and off inside the gaseous tails as gas clumps are able to cool, condense and create stars. This result supports the idea that the jellyfish phenomenon is a relatively short transitory phase of the galaxy along its orbit.

In the three panels of Figure 3.11, three representative galaxies are shown in increasing order of mass. For the least massive galaxy (simulation ID 71),

⁴ We could have computed the star formation rate from the last galaxy snapshot at $z = 0$, reading the time of formation of the star particles. This is the common approach when computing star formation histories of galaxies, and it is observationally motivated. In fact the star formation history of an observed galaxy is inferred from the photometry and spectrum of the detected starlight.

However, the star particles lost during the orbit (i.e. going out of the Moving Box), leads to an underestimation (of a maximum of 30% for the most recent bins especially on low mass galaxies on radial orbits) of what has actually happened during the galaxy journey around the cluster. This is especially true for star particles formed in the tail of the infalling galaxies: these particles at the time of creation have the same velocity as the stripped gas, which makes them travel away from the simulation box. The method of counting individual star particles newly born is therefore employed. The choice of a high frequency snapshot cadence plays a fundamental role to this end.

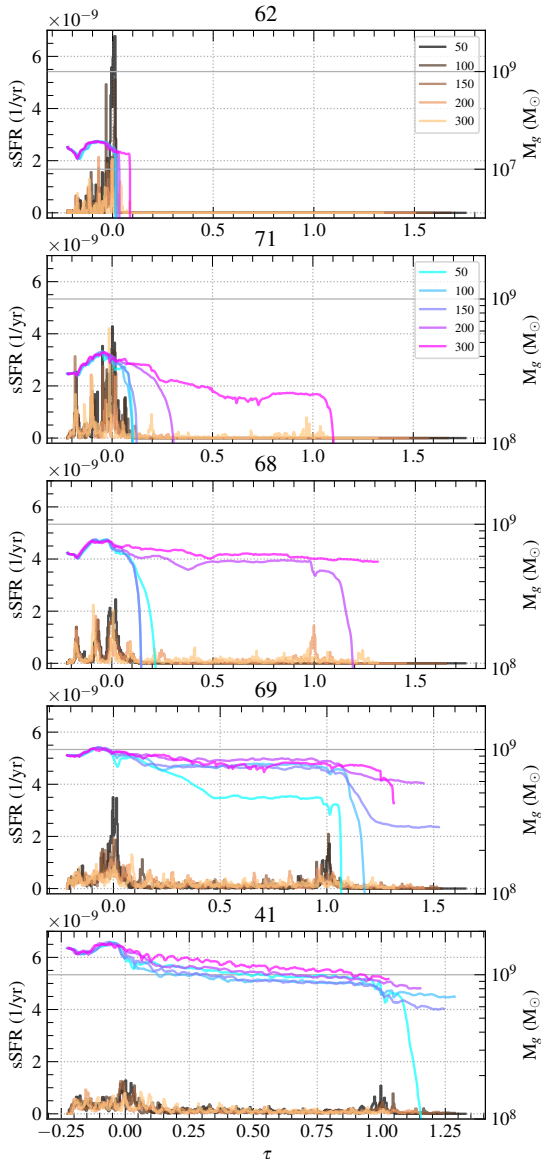
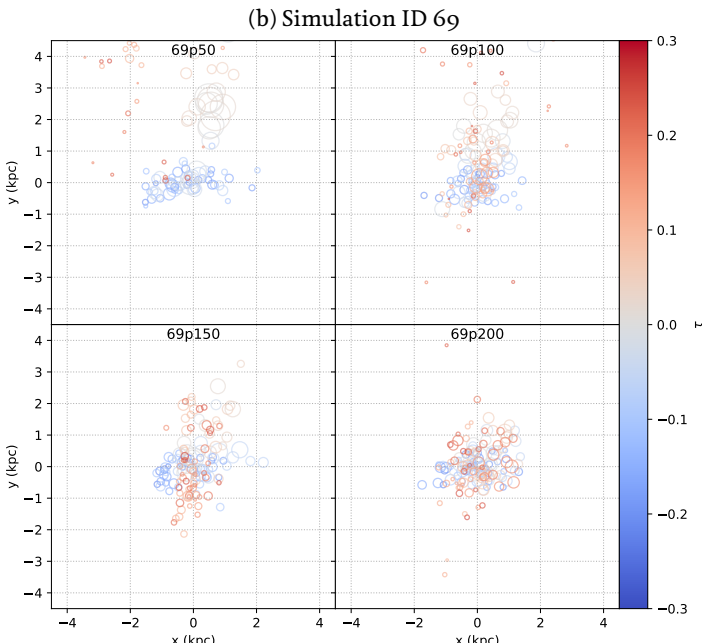
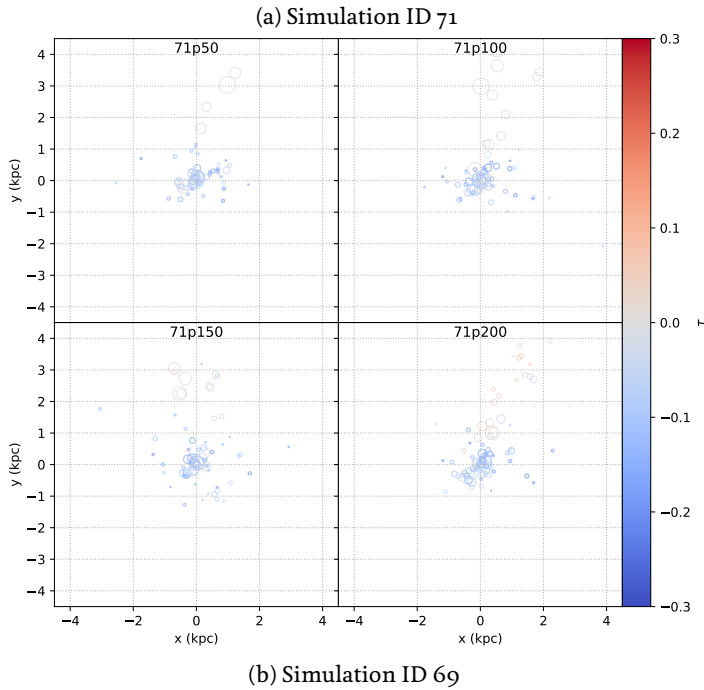


Figure 3.10: Specific Star Formation Rate (sSFR) and cold gas ($T < 15000$ K) evolution on different orbits. Different orbits for each galaxy are indicated with shades of brown for the sSFR, and with shades of cyan for the cold gas.

3 Simulation results



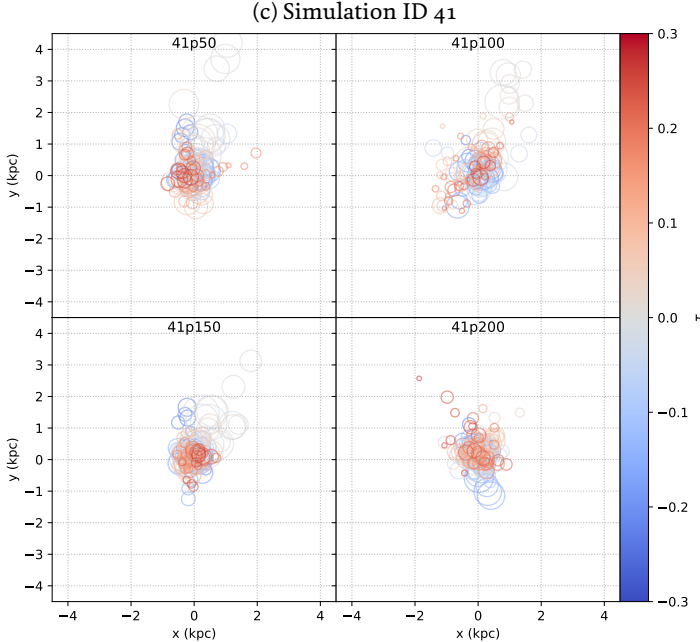


Figure 3.11: Star formation location around first pericenter passage for simulation ID 71, 69 and 41. Each subplot corresponds to a different pericenter. The markers correspond to the barycenter of the positions of the newly formed stars in each snapshot and are colored according to the distance in time from pericenter normalized with the radial period. The size of the markers is proportional to the number of stars born between the current snapshot and the previous one.

as confirmed in Figure 3.10, no stars are formed after pericenter (red markers) because the cold gas is completely stripped by ram-pressure. However, during the stripping phase new star particles appear in the gaseous tail. For the intermediate mass galaxy (simulation ID 69), in the radial orbits, the behaviour is similar to simulation ID 71. Also, a front of newly born star is formed in the center (see panel 69p50) as the gas is compressed and pushed upwards. For the more circular orbits, stars are continuously formed in the center. This is a behaviour similar to the most massive galaxy, simulation ID 41, where clumps of gas are detached only in radial orbits. For the 200 kpc orbit (41p200) stars are even born in front of the galaxy meaning that for a galaxy so massive a layer of star forming gas is not displaced by ram-pressure even at the leading edge of the galaxy.

3.3 Colour Magnitude

The catalogue of dwarf galaxies in the Fornax cluster, prepared by Venholo et al. (2019), can be used to directly compare our results with observations. We build the Color-Magnitude (C-M) diagram with all the simulation snapshots, after computing their SDSS-band colors and magnitude. We then superimposed it on the results of the observations: as shown in Figure 3.12 there is a good agreement between the catalogue values and our simulations. In Fornax, the slopes of the C-M relations are different between the morphologically selected late-type and early-type galaxies. The relation for the former is rather flat, meaning that the color is not correlated with magnitude, whereas the early-types become redder with increasing total luminosity.

In our simulations, the simulated dwarf galaxies tend to be blue and star-forming when they are near to the cluster center. Tidal forces and ram-pressure boosts star formation, implying blue luminosities. The initial mass of the galaxy plays an important role in defining how many times and for how long the galaxy moves between the late-type and early-type regimes. In fact, if the galaxy gets stripped, it settles on the early-type branch; if instead it can keep its gas, it turns blue again when falling into the cluster. In particular the lightest galaxy (ID 62) does not survive the first infall yet ending its life in the early-type galaxy realm, independently of the orbit. On the opposite end of the mass range, the most massive one (ID 41) retains most of its cold gas and, accordingly, its star formation occurs almost steadily, except for the most radial orbit. Only for the 50 kpc orbit its final location on the C-M diagram is among the early-type galaxies. Dwarfs on wide orbits, as shown in the 300 kpc pericenter panel of Figure 3.12, stay on the blue branch indefinitely unless they become unbound (the condition (3.4) ceases to be valid), as it happens for the low-mass galaxies. Figure 3.13 confirms that dwarfs rapidly turn red after quenching.

It is interesting to note that, for instance in the 50 kpc pericenter panel, dwarfs jump across the gap between the blue and red branches in between temporally equidistant snapshots. Given that their color evolves rapidly, the gap between the two branches can be explained: an abundance of dwarfs is not expected in the color interval where their evolution is so quick.

3.4 HI size mass relation during infall

Stevens et al. (2019) show how inevitable is the size-mass relation of neutral hydrogen, even during stripping phases. Our simulations can be checked on the HI size-mass plane. We post-processed our simulations to obtain

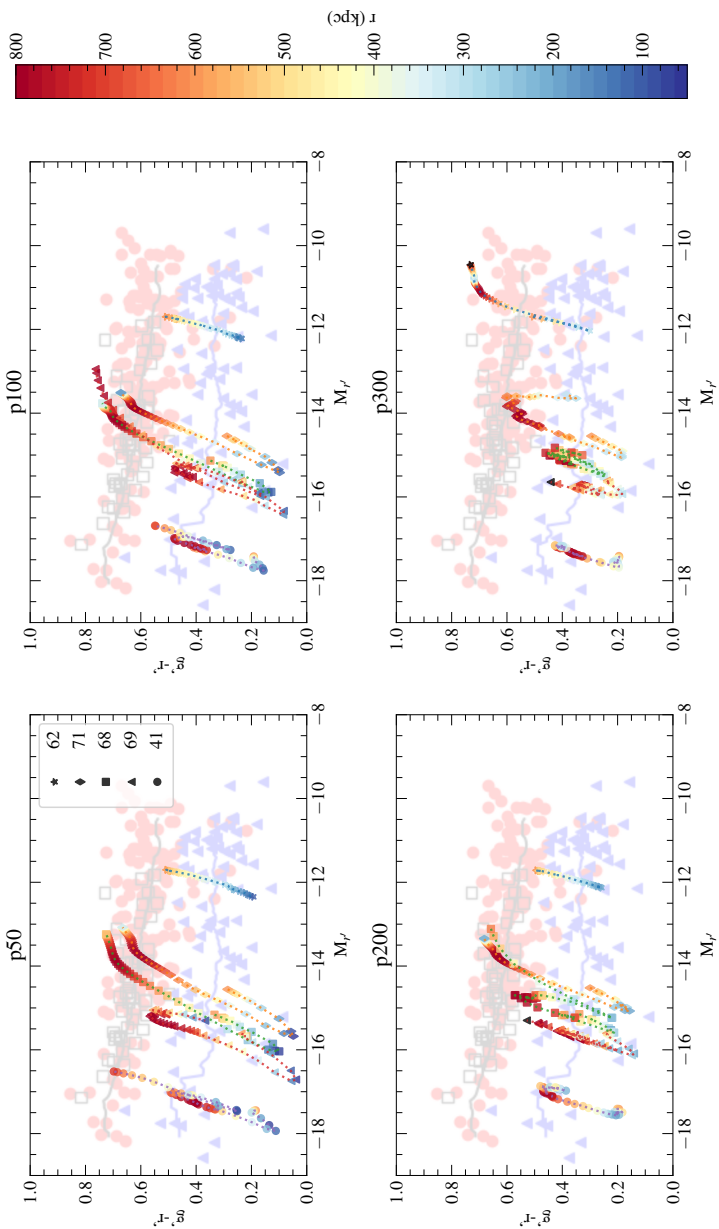


Figure 3.12: SDSS bands colour magnitude diagram of galaxies on different orbits compared to Fornax dwarf catalogue of Venhola et al. (2019). Red and blue colour for the data points in the background represent dwarf elliptical (dE) and late type galaxy respectively, classified by eye on the base of morphology. Empty squares are nucleated dE. Data tracks of simulated galaxies are shown overlaid colour coded by the clustercentric radius. The tracks are limited to bound galaxies i.e. they are drawn with snapshots for which condition (3.4) holds.

3 Simulation results

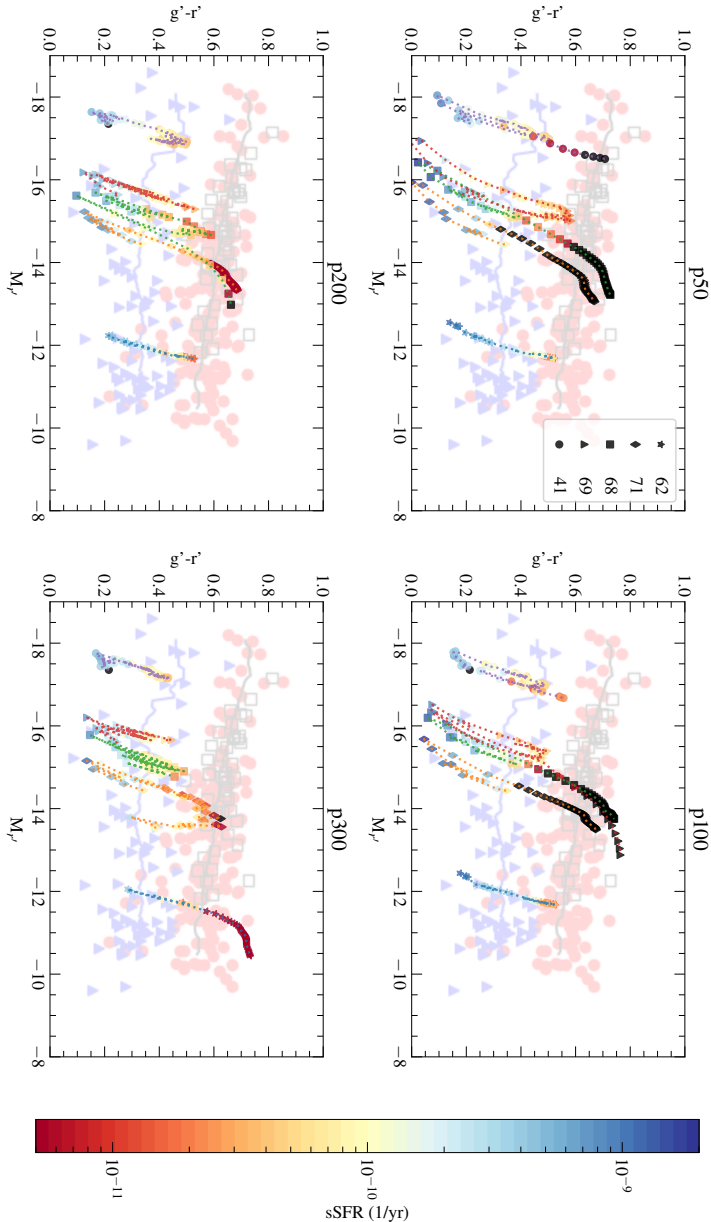


Figure 3.13: Same as Figure 3.12, with point color coded with the specific star formation rate. Black points are snapshots with no star formation.

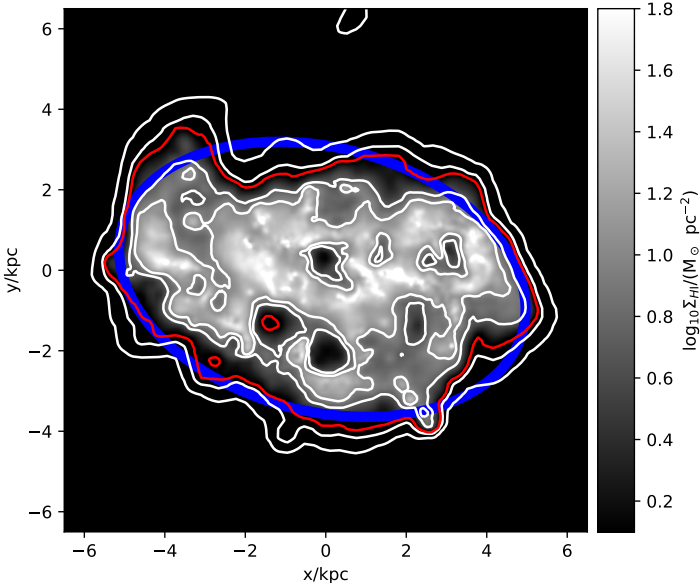


Figure 3.14: HI map for a snapshot of simulation 69 at the beginning of the infall. In white the contours $[0.1, 0.5, 1, 5, 10] M_{\odot} \text{ pc}^{-2}$ of the projected HI density Σ_{HI} . In blue the ellipse fit on the $1 M_{\odot} \text{ pc}^{-2}$ contour, shown in red.

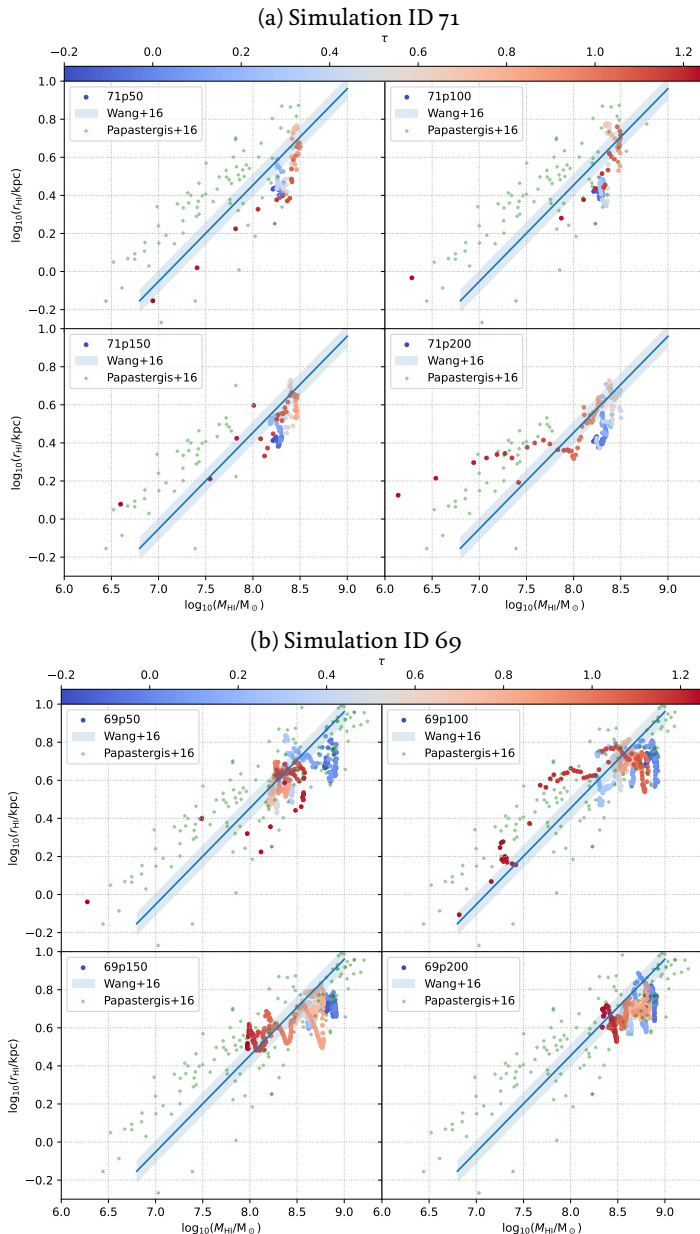
the neutral hydrogen fraction, x_{HI} , of each gas particle. This is done leveraging the models explained in Section 2.4.2. In particular, the HI fraction of a gas particle is computed based on tabulated data from De Rijcke et al. (2013) as a function of density, temperature, composition, and redshift:

$$x_{\text{HI}} = x_{\text{HI}}(T, [\text{Fe}/\text{H}], [\text{Mg}/\text{Fe}], z, \rho),$$

resulting in a HI mass consistent with the sub-grid model employed during the simulations. As in Verbeke et al. (2017), we computed the HI mass by integrating the HI column density Σ_{HI} . To compute the HI radius, we fit an ellipse to the $1 M_{\odot} \text{ pc}^{-2}$ contour of the HI map (as shown in Figure 3.14) and r_{HI} is thus defined as its major axis.

In Figure 3.15 we show the behaviour of the gas of three different simulations on four different orbits each. The snapshots have been oriented following the assumption that the infinitely distant observer lies on the plane of the orbit of the galaxy. We see that our dwarfs stay on the HI size-

3 Simulation results



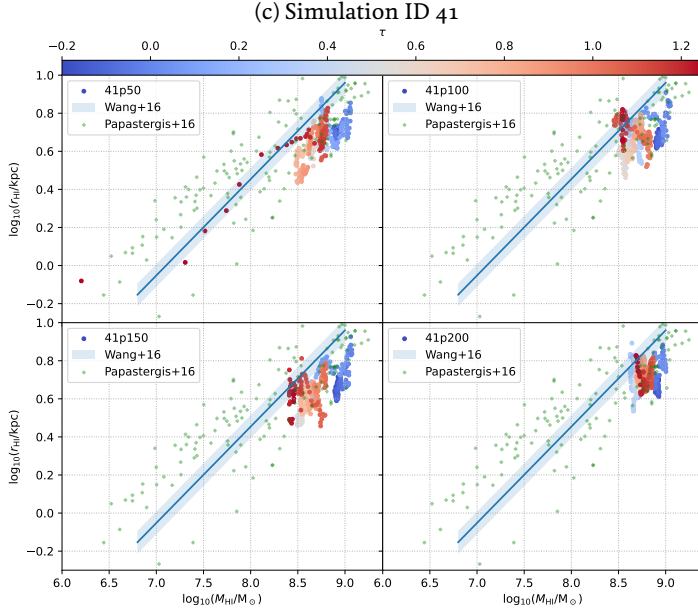


Figure 3.15: HI size-mass relation for simulation ID 71, 69 and 41. The relation of Wang et al. (2016) and data of Papastergis & Shankar (2016) are shown. Each subpanel corresponds to a different pericenter distance.

mass relation as computed by Wang et al. (2016):

$$\log r_{\text{HI}} = (0.506 \pm 0.003) \log M_{\text{HI}} - (3.594 \pm 0.009).$$

The slope of 0.5 implies that the HI mass is proportional to the surface area of the HI disk. Also, data from the ALFALFA blind survey (Papastergis & Shankar, 2016) is used for comparison. For the least massive galaxy (simulation ID 71) on the most radial orbits, the relation is followed closely. In case of no stripping (high pericenter distances) the snapshots lay within the scatter of the data. On the other hand, when there is stripping (for the simulation ID 41, only for the orbit on 50 kpc pericenter), the snapshots move along the relation on the mass-size plane. In other words, the surface density of HI is constant not only among different galaxies but also over time when a galaxy undergoes stripping.

3 Simulation results

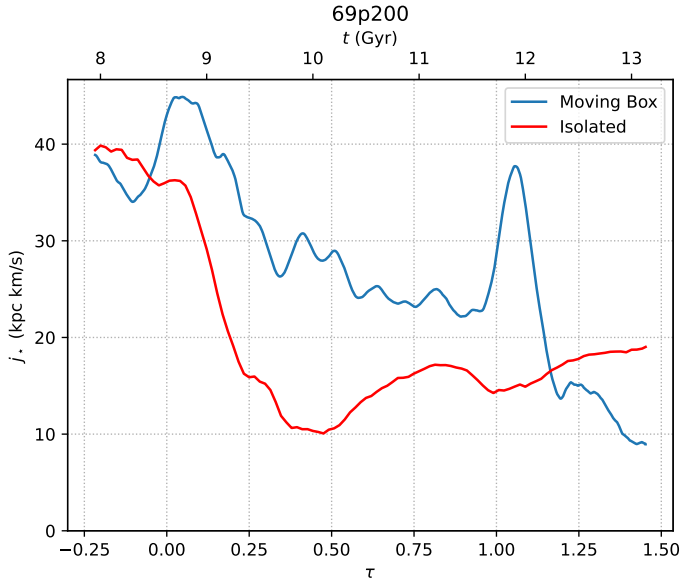


Figure 3.16: Comparison between the norm of the specific angular momentum j_s for the simulation ID 69 on a 200 kpc orbit and the correspondent isolated MoRIA run.

3.5 Kinematics

To correctly compute galaxy kinematics we have to take into account the rotation of the moving box. The details on how to recover the correct kinematics in our setup are shown in Section 2.5.4.

3.5.1 Comparison with simulated galaxies in the field

We compare the specific stellar angular momentum j_s of particles within a sphere of radius 10 kpc from the center of the galaxy for both a simulation in the moving box as well as for a run in isolation. We notice in Figure 3.16 an increase of j_s in correspondence to pericenter passages.

The combination of high-velocity newly born stars and the gravitational energy injection given by the cluster at pericenter, result in a spin-up of the galaxy with respect to its evolution in the field.

3.5.2 Angular momentum and specific angular momentum proxy λ_R

We compute the specific stellar angular momentum proxy λ_R starting from SPH luminosity-weighted velocity and velocity dispersion maps as defined in Emsellem et al. (2007):

$$\lambda_R = \frac{\sum_i F_i R_i |V_i|}{\sum_i F_i R_i \sqrt{V_i^2 + \sigma_i^2}} \quad (3.7)$$

with i the pixel index, F_i its flux, R_i the distance of the pixel from the galaxy center, with V_i the mean line-of-sight velocity of a pixel and σ_i its velocity dispersion. This parameter has been introduced to better capture the spatial information included in the kinematic maps. As opposed to the classical v/σ indicator, λ_R has been designed to distinguish between galaxies with kinematically decoupled components (KDC), which in some cases exhibit large v/σ typical of rotation-supported galaxies, despite their rotation being confined to the central regions.

An example of the maps from which λ_R is computed for our simulation setup are shown in Figure 3.17. The V_{LOS} and σ map are computed with SPH interpolation, using the luminosity in V-band to weight the contribution of particles along the line of sight. Some authors (e.g. Schulze et al., 2018; Pillepich et al., 2019) use non-weighted quantities taken directly from the particles to compare simulations and observations. This approach makes the comparison with observations more difficult since all the information that we get is luminosity weighted (Walo-Martín et al., 2020).

It is possible to compute the radial profile of $\lambda_R(r)$ including in the summation of eq. (3.7) only those pixels that have a galactocentric distance smaller than r . The profile itself and the value $\lambda_R(R_e) = \lambda_{R_e}$ is used to distinguish between fast and slow rotators. Emsellem et al. (2007) defines galaxies with $\lambda_{R_e} < 0.1$ as “slow rotators” and those with $\lambda_{R_e} > 0.1$ as “fast rotators”. While falling into the cluster, galaxies evolve from being classified as having a fast-rotator profile to slow rotator (cf. also Emsellem et al., 2011). We show an example of the profile in Figure 3.19, for simulation ID 69 as a function of time. It is clear that, in a time-frame that is short compared to the lifetime of the galaxy, λ_R undergoes significant changes, both locally, as a function of radius, and averaged over the whole galaxy. In particular, the changes are large enough to cause the galaxy to cross the slow/fast rotator classification threshold. Also, it is worthwhile to note that the value of r adopted affects whether a galaxy is classified or not as a slow rotator.

3 Simulation results

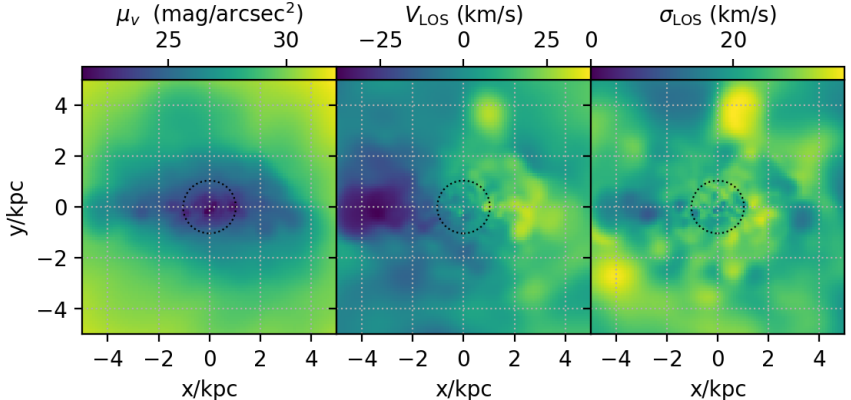


Figure 3.17: μ_v surface brightness map and SPH v-band luminosity weighted maps of line of sight velocity and velocity dispersion σ for a snapshot of the simulation ID 69 around first pericenter passage. The galaxy is projected edge-on, with the angular momentum vector lying on the xy plane. A dotted circle of radius R_e is shown.

There is a complex interplay between R_e , σ and the rotational velocity while the galaxy is on its orbit. R_e increases with time whereas velocity dispersion and the rotation velocity at a fixed radius tends to decline. No single phenomenon can be called to explain the λ_R profile behaviour. The result of this joint evolution is λ_{R_e} decreasing with time.

It has been shown in the SMAKCED survey of 39 early-type galaxies in the Virgo cluster (Toloba et al., 2014, 2015) that the so classified fast-rotator galaxies in the outer region of the cluster rotate faster than the fast rotators in the center of the cluster. Therefore, in this case, observed specific angular momentum λ_R is correlated with cluster-centric distance. It is indeed hypothesized, that after pericenter passages and a long time in the cluster, galaxies are heated up and transformed into slow rotating dEs. This scenario is confirmed by our simulations where dwarf irregulars are converted into early-type galaxies, and with time their kinematics is transformed into the one of slow rotators.

In our case, however, the correlation of λ_R with clustercentric distance is mild and affected by the very noisy and time-dependent nature of the angular momentum proxy. For example in simulation ID 69, as shown in Figure 3.20, λ_R behaviour is very oscillatory and fails to distinguish pericenter passages unequivocally.

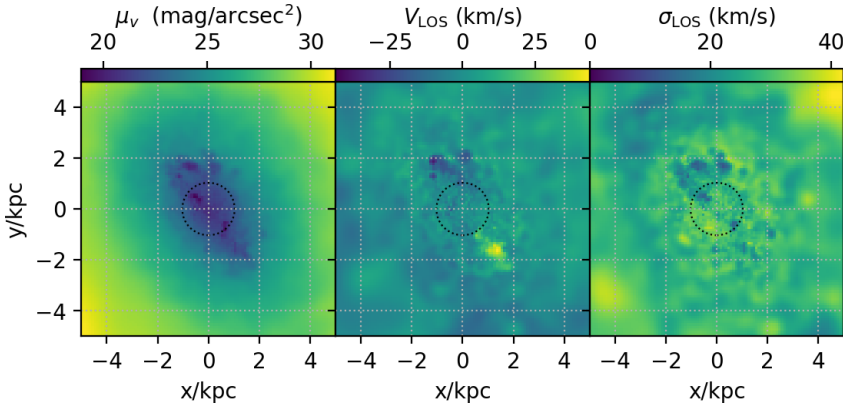


Figure 3.18: Same as Figure 3.17 for simulation ID 41. Note the peak in V_{LOS} outside of R_e .

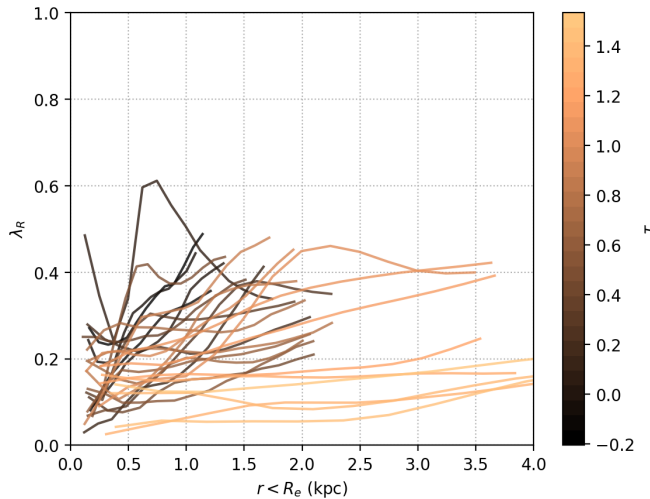


Figure 3.19: λ_R profiles for ID 69 on a 100 kpc orbit color coded with time normalized by radial period. The λ_R profile is shown up to the corresponding R_e .

3.5.3 Relation between λ_R and physical angular momentum

In Figure 3.20, in order to compare λ_R and the angular momentum of the galaxies in an observationally motivated way, we chose to observe the

3 Simulation results

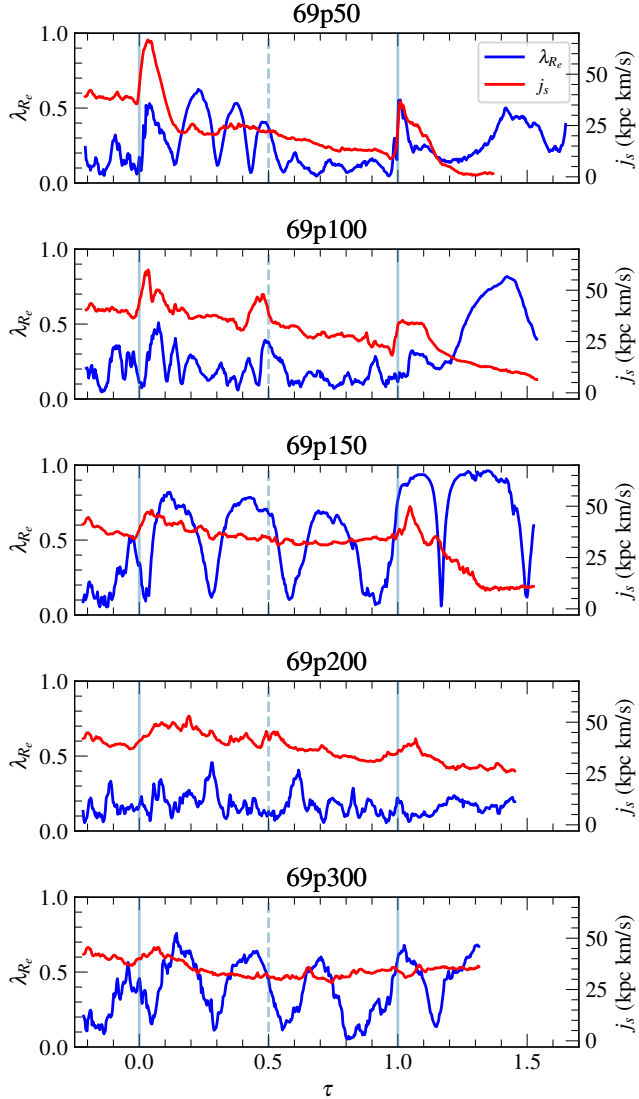


Figure 3.20: Stellar specific angular momentum proxy λ_R and specific angular momentum of star particles j_s for the simulation ID 69 on multiple orbits. The measurements have been taken by observing the galaxy from the plane of the orbit, recreating the condition of a fixed observer. Note the relatively stable values of j_s (a conserved quantity) compared to the oscillatory nature of λ_R , which oscillates by more than 50%.

galaxy from the plane of the orbit, not changing its point of view along its evolution. Given the spin of the galaxy in correspondence of the pericenter (as shown in the previous section), from this point of view the pericenter passage should be visible in λ_R at the highest extent. In Figure 3.20, j_s is the norm of the specific angular momentum vector and it is in fact affected by pericenter passages for radial orbits, whereas it is relatively conserved for more circular orbits.

It is striking how λ_R oscillates along the orbit (e.g. see panel 69p150) and this highlights how inherently variable λ_R is. It is thus clear that - at least for the class of galaxies we consider - the snapshots in Figure 3.19 are not representative of the mean value of λ_R , and an instantaneous measurement of λ_R cannot be used to classify a galaxy as slow/fast, because of the large time-dependent variation.

Emsellem et al. (2007) in their Appendix A, present a description of three main effects at play when trying to recover the apparent angular momentum: projection effects, luminous distribution and mass distribution of the galaxy. In their formal exposition, they describe the approximations made to relate λ_R (which is obtained from the properties of the galaxy measured from the point of view of the observer) to the intrinsic spin parameter λ (Binney & Tremaine, 2008, p. 757):

$$\lambda = \frac{J\sqrt{|E|}}{GM^{2.5}} = \frac{j\sqrt{|E|/M}}{GM}, \quad (3.8)$$

where $J = jM$ is the total angular momentum, M the galaxy of the mass and $E = T + W$ the total energy of the system, where $T = 1/2 M V_{\text{rms}}^2$ and $W = -GM^2/r_g$ the kinetic and potential energy, respectively, which are linked by the scalar virial relation $T = -\frac{1}{2}W$.

The approximations of using the projected radius R instead of both the gravitational radius r_g and the distance from the spinning axis r , are taken into account through the coefficients κ_R and κ_J ; similarly, using the second order velocity moment $V^2 + \sigma^2$ instead of the mean-square speed of the system V_{rms}^2 , is considered through the coefficients $(\kappa_V, \kappa_\sigma)$. All in all these four coefficients grasp the effects of projection and of the luminous and mass distribution:

$$\left\{ \begin{array}{ll} j &= \kappa_J \langle R|V| \rangle, \\ 2E/M = V_{\text{rms}}^2 &= -\langle \kappa_V V^2 + \kappa_\sigma \sigma^2 \rangle, \\ GM &= \kappa_R \langle R (\kappa_V V^2 + \kappa_\sigma \sigma^2) \rangle. \end{array} \right. \quad (3.9)$$

In the case of λ_R the coefficients are set to: $\kappa_J/\kappa_R = \sqrt{2}$, $\kappa_V = \kappa_\sigma = 1$.

Comparing λ_R with observables

Given the possible interest observers may have in how much λ_R is a tracer of the apparent angular momentum, we investigated the relation between the two in our simulations setup (cf. the work of Walo-Martín et al., 2020). We tried to use λ_{R_e} as a starting point to compute the physical angular momentum. To do so, we try to retrieve an approximate formula for the specific angular momentum which relies on observable quantities:

$$j_s^* = \lambda_{R_e} R_e \sigma_e \quad (3.10)$$

where σ_e is the line-of-sight velocity dispersion of star particles measured within an aperture of R_e . For a fair comparison we compute the specific angular momentum j_{se} of star particles within R_e (the projected effective radius).

$$\mathbf{j}_{se} = \sum_{i \in S} \mathbf{r}_i \times \mathbf{v}_i, \quad \text{where } S \equiv \{i : \|\mathbf{r}_i\| < R_e.\} \quad (3.11)$$

The relation between $j_{se} = \|\mathbf{j}_{se}\|$ and j_s^* is shown in Figure 3.21. To simplify the treatment, as a first approximation, the snapshots have been rotated edge-on.

It is interesting to see how for the case of simulation ID 69 in Figure 3.21a the order of magnitude of j_s^* is strikingly in accord with the measured j_{se} from the particles. In contrast, for simulation ID 41, there is no correlation. Given that ID 41 shows an unusual velocity profile (the peaks of the line-of-sight velocity lay outside of R_e , as shown in Figure 3.18) we hypothesize that the limited radius used to compute λ_{R_e} may cause the discrepancy. Accordingly, we inspected the possibility that by computing both j_{se} and j_s^* within $2R_e$ a tighter relation between them would emerge. Figure 3.22 does not support this theory, and the gap between j_{se} and j_s^* increases for the doubled radial limit.

We conclude that in the dwarf-irregular regime covered by our simulations the adapted proxy j_s^* computed in equation (3.10) is not a good tracker of angular momentum.

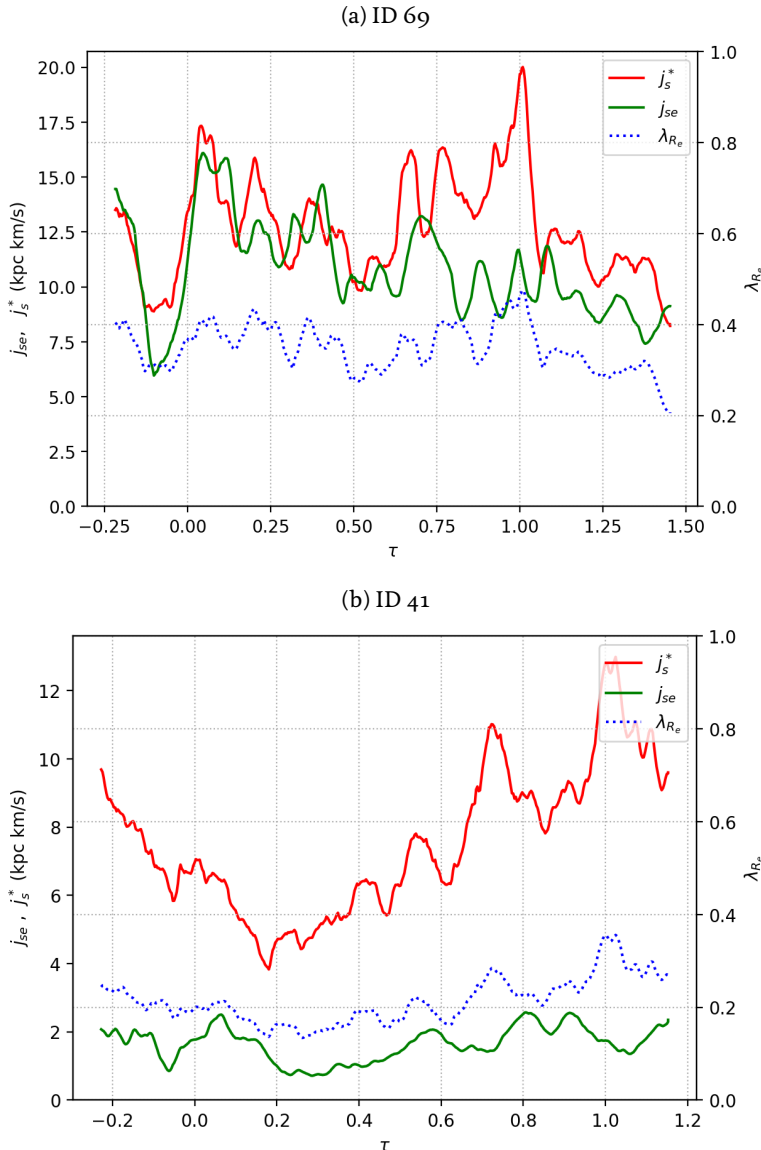


Figure 3.21: Comparison between specific angular momentum j_{se} and λ_{Re} at the effective radius for simulation ID 69 and ID 41 on a 200 kpc orbit. λ_{Re} is computed viewing the galaxy side-on. Curves are smoothed using a rolling average of 0.2 Gyr.

3 Simulation results

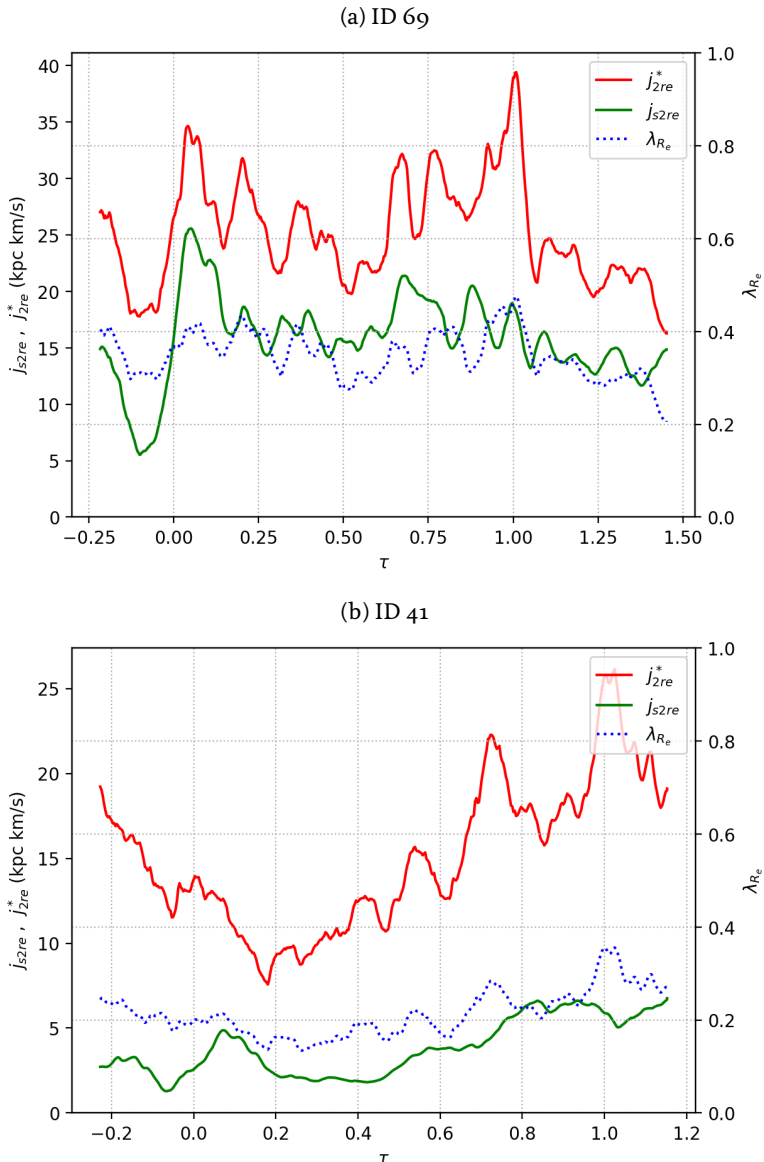


Figure 3.22: Same as Figure 3.21, but using the limit of $2R_e$ to compute j_{se} and λ_R .

Insights from simulations into the formation of the peculiar dwarf galaxy NGC 1427A

4

Abstract

We present a scenario for the formation and the morphology of the arrow-shaped dwarf irregular galaxy NGC 1427A in the Fornax Cluster. This galaxy shows intriguing stellar and gaseous tails pointing in different directions for which alternative but not conclusive formation scenarios have been proposed in the literature. We performed N -body/SPH simulations of dwarf galaxies falling into a model of the Fornax cluster, exhibiting a jellyfish-like appearance while undergoing ram-pressure stripping. We noted that some of our models show interesting tail morphologies similar to that of NGC 1427A. In this way, the peculiar NGC 1427A structure can be studied using models whose stellar and neutral gas photometry and kinematics are in good agreement with the observed ones, without the need of invoking an interaction with a nearby galaxy. Thanks to the tails, we can identify the requirements for a galaxy to expose such a structure and assess the possible position and velocity of the galaxy in the cluster. This puts constraints on the orbit of the galaxy, its position in the cluster and the time since its pericenter passage. From the statistics of identified snapshots following our modelling, we found that the most likely position of the galaxy is around 200 kpc in front of the cluster center, travelling towards the cluster with a velocity angle with respect to the line-of-sight direction of around 50 deg. This analysis can be useful in future observations of similar galaxies in clusters to characterise their position and velocity in the cluster and their formation.

The distorted optical appearance and gaseous tails and overall jellyfish-like morphology – barring currently active star formation in the gas tails – of NGC 1427A (Figure 4.1) seems to be straightforwardly and satisfactorily explained by ram-pressure stripping in conjunction with cluster tidal forces. In particular, as has been explored more in detail in Chapter 3, star formation flickers on and off inside the gaseous tails of simulated ram-pressure stripped dwarf galaxies as gas clumps condense and disperse

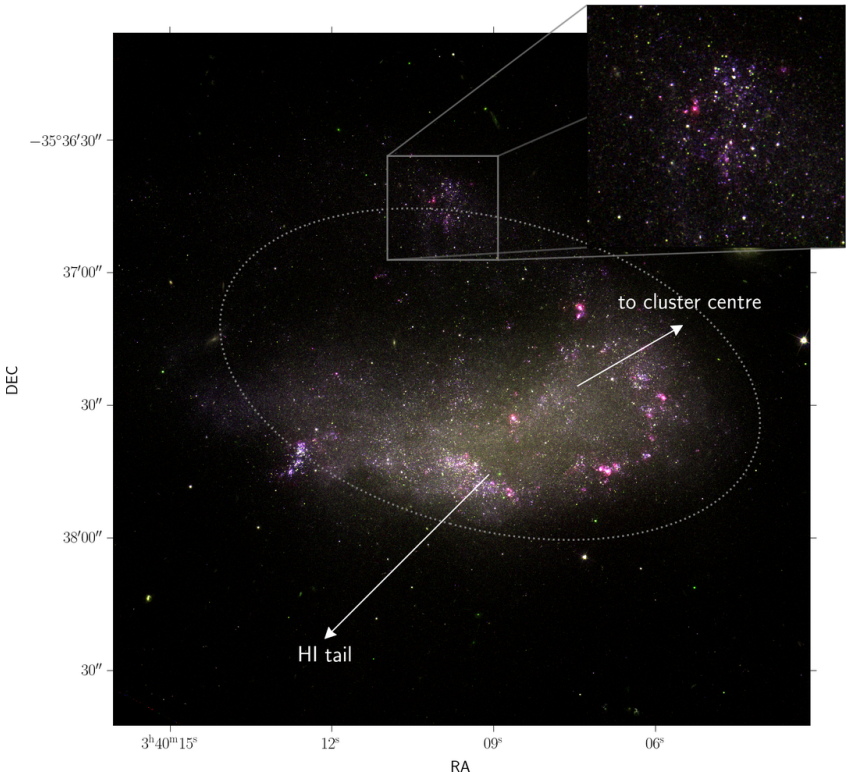


Figure 4.1: False-colour image of NGC 1427A, based on HST Advanced Camera for Surveys (ACS) archival data (Proposal ID: 9689; PI: M. Gregg). The following colour bands were used: blue=475W; green=775W; red=625W+660N (stellar emission was subtracted from the 660N image using a scaled 775W image). This colour scheme makes the H α emission stand out in red. An asinh stretch was applied to bring out also the faint details. The inset zooms in on the Northern Clump, showing it to be composed of two loose stellar clusters with embedded HII emission. The Northern Clump also appears to be connected to the north-west rim of NGC 1427A's main body via a tenuous stream of stars. The directions of the HII tail and towards the Fornax Cluster center are indicated with arrows. The dotted ellipse is the same as in Figures 1 and 2 of Lee-Waddell et al. (2018) and indicates the shape and direction of the faint outskirts of the galaxy, which are quite distinct from the system's inner, brighter parts.

again. This gives the label “jellyfish galaxy” a transient and possibly recurrent quality.

To correctly interpret the available data, it is of prime importance to be able to reliably identify the dominant transformation process for this galaxy. With this goal in mind, we compare recent H α and optical data of NGC 1427A with a suite of dwarf galaxy simulations, set in a Fornax Cluster environment.

In the next section, we give a short overview of the observed properties of NGC 1427A and focus on those that are considered most relevant for elucidating its origin and evolution. The methodology behind the comparison of these simulations with the observations is discussed in Section 4.3. We conclude with a discussion of the main results in Section 4.4.

4.1 Observed properties of NGC 1427A

NGC 1427A is a gas-rich dwarf irregular galaxy in the Fornax Cluster. Recessional velocity measurements indicate that NGC 1427A is moving with a line-of-sight velocity of around 2028 km/s (Bureau et al., 1996; Schröder et al., 2001). Accordingly, if we assume NGC 1399 to be the cluster center, NGC 1427A travels away from us at a projected speed of around 700 km/s relative to the cluster center. NGC 1427A has a projected distance of 137 kpc from NGC 1399¹.

A false-colour HST image of the galaxy is shown in Figure 4.1. The inset of Figure 4.1 zooms in on the Northern Clump, showing it to be composed of two loose stellar clusters with embedded HII regions. The Northern Clump also appears to be connected to the north-west rim of NGC 1427A’s main body via a tenuous stream of stars. The directions of the H α tail and towards the Fornax Cluster center are indicated with arrows. The dotted ellipse is the same as in Figures 1 and 2 of Lee-Waddell et al. (2018) and indicates the shape and direction of the faint outskirts of the galaxy. We interpret these low-surface-brightness stellar features, which point towards the north-east and south-west (effectively captured by the ellipses in Figure 4.1 and 4.2c), as quite distinct from the much brighter inner regions of the galaxy’s main body, as tidal features. The Northern Clump, which we discuss in detail in Section 4.4.2, may be associated with these tidal features.

Chanamé et al. (2000) presents a lower limit for the dynamical mass of NGC 1427A using a rigid-body rotation model: $M_{\text{dyn}} > (9 \pm 3) \times 10^9 M_\odot$.

¹The angular separation is 1373 arcsec = 137 kpc, throughout the paper, we assume a fiducial distance of the cluster center of 20 Mpc.

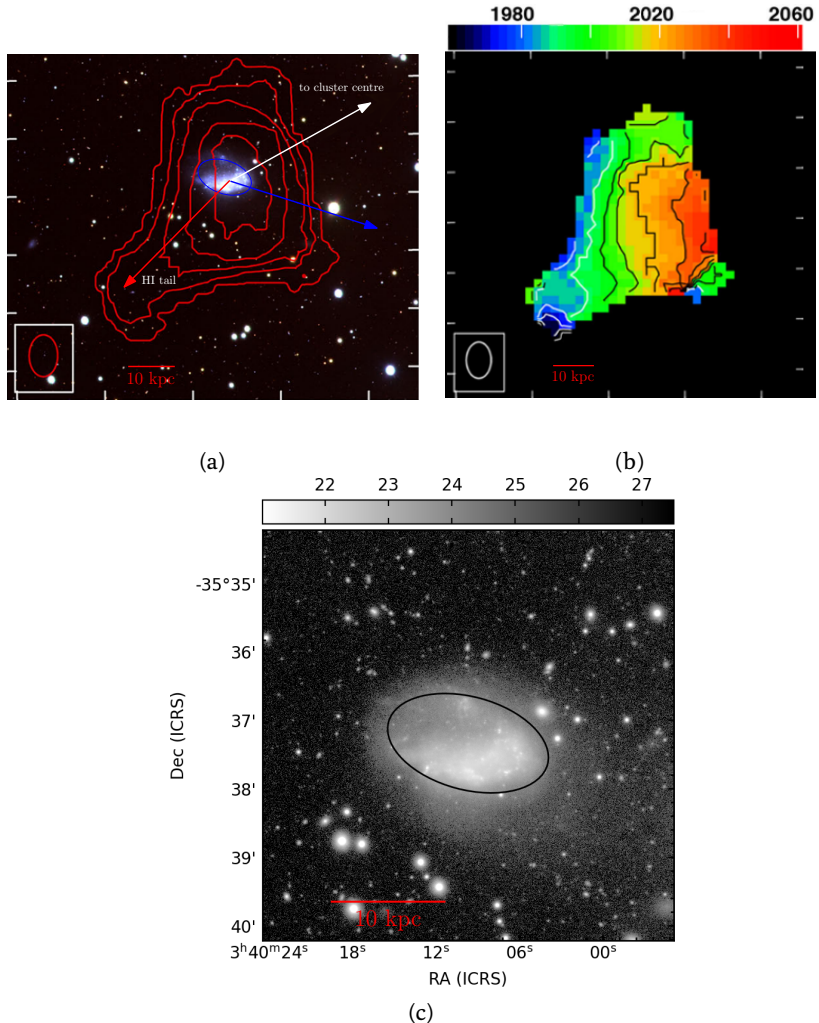


Figure 4.2: Images of NGC 1427A from Lee-Waddell et al. (2018) for illustrative purposes: (a) VST image with overplotted in red contours of constant HI column density at levels $(0.5, 1, 2, 5, 10) \times 10^{20}$ amu cm $^{-2}$; (b) gas kinematics (recessional velocity in km/s); (c) r' -band image (in mag/arcsec 2). A length scale at the assumed cluster distance is indicated in red.

Following the calibrated empirical relation of Taylor et al. (2011), the stellar mass estimated by Lee-Waddell et al. (2018) is $M_* \approx 10^9 M_\odot$ while its total HI mass is determined to be $M_{\text{HI}} = (2.1 \pm 0.2) \times 10^9 M_\odot$. The galaxy has a conspicuous HI tail, containing about 10 per cent of all HI gas in NGC 1427A, pointing towards the south-east as well as stellar tidal extensions along a north-east to south-west axis. In other words: the gaseous and stellar extensions are almost perpendicular to each other. NGC 1427A was not detected in CO emission, providing an upper limit on its molecular gas mass of the order of $M_{\text{H}_2} \sim 10^8 M_\odot$ (Zabel et al., 2019). These authors report the detection of a single 3 mm continuum source without an optical counterpart but its nature remains unclear. A distinct young stellar clump is visible in the northern rim of the galaxy. On high-resolution images, this clump, the rim, as well as the galaxy's main stellar body are resolved into many individual OB associations and clusters, some with accompanying H α -emission (Hilker et al., 1997; Sivanandam et al., 2014). Clearly, star formation proceeds in many dispersed small bursts.

Various hypotheses regarding the evolution of NGC 1427A, and especially its extraordinary configuration of tails, have been proposed. These include recent interactions with other nearby galaxies (Cellone & Forte, 1997), a merger with an object that now forms the northern stellar clump (Lee-Waddell et al., 2018), the tidal interaction with the cluster potential, and ram-pressure stripping of its gas by the cluster hot gas halo (Chanamé et al., 2000; Mora et al., 2015).

To try and identify the environmental processes acting on NGC 1427A, we first selected those properties of this dwarf galaxy that were most likely to be indicative of those processes and not of internal effects. Those are:

1. the direction towards the Fornax cluster centrum,
2. the direction of the axis of the stellar tidal extension,
3. the direction of the HI tail.

These parameters are most tightly linked with NGC 1427A's orbit through the Fornax Cluster and are expected to be relatively insensitive to the accidents and vagaries of its evolution before its acquisition by the cluster.

Thus, our analysis differs from that of Lee-Waddell et al. (2018) where the ram-pressure hypothesis is discussed based on stellar colour and galaxy morphology information. Their new data indeed rule out a ram pressure origin for the optical appearance of the galaxy, but they leave open the question whether ram pressure may have played a role in the formation of the HI tail.

4.2 Simulations

The simulations used in this chapter are described in full details in Section 2.6. We stress that they have not been set up to mimic NGC 1427A in any particular way. Therefore, not all details can be expected to exactly match with observations. Nonetheless, these simulations provide valuable insights not only into the phenomena at play but, more importantly, they can be used to infer the most likely current orbital phase of the galaxy.

4.3 Constraining the orbital phase of NGC 1427A

4.3.1 Quantitative morphological search

We carried out a systematic search among all the simulation snapshots, portraying different dwarfs at different times on different orbits. We observed each snapshot from different points of view in order to select the snapshots and their orientation most resembling the observed galaxy using four measurable quantities:

- (i) the projected cluster-centric distance, r_p ;
- (ii) the line-of-sight velocity with respect to the cluster center, v_p ;
- (iii) the position angle of the outer isophotes, quantified as the angle α between the projected cluster center direction and the direction of the 26.5 mag/arcsec² isophote in r' band, see Figure 4.4;
- (iv) the orientation of the HI tail as measured with the angle β between the isophote orientation and the direction of the highest variance of the image obtained by computing the second order moments of the HI SPH map (Stobie, 1980).

We highlight that the search has been carried out using only morphological and orbital parameters, given our focus on the peculiar morphology of NGC 1427A. Moreover, the criteria used to compare simulations to observations are the ones that best represent the effects of the cluster environment: the relative directions of the tidal pull and the ram pressure stripping. Indeed, the first two requirements put constraints on the orbital position and hence on the orbital phase of the simulated dwarf. The latter two require that the isophotal tail and the neutral gas tail are oriented as in NGC 1427A. By selecting a faint isophote for criterion (iii) we are tracing the outer tidal extensions of the stellar body. Inspection of the evolution of the direction of the principal axes of the stellar density distribution along a simulated dwarf galaxy's orbit shows that the galaxy outskirts

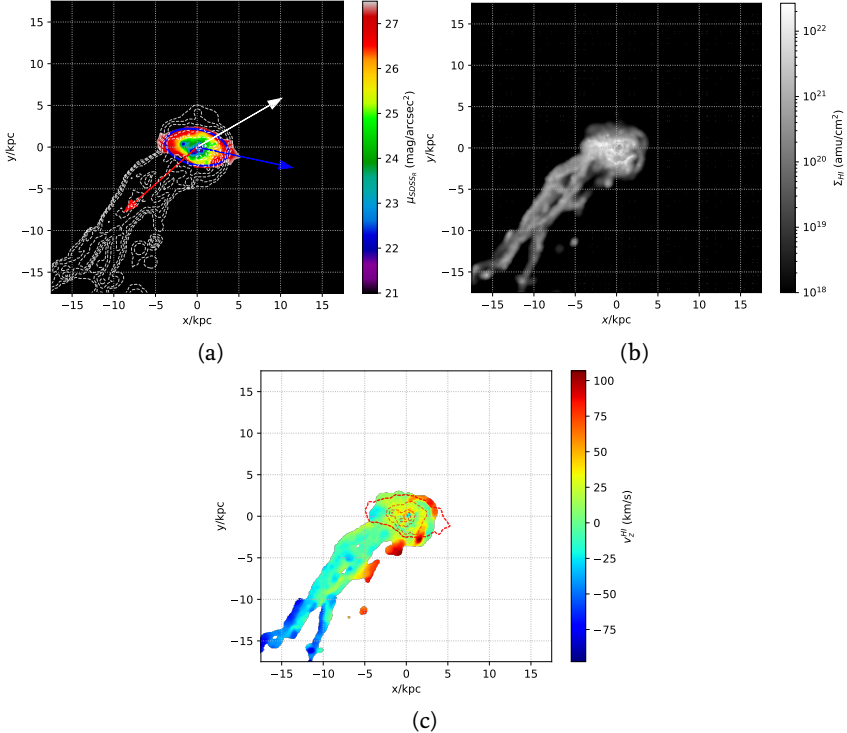


Figure 4.3: A simulation snapshot (ID 68, see Table 2.1) on an orbit with 100 kpc pericenter distance, showing stellar tidal and gaseous stripped tails. (a) r' -band surface brightness with HI column density contours as seen from a point of view for which the projected cluster-centric distance $r_p = 77 \text{ kpc}$ and the recessional velocity -793 km/s . HI contours are drawn at column density levels $[10^{17}, 10^{18}, 10^{19}, 10^{20}, 10^{21}] \text{ amu cm}^{-2}$. The white arrow points towards the cluster center, whereas the blue and the red arrows are the computed orientation of the stellar tail and the gaseous tail respectively, see Section 4.3.1. (b) The column density of the neutral hydrogen, highlighting clumpy blobs of stripped HI . (c) SPH map of the HI velocity field where the HI tail in its rightmost part is receding more than the more detached part. For reference, the $[22, 24, 26, 28]$ mag/arcsec 2 isophotes are shown as dashed red contours. We stress that our Fornax cluster dwarf galaxy simulations were not designed to reproduce all the details of this particular galaxy. Nonetheless, remarkable similarities can be found.

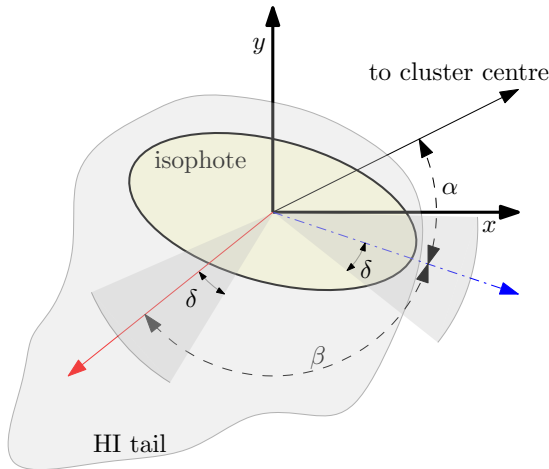


Figure 4.4: Angles α, β definitions used to set up the requirements for the morphological search. δ is the angle tolerance used for the selection. Blue and red arrows are defined as in Figure 4.3a. Darker grey shaded regions are the allowed directions of the oriented snapshots tidal stellar tail and HI tail.

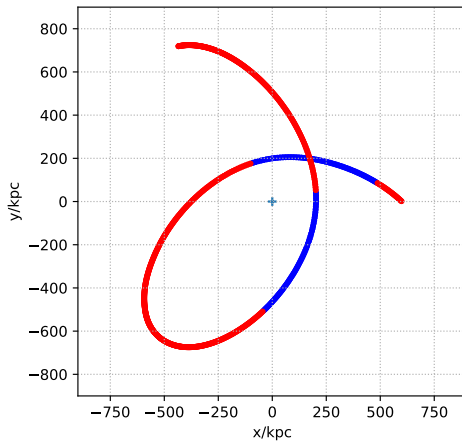


Figure 4.5: A trajectory with pericenter of 200 kpc. In blue the orbital phases for which there are snapshots with projected distance and recessional velocity compatible with the ones of NGC 1427A (i.e. snapshots fulfilling requirements (i)-(ii)) for some points of view. In this case $r_p = 137$ kpc, $v_p = -693$ km/s.

rapidly forget their initial spatial orientation and become strongly aligned with the cluster center around pericenter and apocenter. On the inward or outbound legs of a galaxy's orbit, this elongation occurs parallel with its orbital velocity. This evidence for a tight correlation between a dwarf galaxy's elongation and its orbital phase, led us to include criterion (iii).

From VST images of Lee-Waddell et al. (2018) (originally from the deep survey presented in Iodice et al., 2016) we used the position angle of 15 deg of the fitted ellipse in its Figure 2. From the HI maps of Figures 1 and 3 of the same paper (see Figures 4.2a and 4.2b above) we assumed an inclination of the HI tail of -135 deg (pointing south-east). Given that the direction of the cluster center is around 30 deg north-west, the resulting target angles are $\bar{\alpha} = 45$ deg, $\beta = 120$ deg, as in Figure 4.4.

For each snapshot, we started by finding the orbital phase which fulfils the first two requirements. Each requirement is satisfied by the set of points of view constituting the generatrices of a cone centered on the galaxy position. By intersecting two cones it is possible to find the points of view satisfying the requirements. This is equivalent to solving a quadratic equation (see Section 4.3.2) whose two solutions are two points of view satisfying the requirements (i) and (ii). Each snapshot is then rotated as if it was observed from the peculiar point of view yielding the imposed cluster-centric distance and the recessional velocity. The more radial the orbit is, the higher the number of suitable snapshots which will be further selected using requirements (iii) and (iv), see Figure 4.5.

With the assumed cluster center at a distance of 20 Mpc from us (see Section 4.1), we imposed as targets the two quantities $\bar{r}_p = 137$ kpc and $\bar{v}_p = -693$ km/s with measures for NGC 1427A (the projected distance on the sky and recessional velocity of NGC 1427A relative to NGC 1399). In order to take into account uncertainties in the measured \bar{r}_p and \bar{v}_p and to capture the sensitivity of the procedure to the selected projected distance and recessional velocity, we repeated the same procedure for each simulated snapshot but allowing for other slightly offset targets r_p and v_p . Practically, we fixed an offset in both quantities $r_p = \bar{r}_p \pm \Delta r$, $v_p = \bar{v}_p \pm \Delta v$ with $\Delta r = 100$ kpc, $\Delta v = 60$ km/s. Also we added four other targets: $(\bar{r}_p \pm \Delta r, \bar{v}_p)$ and $(\bar{r}_p, \bar{v}_p \pm \Delta v)$ with same $(\Delta r, \Delta v)$ as before. Including the exact target \bar{r}_p, \bar{v}_p , at the end, we had nine targets to check for each snapshot. In total, we obtained a dataset of 424,656 oriented snapshots.

For each snapshot surviving the selection of requirements (i) and (ii) and oriented so that r_p and v_p are the ones imposed, we created the surface brightness map and HI map. We first fitted an ellipse to the contour corresponding to the 26.5 mag/arcsec² isophote in r' band. We computed the second order moments of the HI map to obtain the direction of the neutral hydrogen tail. Since we are interested in snapshots with an elon-

gated H α tail in the South-East direction, we further selected only oriented snapshots with galactic projected velocity on the plane of the sky having a positive projection on the cluster center direction. This removes false positives with a H α tail inclined with the proper angle but extending towards the cluster center (from the image moments only the direction is returned, not the sense of elongation of the tail). At the end of this pre-selection, we ended up with 59,896 oriented snapshots.

We then used requirements (iii) and (iv) to further refine the search. In the following section we shall determine the distribution of the snapshots with tails similar to the observed galaxy using angles α and β , described above, and a tolerance δ :

$$\bar{\alpha} - \delta < \alpha < \bar{\alpha} + \delta, \quad \bar{\beta} - \delta < \beta < \bar{\beta} + \delta$$

The selection tolerance δ is then our main knob to filter-out snapshots oriented as NGC 1427A with angles $\bar{\alpha}$ and $\bar{\beta}$. The dependence of the results (and the number of oriented snapshots surviving the selection criteria (i-iv)) on its choice is quite strong, so in all the following histograms we highlight the δ chosen.

4.3.2 Finding points of view - cones intersection

Finding the point of views from which the galaxy appears as having the target projected clustercentric distance (r_p) and the proper line-of-sight velocity (v_p) is equivalent to solving the problem of intersecting two cones.

Given \vec{x} the unit vector representing the direction of the point of view, and \vec{r} and \vec{v} the clustercentric position and velocity of the galaxy respectively, we can write the following conditions:

$$\begin{cases} \vec{x} \cdot \vec{v} = v_p \\ \vec{x} \cdot \vec{r} = \pm R \\ |\vec{x}|^2 = 1 \end{cases} \quad (4.1)$$

where $R = \sqrt{r^2 - r_p^2}$. By using $[\vec{r}, \vec{v}, \vec{r} \times \vec{v}]$ as basis (right-handed but not orthogonal), it is possible to express \vec{x} as:

$$\vec{x} = a\vec{v} + b\vec{r} + c(\vec{r} \times \vec{v}). \quad (4.2)$$

Substituting into (4.1):

$$\begin{cases} av^2 + b(\vec{r} \cdot \vec{v}) = v_p \\ a(\vec{r} \cdot \vec{v}) + br^2 = \pm R \\ |\vec{x}|^2 = 1 = av^2 + br^2 + c^2|\vec{r} \times \vec{v}|^2 + 2ab(\vec{r} \cdot \vec{v}) \end{cases} \quad (4.3)$$

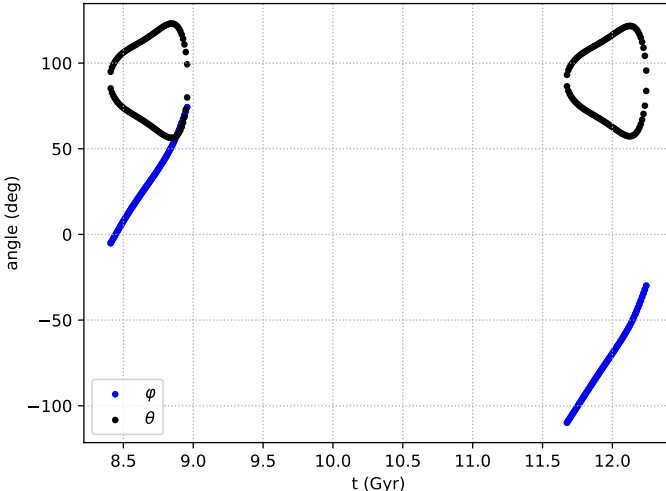


Figure 4.6: Angles φ, θ defining the points of view of each snapshot of the trajectory of Figure 4.5. The angles are used to rotate the selected snapshots in order to obtain the target r_p, v_p . Only a subset of snapshots can be oriented to fulfil the requirements.

The last quadratic equation yields immediately two values of c (c_1, c_2).

For each chosen sign of R , the system yields two solutions: (\vec{x}_1, \vec{x}_2) which can be used to rotate the galaxy snapshot as if it was seen from the directions \vec{x}_1 and \vec{x}_2 .

Each direction can be defined using two angles (φ and θ) representing the spherical coordinates of the unit vectors \vec{x}_1 and \vec{x}_2 .

In Figure 4.6 an example of rotation angles for a particular simulated orbit is shown. The angles φ and θ are used to rotate the simulated galaxy as if it was observed from the peculiar point of view yielding the imposed clustercentric distance r_p and the recessional velocity v_p .

4.3.3 Distribution along the orbit of points of view satisfying the requirements

We computed the distribution of selected oriented snapshots with respect to the time from the pericenter passage. We noted that all the snapshots surviving the selection are found within 200 Myr of a pericenter passage.

We ascertain the robustness of this result by varying the tolerance δ of the comparison of the angles α, β with the observed ones. Our orbital and morphological criteria are preferentially met by simulations with a stellar

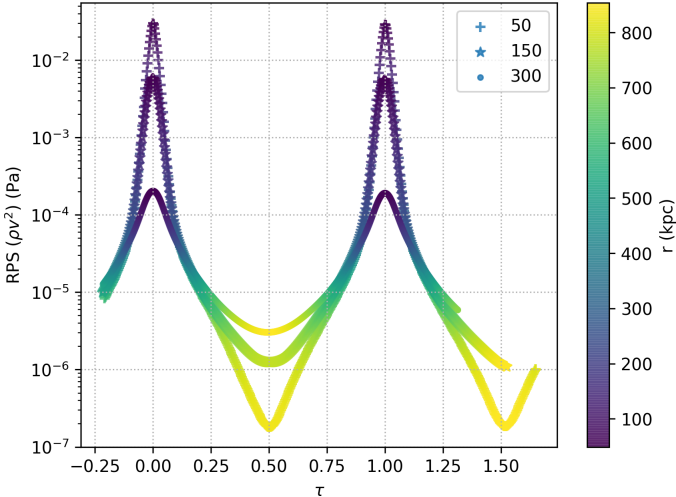


Figure 4.7: The strength of the ram pressure (ρv^2) as a function of normalised time τ (cf. equation (3.2)) for the ID 69 simulations on multiple orbits (orbit pericenter in kpc is indicated in the legend). The colour scales traces orbital distance with respect to the cluster center.

mass above $\approx 10^8 M_{\odot}$. Less massive galaxies and galaxies on radial orbits are completely stripped from their HI gas, see Figure 4.8, because of the steep increase of ram pressure around pericenter as shown in Figure 4.7. Especially for radial orbits, no oriented snapshot is found on orbits of 50 and 100 kpc after first pericenter passage, regardless of the tolerance δ considered, as shown in Figure 4.9. For the most circular orbits, only snapshots undergoing second pericenter passage survive the selection. This is likely due to the first passage acting as ‘preprocessing’ and making the galaxy potential shallow with higher chances to create tidal tails. In Figure 4.10 we performed the same analysis cumulatively counting all the oriented snapshots (without pericenter distance distinction) but using different isophotes. The diagrams, even if noisier when using fainter isophotes, convey the same message: there is an abundance of correctly oriented snapshots (with tails as NGC 1427A) around first pericenter passage. Indeed, tidal tails as those shown in Figure 4.15, are present in low surface brightness regions of the dwarf, even if they are more difficult to measure. The counterpart in NGC 1427A would be the faint stellar South-West elongation visible especially in r' -band, see Figure 4.2c.

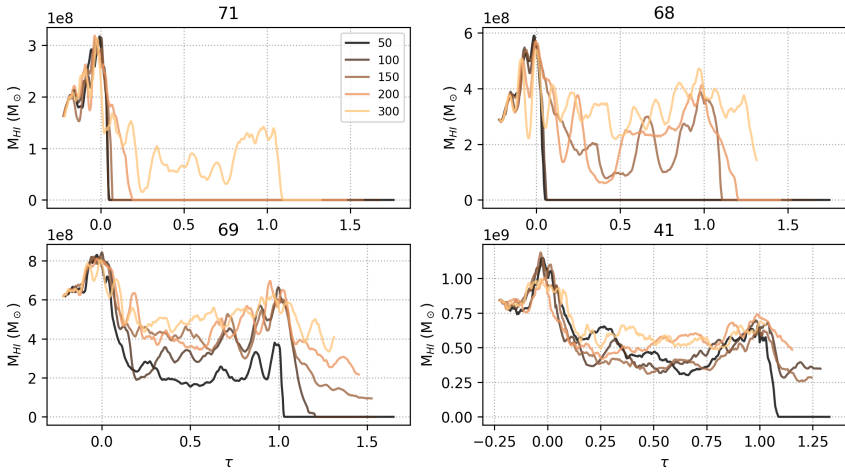


Figure 4.8: Neutral gas mass as a function of normalised time τ as defined in equation (3.2). Each panel is labelled with the simulation ID (cf. Table 2.1) and contains information for the simulated dwarf launched on orbits with different pericenter distances (50, 100, 150, 200, 300 kpc identified by the colour legend in the top-left panel). Gas is compressed when the isolated galaxy enters the cluster and as a consequence it cools down, thus increasing the neutral hydrogen mass. Obviously, around pericenter, ram pressure stripping is effective at driving down the gas mass (as shown also in Figure 4.7).

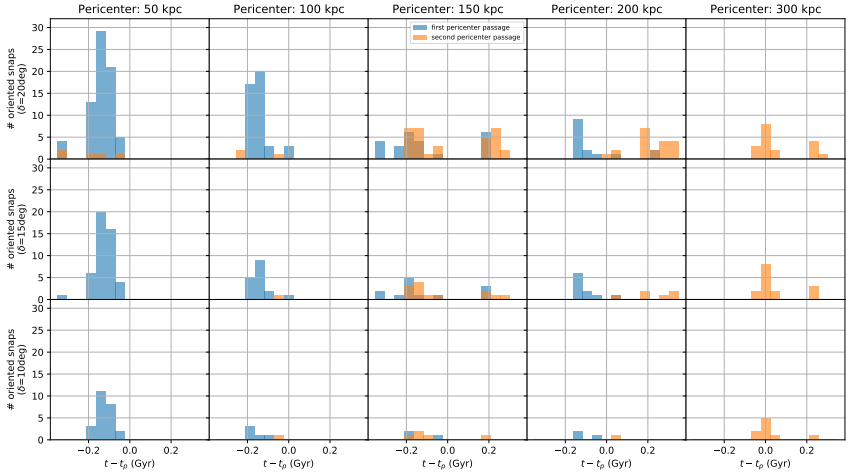


Figure 4.9: Histograms of oriented snapshots fulfilling the requirements (i)-(iv), selected to be around first (blue) or second (orange) pericenter and grouped by orbital pericenter distances (50, 100, 150, 200, 300 kpc). The isophote used to compute the stellar tail inclination is 26.5 mag/arcsec² in r' band. The distribution is peaked at around 150 Myr before pericenter passage, especially in more radial orbits. The result is robust enough to be visible on stricter angle tolerances $\delta = [20, 15, 10]$ deg.

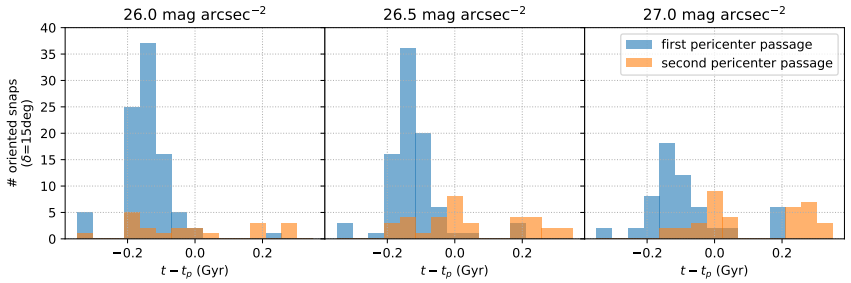


Figure 4.10: Distribution in time relative to pericenter passage of oriented snapshots fulfilling the requirements (i)-(iv) with tolerance $\delta = 15$ deg. Histograms of selected snapshots are coloured relative to their orbital phase: around first (blue) or second (orange) pericenter. Each column corresponds to a different isophote used to compute the stellar tidal orientation. Irrespective of the isophote, the distribution remains peaked around 150 Myr before pericenter passage.

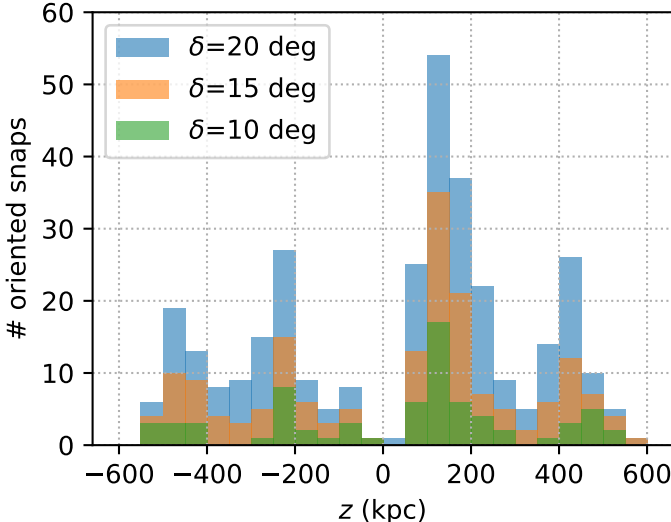


Figure 4.11: Distribution of selected oriented snapshots with multiple tolerance δ along the projected line of sight. The zero point is 20 Mpc, assumed distance of NGC 1399. Positive values mean the galaxy being *in front* of the cluster center.

4.3.4 3D position of the galaxy in the Fornax context

Based on the above described model, we can produce a quantitative estimation of the galaxy projected radial distance. This measure is actually a testable prediction with distance observations. Unfortunately, current uncertainties on the distance measurements do not allow to unequivocally assess the position of the galaxy to be in front or behind the cluster center (Georgiev et al., 2006).

Using our models we can see which is the most likely radial distance relative to the cluster center of a galaxy with morphological features like NGC 1427A. As shown in Figure 4.11, the preferred line of sight distance is around 200 kpc in front of the cluster center.

It is also possible to compute the flight angle γ of the galaxy with respect to the line of sight direction (see Figure 4.13). As shown in Figure 4.12, from the above models, the most frequent is $\gamma \approx 50 \text{ deg}$. Given that the stripped gaseous tail approximately follows the opposite direction of flight, measuring the flight angle in simulations can be useful to assess the real length of the gaseous tail in observations. Our result would indicate the real tail to be roughly a factor 1.3 longer than the projected one.

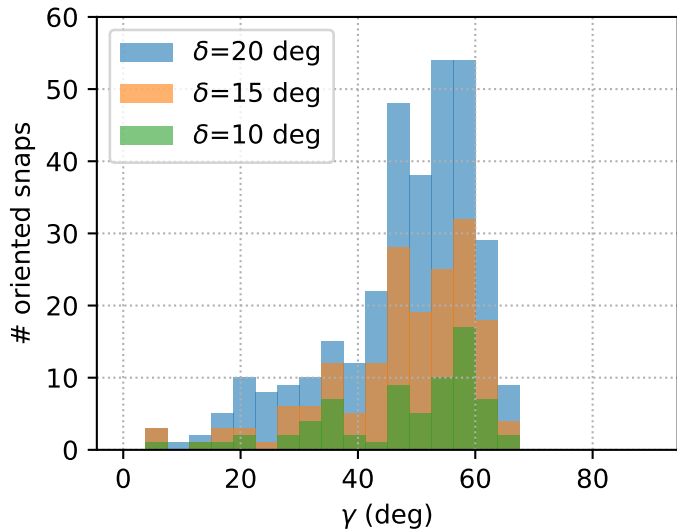


Figure 4.12: Distribution of the flight angle γ of selected oriented snapshots with multiple tolerances δ . γ is defined as the angle between the galactic velocity vector in the cluster reference frame and the line of sight direction.

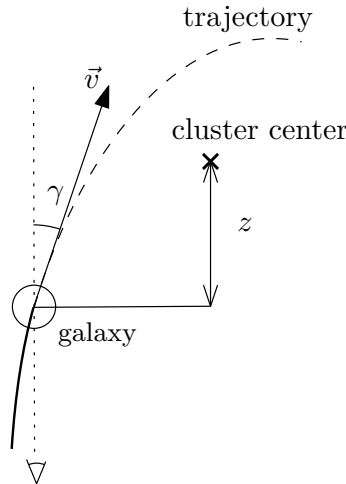


Figure 4.13: Definitions of angle of flight γ and radial distance z . \vec{v} is the orbital velocity of the galaxy.

4.4 Discussion

4.4.1 The asymmetric stellar tidal tails

Including asymmetry as a constraint

As a way of quantifying the asymmetric stellar tides, we computed the non-parametric measure Asymmetry (as defined by Lotz et al., 2004) of our oriented snapshots. For each oriented snapshot we fed its surface brightness map to statmorph (Rodriguez-Gomez et al., 2019) isolating the region of the map within 27 mag/arcsec^2 . As a reference, Su et al. (2021) find an Asymmetry of 0.23 for NGC 1427A. We tried to add the Asymmetry to the constraints described in Section 4.3.1. Given that almost all the oriented snapshots have an Asymmetry higher than 0.2 (in line with the average of 0.53 ± 0.22 for galaxies with intense star formation as reported by Conselice, 2003), we find that isolating snapshots at least as asymmetric as NGC 1427A do not affect the results.

By plotting Asymmetry on selected snapshots as a function of time from pericenter, as shown in Figure 4.14, it can be seen that selected snapshots closer to the pericenter become more symmetric. A possible reason of this can be hypothesised in the tidal pull close to the pericenter which squeezes the galaxy elongating it, hence removing asymmetric regions of the galaxies. Indeed all simulations show an Asymmetry greater than the one of NGC 1427A. We note that this is in line with Rodriguez-Gomez et al. (2019) who find a systematically higher asymmetry for simulated galaxy of Illustris and Illustris TNG (Vogelsberger et al., 2014; Pillepich et al., 2018), especially in the low mass range. In fact, in a numerical simulation each star particle created represents stars of $\approx 1000 M_\odot$: a simulated galaxy is always more "granular" than an observed real galaxy due to the limited resolution.

The origin of the asymmetric stellar tidal tails

An interesting effect of the pericenter passage is the formation of an asymmetric tidal tail, a stellar elongation more pronounced in just one direction, as that shown in the fourth column of Figure 4.15. This effect can be investigated by looking at different simulation snapshots evolving with time around a pericenter passage. We focus our discussion to the case of the galaxy with ID 68 on an orbit with pericenter 100 kpc. In Figure 4.15, the snapshot in the first column is the one who has passed the filters described in Section 4.3.1 and represents a snapshot which is in good agreement to the observation, given its stellar and gaseous tail directions and

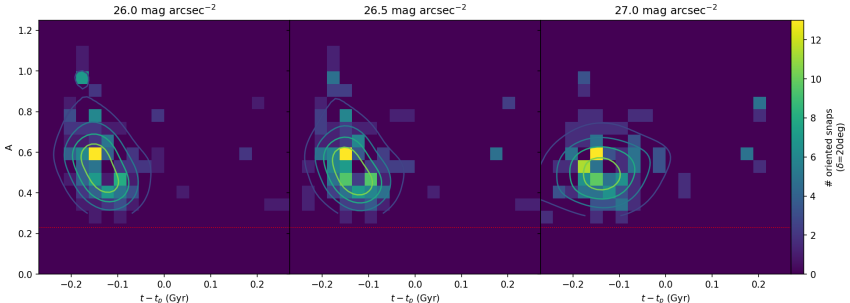


Figure 4.14: 2D histogram of selected oriented snapshots with tolerance $\delta = 20$ deg. The distribution is plotted with time from first pericenter passage on the x axis, whereas on the y axis the Asymmetry non-parametric measure as defined by Lotz et al. (2004). Each column corresponds to a different isophote used to compute the stellar tidal orientation. We overplot a kernel density estimation of the distribution for the snapshots approaching pericenter. The dotted red line corresponds to the measured Asymmetry for NGC 1427A.

the projected clustercentric distance and recessional velocity.

We can then reconstruct a series of events leading to the generation of the leading edge stellar tail. The tidal forces exerted by the Fornax Cluster become markedly asymmetric as a galaxy approaches pericenter on a radial orbit. The steeply deepening gravitational potential well can raise a stronger leading stellar tidal tail while producing a weaker trailing tail during a fast swing-by of a galaxy close to the cluster center. After pericenter, the leading tail twists due to the curvature of the galaxy's orbit, the rapidly changing direction of the gravitational force, and the internal rotation of the galaxy. Effectively the pericenter passage injects energy into the galaxy resulting in a temporary increase of its angular momentum.

At the same time, the gaseous tail is always directed opposite to the instantaneous velocity. The result is that the stellar and gaseous tails are very misaligned, almost orthogonal to each other.

4.4.2 Possible origin of the Northern Clump in NGC 1427A

The galaxy NGC 1427A contains a so called Northern Clump (NC), which has been investigated in detail by some authors (Cellone & Forte, 1997; Hilker et al., 1997). The NC is a clump of blue and very young stars with associated H α emission (Sivanandam et al., 2014). Even on ground-based images, the NC appears to be composed of two sub-clusters, one to the north of the other. This impression is strengthened by the HST image presented in Figure 4.1. The centers of the two sub-clusters are separated by

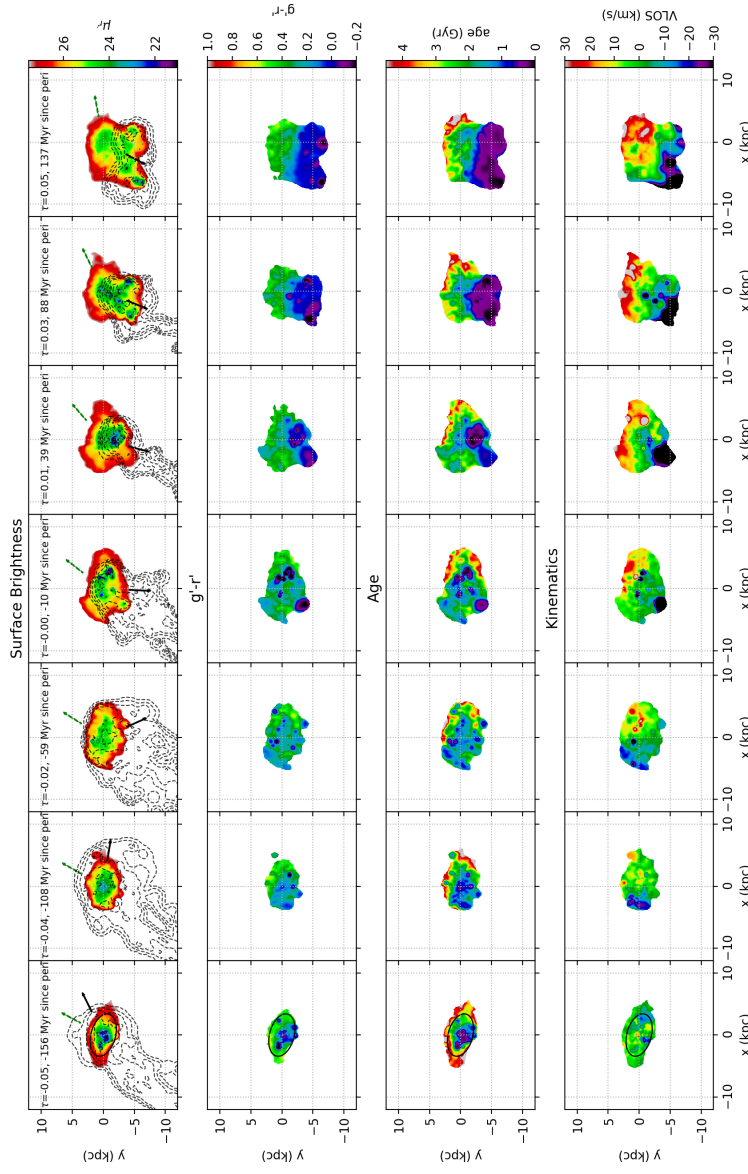


Figure 4.15: Evolution in time of the simulation with ID 68 around first pericenter passage, projected in a way that the first column has $r_p = 1.37$ kpc, $v_p = 693$ km/s, the target values for NGC 1427A. All the other snapshots are seen from the same point of view as the first one. Black arrow indicates the direction to the cluster center whereas the green indicates the instantaneous velocity direction of the galaxy projected on the plane of the sky. In the first column, an ellipse fitted on the 26.5 mag/arcsec² is shown to highlight the direction of the tidal elongation. The first row represents the surface brightness of snapshots around the first pericenter. HI Contours are $[10^{17}, 10^{18}, 10^{19}, 10^{20}, 10^{21}]$ amu cm⁻². Second row the $g'-r'$ colour. Third and fourth row the v-band SPH-average age and velocity of star particles along the line of sight.

7", corresponding to just under 700 parsec. The NC lies on NGC 1427A's projected rotation axis and hence its line-of-sight velocity agrees very well with NGC 1427A's mean recession velocity (Bureau et al., 1996; Chanamé et al., 2000). This does not hint at an external origin for this object. The NC appears to be connected to the north-west rim of the galaxy's main body by a tenuous stream of stars, suggesting it to be displaced along this stream away from the galaxy's main body in a direction that is almost parallel to the major axis of the faint outer isophotes. If, as in our interpretation of the data, these outer isophotes trace the two diametrically opposite stellar tides raised by the Fornax Cluster forces then this would argue for a purely internal origin of the NC. It could be a star-formation region (of which there are many inside NGC 1427A) that is being pulled out by the Fornax Cluster tidal forces, leaving behind a stream of stars. As shown in Figure 4.15, star formation flares up in our simulated dwarf galaxies around pericenter passage and leads to the appearance of scattered bright, blue clumps of active star formation. These clumps orbit along with the general rotation of their host galaxy. The spatial location and the time of appearance of these clumps are erratic and differ between galaxies and between orbits. For instance, a star-forming clump is first visible to the top-right of the galaxy in the snapshots 108 Myr before pericenter passage (second column in Figure 4.15; it rotates clockwise, and disappears again after the 137 Myr past pericenter passage snapshot. Likewise, other clumps with similar lifespans pop in and out of existence around pericenter passage.

Based on these simulations and the available observational data, we suggest that the NC is precisely such a star-forming clump. This interpretation is consistent with its very young age and blue colour, its presence around the time that NGC 1427A is expected to be near pericenter passage (this is required to explain all other characteristics of NGC 1427A), and its kinematics being in line with the galaxy's global velocity field.

4.5 Conclusions

We carried out a set of simulations of gas-rich late-type dwarf galaxies in a Fornax-like cluster environment. We isolated snapshots with morphological properties similar to the peculiar galaxy NGC 1427A. The properties have been chosen to be representing the impact of the environment on the dwarf. We found that the main effects generating peculiar morphology are indeed the combination of ram pressure and tidal interaction close to the cluster center and galaxy rotation. We saw that the most likely scenario which recreates NGC 1427A tails morphology is assuming

the galaxy to be on a very radial orbit with its tail almost aligned with the line of sight, pointing towards the observer. This naturally leads to a gas kinematic configuration consistent with HI observations: in the westward part, gas attached to the stellar body of the galaxy is receding whereas the eastward part is stripped and dragged towards the observed by the intra-cluster medium (or ICM), therefore having a smaller recessional velocity, see Figures 4.3c and 4.2b.

From the analysis of the morphology of the simulated snapshots motivated by environmental effects, we found an excess of snapshots revealing similar NGC 1427A structure around 150 Myr before pericenter passage. It should be highlighted that this result comes from a suite of simulation which has not been tailored from the beginning to reproduce NGC 1427A. Nonetheless, interestingly, falsifiable predictions on the location and orbital phase of the galaxy can be made.

We can sum up the main results in the following points:

- Perpendicular gaseous and stellar tails are explainable given that they are subject to different environmental effects.
- Tails geometry is crucial to unravelling the direction of motion of the galaxy and its orbit.
- From our suite of simulation it is evident how around ~150 Myr before first pericenter passage, a morphological tail structure like the one of NGC 1427A emerges in galaxy falling into a Fornax-like cluster.
- In simulations, around pericenter, clumps of newly formed stars can form. This is coherent with a formation scenario of NGC 1427A's Northern Clump as a star formation region pulled out by tidal forces.
- Following our modelling it is possible to estimate the most likely position of a NGC 1427A-like galaxy to be around 200 kpc in front of the cluster center. Also, the most likely flight direction (represented by the angle γ in the paper) is around 50 deg.

Data availability

The data underlying this article and the algorithms used are available at this GitHub repository: <https://github.com/elehcim/ngc1427apaper>.

A publicly available python package to analyze the simulations in this dataset can be found at this GitHub repository: <https://github.com/elehcim/simulation>.

Based on: *Probabilistic modelling of general noisy multi-manifold data sets*, Canducci M., Tiňo P., Mastropietro M. Canducci et al. (2022). Part of this work has been carried out during the planned SUNDIAL secondment at the Computer Science Department of the University of Birmingham.

Low-dimensional manifolds

5

Abstract

The intrinsic nature of noisy and complex data sets is often concealed in low-dimensional structures embedded in a higher dimensional space. In real-world applications, the data can contain several low-dimensional structures of different dimensionalities. We propose a framework for dimensionality estimation and reconstruction of multiple noisy manifolds embedded in a noisy environment. The framework is then applied to a complex data set containing simulated gas volume particles from a particle simulation of a dwarf galaxy interacting with its host galaxy cluster. Detailed analysis of the recovered 1-D and 2-D manifolds can help us to understand the distribution of various physical quantities in such complex systems. The technique allows to isolate the evolution of quantities around tails of a simulated jellyfish galaxy, so that of star formation regions and the mixing of galaxy gas and cluster gas can be studied.

5.1 Introduction

Dimensionality reduction and Density Estimation of raw data, are commonly used tools to extract information from complex and noisy data sets. Due to dependencies among measured attributes of real world data, the data is often distributed along low-dimensional structures in a higher dimensional measurement space. This realisation has driven the development of a variety of Manifold Learning algorithms. Principal Component Analysis (PCA, Pearson, 1901) is a well understood and widely used linear dimensionality reduction scheme. However, by design, PCA cannot appropriately capture non-linear low-dimensional structures.

Generative Topographic Mapping (GTM, Bishop et al., 1998) was proposed as a probabilistic formulation of the Self-Organizing Map (Kohonen, 1982). Its main advantage is that instead of treating noisy manifold

as a core low-dimensional manifold to be discovered, plus some “noise” around it that somehow needs to be dealt with, it formulates a consistent manifold-aligned density model in the form of a constrained mixture of Gaussians. The location parameters (means) of the Gaussian components are constrained to lie on a smooth manifold – most commonly a smooth image in the data space of a two-dimensional interval (latent space).

In Canducci et al. (2022) we propose a framework for automated dimensionality estimation and reconstruction of multiple noisy manifolds embedded in a noisy environment called *Abstract Generative Topographic Mapping* (AGTM). Since our latent space is a discrete structure (abstract graph representing a skeleton of a given manifold), we formulate local noise models through kernel based estimates of the local covariance matrix of the data, with trainable scale parameter to allow for optimized overlapping of the neighbouring Gaussian components. The work is inspired by Wang et al. (2008), but extends and generalizes it, so that densities aligned along arbitrary manifolds (even non-orientable ones such as Möbius strip) can be captured,

The detailed aspects of AGTM will not be described in this thesis, because its treatment is not suitable for this context. However, after the identification of the low-dimensional manifold as in Canducci et al. (2022), instead of the probabilistic one, we’ll use the SPH approach to estimate densities to compute physical quantities along the manifolds.

This work is the product of the collaboration in the SUNDIAL network between the Birmingham and the Gent node. It should be clear that the original mathematical treatment of dimensionality estimation and AGTM have been authored by the Birmingham node. My direct contributions to the work are the idea of analysis of jellyfish tails, the development of independent code to test the manifold analysis, the scientific questions driving the application of the method, supervision on the implementation, the proposal of physical quantities to be analyzed from the simulation and their physical interpretation.

The methodology is applied in section 5.3 to a numerical simulation of a dwarf galaxy falling into the gaseous halo of a Fornax-like cluster, a snapshot of the simulation ID 69 described in Chapter 2. The point cloud generated by the simulation presents non linear, noisy, low dimensional structures, providing for an ideal test bed for our methodology. We extract and model two of the most significant manifolds, suggesting a possible scenario for formation of new stars in such a disrupted dwarf galaxy.

5.2 Methodology

We refer to Canducci et al. (2022) for the thorough mathematical presentation of the technique. Here we sketch the main ideas and we set up the scene in order for the reader to understand the overall methods used. In the following we give a brief outline of our methodology to robustly detect the manifolds.

5.2.1 Diffusion filtering

Consider a point cloud

$$\mathcal{Q} = \{\mathbf{t}_1, \mathbf{t}_2, \dots, \mathbf{t}_L\}, \quad \mathbf{t}_i \in \mathbb{R}^d$$

containing points sampled from an unknown number of noisy lower-dimensional manifolds embedded in a noisy environment (e.g. points generated from a broad d -dimensional distribution). We first apply a physics-based diffusion method, Structure-Aware Filtering Technique (SAF, Wu et al., 2018), that collapses points in close vicinity of dense structures onto them, resulting in a diffused data set:

$$\tilde{\mathcal{Q}} = \{\tilde{\mathbf{t}}_1, \tilde{\mathbf{t}}_2, \dots, \tilde{\mathbf{t}}_L\}, \quad \tilde{\mathbf{t}}_i \in \mathbb{R}^d.$$

The SAF method moves points towards high density regions, enabling points in the vicinity of a noisy manifold to migrate towards its “spine” or “mean surface”.

Assuming that the data structures to be modeled are more densely sampled than the noisy environment we first filter the data sets \mathcal{Q} and $\tilde{\mathcal{Q}}$ by removing point couples $(\mathbf{t}_i, \mathbf{t}_i)$ that have sparse neighbourhood in both \mathcal{Q} and $\tilde{\mathcal{Q}}$. In particular, around each \mathbf{t}_i and $\tilde{\mathbf{t}}_i$ we construct a hyperball $\mathcal{B}(\mathbf{t}_i; r)$ and $\mathcal{B}(\tilde{\mathbf{t}}_i; r)$ in \mathbb{R}^d of radius $r > 0$. In case a point \mathbf{t}_i lies further apart from a manifold, both hyperballs will be sparsely populated. Hence, if both $\mathcal{B}(\mathbf{t}_i; r)$ and $\mathcal{B}(\tilde{\mathbf{t}}_i; r)$ contain less points than a pre-specified threshold $\tau > 0$ the points \mathbf{t}_i and $\tilde{\mathbf{t}}_i$ are removed from their corresponding data sets.

Following this, the first task in capturing the multi-manifold structure in $\tilde{\mathcal{Q}}$ is to estimate local dimensionality of the cloud point around each $\tilde{\mathbf{t}}_i$ in the form of a *dimensionality index* δ_i (section 5.2.2). Using the dimensionality indices, we partition the data into subsets $\tilde{\mathcal{Q}}_j$ according to the local dimensionalities $j = 1, 2, \dots, d$.

Since $\mathcal{Q}_j, \tilde{\mathcal{Q}}_j$ can contain several distinct sampled manifolds of dimensionality j , we use a dedicated *manifold crawling* procedure operating on $\tilde{\mathcal{Q}}$

to separate the individual manifolds (section 5.2.3). Moreover, the crawling also produces for each manifold a graph structure embedded in \mathbb{R}^d representing a piece-wise linear “skeleton” approximation of the spine of the noisy manifold.

5.2.2 Dimensionality estimation

Around each $\tilde{t}_i \in \tilde{\mathcal{Q}}$ we perform local Principal Component Analysis (PCA) using points from $\mathcal{B}(\tilde{t}_i; r) \cap \tilde{\mathcal{Q}}$, obtaining eigenspectrum

$$\lambda_{i,1} \geq \lambda_{i,2} \geq \dots \geq \lambda_{i,d}.$$

We suggest a general method for computing dimensionality index of points distributed in spaces of arbitrary finite dimension d , based on renormalized eigenvalues,

$$\tilde{\lambda}_{i,j} = \frac{\lambda_{i,j}}{\sum_{k=1}^d \lambda_{i,k}},$$

viewed as “likelihoods” of different dimensionalities j of the cloud of points around \tilde{t}_i .

Simplex Note that $\tilde{\Lambda}_i = (\tilde{\lambda}_{i,1}, \tilde{\lambda}_{i,2}, \dots, \tilde{\lambda}_{i,d})$ lies in the $(d-1)$ -dimensional simplex \mathcal{S}_0 with vertices:

$$\begin{aligned}\mathbf{s}_1 &= (1, 0, 0, \dots, 0), \\ \mathbf{s}_2 &= (1/2, 1/2, 0, \dots, 0), \\ \mathbf{s}_3 &= (1/3, 1/3, 1/3, \dots, 0), \dots \\ \mathbf{s}_d &= (1/d, 1/d, 1/d, \dots, 1/d).\end{aligned}$$

It is useful to see \mathcal{S}_0 as a subset of the the simplex of multinomial distributions, so that for any point of the simplex, $\tilde{\Lambda}_k \in \mathcal{S}_0$, we will compute its distance from the vertex \mathbf{s}_j using the Fisher distance (Lebanon, 2005):

$$d_J(\tilde{\Lambda}_k, \mathbf{s}_j) = 2 \arccos \left(\sum_{i=1}^d \sqrt{(\tilde{\lambda}_{ki} s_{ji})} \right). \quad (5.1)$$

We therefore assign to each point \tilde{t}_i of the dataset a dimensionality index δ_i as the index of the closer (assuming the d_J distance metric) vertex of the simplex:

$$\delta_i = \arg \min_j d_J(\tilde{\Lambda}_i, \mathbf{s}_j). \quad (5.2)$$

In Canducci et al. (2022) also a “soft” and spatially smoothed version of the dimensionality index is proposed.

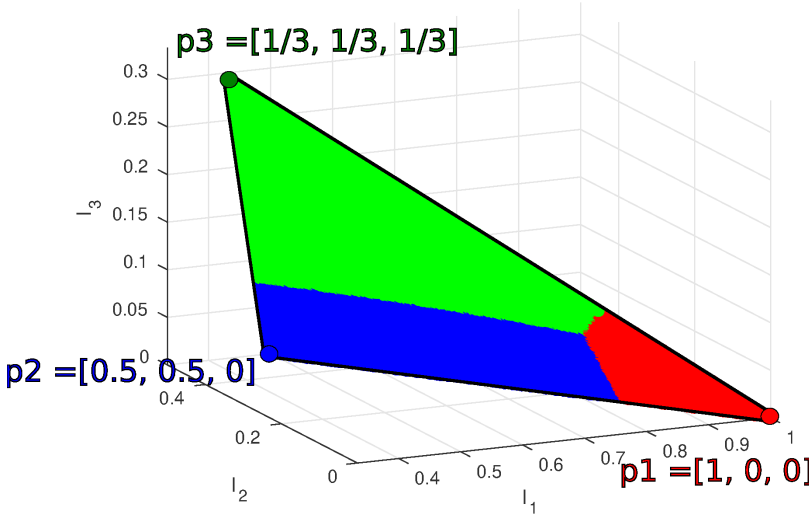


Figure 5.1: Simplex S_0 in three dimensions. p_1 , p_2 and p_3 are the analogous of the s_1 , s_2 , s_3 vertexes. The three parts of the simplex are coloured depending on the minimum distance vertex using the Fisher metric (5.1).

5.2.3 Crawling

After having identified the subsets of points belonging to manifolds of different dimensionalities, for each dimension we would like to isolate the (possibly multiple) embedded manifolds they can contain. The goal is to create a latent space containing all the information about a detected manifold \mathcal{M} embedded in a higher dimensional data space.

The mapping $f : \mathcal{V} \rightarrow \mathbb{R}^d$ from the latent space to the data space is, following Bishop et al. (1998), a nonlinear model, linear in parameters. The latent space grid structure can be represented by an abstract undirected graph $\mathcal{G} = (\mathcal{V}, \mathcal{E})$, where each grid point corresponds to a vertex $v_i \in \mathcal{V}$ and edges $e_{ij} \in \mathcal{E}$ are connecting vertices corresponding to neighbouring grid points. In particular, the image of a vertex $v \in \mathcal{V}$ is obtained as $\bar{v}_i = f(v)$ operating on the latent space \mathcal{G} (see section 3.1 of Canducci et al., 2022, for details). The goal of the crawling is to create a manifold skeleton formed by the embedded graph $\bar{\mathcal{G}} = (\bar{\mathcal{V}}, \bar{\mathcal{E}})$.

Manifold crawling Briefly, starting from a randomly selected data point \tilde{t}_0 , a local PCA in $\mathcal{B}(\tilde{t}_0; r)$ is performed and depending on the dimensionality δ_j of \tilde{t}_0 , the first j largest eigenvectors u_j are selected to define the tangent space to the manifold \mathcal{M} . For each local eigenvector u_j , a step of length ηr is performed in its directions $(\pm u_j)$. A new vertex \bar{v} of the graph $\bar{\mathcal{V}}$ is then selected as the closest data point to $z_j^\pm = \tilde{t}_0 \pm \eta r u_j$. The graph $\bar{\mathcal{V}}$ is gradually constructed in this way.

At the end of this step, we obtain: a latent space graph \mathcal{G} , a set of points \tilde{t}_i belonging to the manifold, and an embedding $f : \mathcal{V} \rightarrow \mathbb{R}^d$. This will enable us to naturally represent density models of noisy manifolds of much more intricate structure than that of a smoothly embedded low dimensional interval.

The latent space graph is interesting because it contains information about the topology of the manifold: the local curvature, the local elongation. From the derivative along the edges e_{ij} of the mapping f it is possible to compute the local curvature and elongation (see Figure 5.4).

5.3 Experiments on a simulated jellyfish galaxy

We will demonstrate our methodology on the analysis of formation of a peculiar astronomical object, a simulated “jellyfish galaxy”. The term refers to an observed galaxy showing signs of gas stripping (Poggianti et al., 2017), whose signatures are a dense “head” of mainly gas and stars and an elongated gaseous, star-forming tail. These galaxies are usually observed when falling into large clusters of other galaxies, where the hot ionized gas filling the cluster is able to strip away “tentacles” of relative cold gas from the galactic body.

The technique described above can be a valuable tool to investigate the behaviour of physical quantities in the head and in the gaseous tail. We will focus our study on identifying star formation regions in the head and in the tail of the galaxy for two main reasons:

- i) presence of new stars born in the head is an important indicator of how much the galactic gas is affected by the stripping pressure;
- ii) since stars are created from dense and cold regions of gas, the presence (or lack thereof) of stars formed in the gaseous tail carries information about how much the galaxy gas is mixed with the hot gas in the surrounding environment.

To quantify the star formation we will measure the intensity of the [C II] emission line. Recent observations with the Herschel Space Observatory

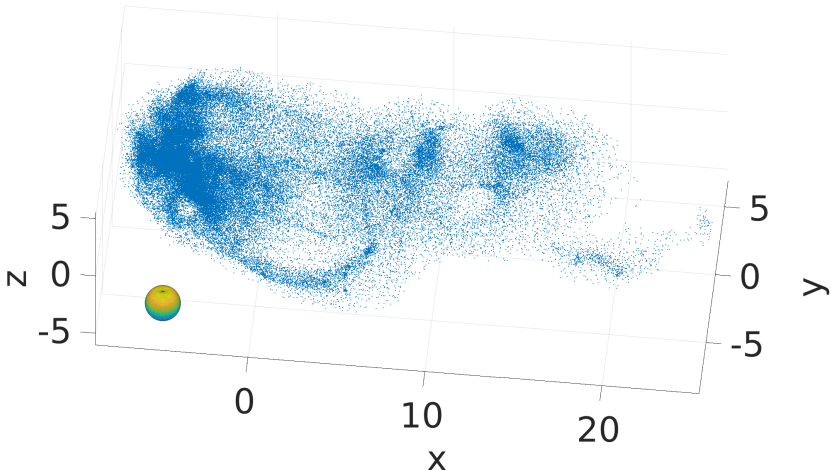


Figure 5.2: Gas particles of the simulated dwarf galaxy falling into the halo of the Fornax Galaxy Cluster.

showed a tight correlation between the intensity of [C II] and other well known tracers of Star Formation Rate (SFR) (De Looze et al., 2011; Herrera-Camus et al., 2015).

The study can provide useful insights on the formation scenario of galaxies infalling in a cluster (Ebeling et al., 2014). As an example, dwarf galaxy NGC 1427A in the Fornax cluster, described in detail in Chapter 4, provides an interesting case of still unclear formation scenario and a generally accepted common interpretation is still lacking (Lee-Waddell et al., 2018; Mora et al., 2015).

Starting from the suite of simulations of dwarf galaxies evolving in a Fornax-like cluster environment (explained in detail in Chapter 2), we chose a single simulated snapshot representing an irregular, gas rich galaxy, exposing an elongated star forming gaseous tail during intense ram pressure stripping (we used a snapshot at $\tau = 0.10$, $t = 9.17$ Gyr of simulation ID 69p100, snapshot 100). As described in Section 2.3, the computation model in SPH simulations is based on a particle formulation of hydrodynamics where each particle samples physical properties of a volume of radius r_N - radius of the sphere containing N neighbouring particles. A continuous distribution of the physical variables over the full domain is then obtained by spatial smoothing with Gaussian kernels centered on each particle (Gingold & Monaghan, 1977a). Associated with each gas particle are

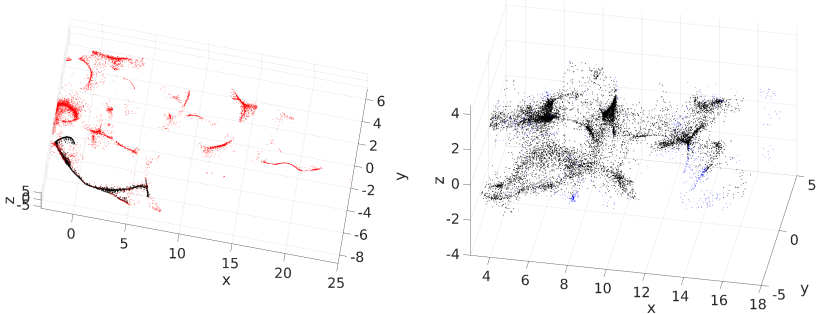


Figure 5.3: 1-D (left) and 2-D (right) distributions of the diffused particles in the tail of the jellyfish structure. Highlighted in black are the points belonging to two distinct 1-D and 2-D structures discussed in section 5.4.

values of physical quantities such as density, temperature, pressure etc.

To do this we post process the simulation obtaining for each particle the intensity of the [C II] emission line. This is the “forbidden” line emitted by a carbon atom which has been ionized - having 5 out of 6 electrons. The outermost electron of the ionized atom gets excited on a higher energy level by radiation. The excited electron, under extremely low density environment conditions, is able to re-emit radiation at a specific wavelength ($158 \mu\text{m}$) while jumping to a lower energy level. These types of emission lines are called “forbidden” due to their impossibility to be seen in normal terrestrial environments.

An estimate of [C II] emission in this kind of simulations is obtained by using evolved quantities of the gas (metallicity, density and temperature) as inputs of chemical evolution models of the radiating gas, taking into account its ionization equilibrium and ion level occupation model (Maio et al., 2007; De Rijcke et al., 2013).

The resulting gas particle data set is presented in Figure 5.2. Several low dimensional structures are clearly visible, for example the long 1-D manifold departing from the head and elongating along the x -axis of the simulation box. Visually inspecting the data set, we chose a radius $r = 1 \text{ kpc}$ as the characteristic scale parameter for the manifolds (shown as the small sphere in Figure 5.2). The chosen radius is in agreement with the spatial resolution of recent observations. The parameter r is fixed for preprocessing through diffusion and filtering (section 5.2.1), local dimensionality estimation (section 5.2.2) and manifold crawling (section 5.2.3). We highlight that this parameter is not used to smooth, and is not related to the

smoothing lengths coming from SPH.

As mentioned earlier, the main body of the data set can be visually divided into head and tail parts. However, from the topological standpoint there is no justification for clear segregation into 1-D manifolds in the tail and 2-D manifolds in the head, as one may expect naively. Dimensionality index estimation clearly identified 1-D structures in the tail, such as elongated streams of particles starting from the head. However, points in the head were also predominantly identified as 1-D, due to its complicated, intertwined filamentary structure. On the other hand, distribution of 2-D points was more localized in the main body of the tail.

5.4 A multi-manifold analysis of a dwarf jellyfish galaxy

Having obtained the multi-manifold probabilistic profile of the gas particles in the tail of the jellyfish galaxy, it is possible to perform various kinds of detailed analysis of how physical properties vary along the manifolds. Here we concentrate on the curvature (Figure 5.4), computed through the embedding (details in Canducci et al., 2022, section 3.2.1) and on the star formation potential. The latter is analysed by studying the behaviour of emission line [C II] over the 1-D and 2-D structures in the jellyfish tail shown as black dots in Figure 5.3 (left) and (right), respectively - the gaseous stream of gas particles departing from the head and reaching halfway through the tail and the predominant 2-D structure in the tail.

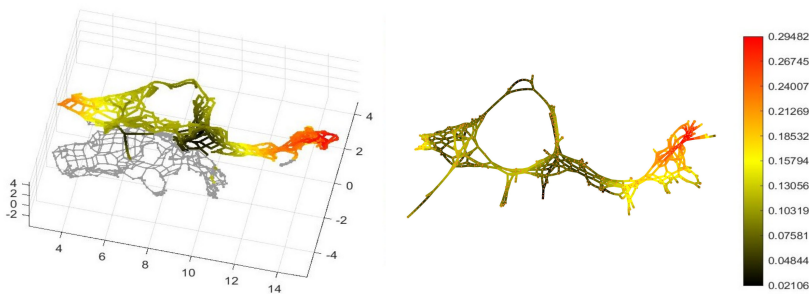


Figure 5.4: Embedded graph (left panel) and planar representation (right panel) of a 2-dimensional manifold extracted from the jellyfish data set. The local curvature for each vertex is shown in color.

Figure 5.4, left panel shows two regions of high curvature, for the 2-D manifold presented in Figure 5.3, right panel. The far right region of in-

tense curvature, is located towards the end of the tail, where it's expected a turbulent chaotic behaviour of the gas due to the motion of the galaxy through the halo of the galaxy cluster. However, the spherical region on the left side of the manifold, presenting a coherent curvature throughout its elongation (top right corner of Figure 5.4) suggests, as a possible cause of formation, an isotropic expansion, typical of Supernova remnants.

We performed the SAF filtering, dimensionality analysis and manifold crawling, and for the two identified manifolds we show in Figure 5.5 the embedded vertices \bar{v}_j of the graph $\bar{\mathcal{G}}$ for both the stream and the 2-D manifold. The vertices are color coded with the SPH interpolation of the [C II] intensity field. That is the average of the [C II] intensity of the particles at the nodes' positions \bar{v}_j weighted with the SPH smoothing kernel W defined in equation (2.16) in Section 2.3.1:

$$\langle \mathcal{I}_j^{[\text{C II}]} \rangle = \frac{\sum_{i=1}^N \mathcal{I}_i^{[\text{C II}]} W(\|\mathbf{t}_i - \bar{v}_j\|, h_i) m_i / \rho_i}{\sum_{i=1}^N W(\mathbf{t}_i - \bar{v}_j, h_i) m_i / \rho_i} \quad (5.3)$$

with N the total number of particles in the dataset.

It is worth noting that this method (the classical SPH) is different from what is employed in Canducci et al. (2022), where a probabilistic approach with a mixture of locally manifold-aligned trivariate gaussians is used to retrieve the intensity of the nodes. Their intensity is modulated by the weighted mean of [C II] values $\mathcal{I}_i^{[\text{C II}]}$ of particles \mathbf{t}_i in the manifold, where the weights are the posterior probabilities of the node v_j , given particles \mathbf{t}_i . The fact that the gaussians themselves are oriented on the manifolds may highlight areas of the dataset where the intensity is more manifold aligned, like in the edges of the hole found in the 2-D manifold. This is indeed at the basis of manifold learning: it is assumed that data points are the expression of an underlying manifold aligned distribution.

In the 1-D case, the manifold is located at the outskirts of the Jellyfish (Figure 5.3, left panel), meaning that it is more exposed to the surrounding gas of the galaxy cluster. This implies that the manifold is subject to a higher ram pressure than the tail, leading to a higher density and lower temperature of the gas - necessary conditions for the formation of new stars. These conditions are reflected in an increase of the [C II] emission line over the end section of the manifold, as shown in Figure 5.5a at $3 < y < 7$, where there are clumps of high [C II] emission, thus informing us of an enhanced star formation rate, compared to the rest of the manifold.

The 2-D structure in Figure 5.5b shows an overall constant [C II] intensity whereas the region at $6 < y < 10$ presents clumps of higher values. The shape of this region is particularly interesting. It is, in fact, a hole with an

almost spherical section. This structure detected with Manifold Crawling, with clumps of [C II] emission at its boundary, is the remnant of a supernova explosion. Due to their high mass, young stars burn efficiently and relatively fast all their gas reservoir, terminating their life as supernovae and injecting energy and debris in the surroundings. This process is modeled in the simulation via an injection of 10^{51} erg of energy for a short amount of time and a transfer of metallic elements (in the case of our simulations, the model tracks iron and magnesium, De Rijcke et al., 2013) to the neighbouring gas particles. The metal-enriched gas particles (like in the surrounding of a supernova explosion) are then able to cool down more efficiently and show strong [C II] emission line.

Our methodology provides a strong tool for extracting such an information from the morphology of gas particles and can be used to effectively calibrate feedback models in simulations.

Such a detailed analysis of low dimensional structures (remnants of galaxy interactions) is not currently possible with tools routinely used to calibrate and analyse astrophysical simulations of galaxy evolution. The technique presented in this paper can be used as a semi-automatic exploratory tool by the domain experts, where the focus and characteristic scale of the structures to be mined can be varied continuously with analysis of their physical properties of interest (after necessary computations) performed and studied on the fly. As an example we show an application in the next section.

5.5 Evolution of quantities along the jellyfish tails

We now describe a methodology that, taking full advantage of the manifold extraction technique and SPH density formulation, simultaneously recovers the behaviour of simulated properties along the manifold's elongation and its thickness within the simulated volume. In this section we consider only the 1-D case. It's possible to carry out a similar analysis for the 2-D case, but the result is not of easy interpretation and not appropriate in this context.

We start from the centers found by the crawling which are lying on the identified manifold. These center are points $\tilde{\mathbf{t}}_\ell \in \tilde{\mathcal{Q}}$ belonging to the diffused dataset. From each pair of adjacent centers we can compute the tangent bundle on the 1-D manifold:

$$\hat{\mathbf{v}}_\ell = \frac{\tilde{\mathbf{t}}_{\ell+1} - \tilde{\mathbf{t}}_\ell}{\|\tilde{\mathbf{t}}_{\ell+1} - \tilde{\mathbf{t}}_\ell\|}, \quad (5.4)$$

The norm $d_\ell = \|\tilde{\mathbf{t}}_{\ell+1} - \tilde{\mathbf{t}}_\ell\|$ is also the distance between the two adjacent centers.

5.5.1 Computing a point cloud around each manifold segment

Around each segment of length d_ℓ we want to build a cylinder or randomly distributed points which will be used to compute tangential and radial average along the manifold of the quantity. To do so, let us now consider a point cloud \mathcal{C} containing randomly distributed points $\mathbf{p} \in \mathcal{C}$, uniformly sampling a cylindrical volume of radius 1, aligned along the z -axis and centered at the origin \mathcal{O} . As a first step we partition the point cloud into concentric cylindrical shells $\mathcal{S}^i : \bigcup_i \mathcal{S}^i \equiv \mathcal{C}$. For every point $\mathbf{p} \in \mathcal{C}$ we compute its distance to the cylinder z -axis, versor \hat{k} . We can now group points in \mathcal{C} so that:

$$\mathcal{S}^i = \left\{ \mathbf{p}_j : r_{i-1} \leq \|\mathbf{p}_j - \hat{k}\| < r_i \right\}, \forall \mathbf{p}_j \in \mathcal{C}. \quad (5.5)$$

We radially partition into concentric cylindrical shells and for each point we compute its distance to the projected origin, as show in Figure 5.6.

It is always possible to scale, translate and rotate the point cloud so that the cylindrical axis is oriented as the vector \mathbf{v}_ℓ , the origin over-posed to center $\tilde{\mathbf{t}}_\ell$ and the axis length equal to d_ℓ . The scaling operator is the diagonal matrix $S = \text{diag}(1, 1, d_\ell)$. To rotate the cylinder we compute the quaternion \mathbf{q} which rotates the z -axis versor \hat{k} into $\hat{\mathbf{v}}_\ell$. From equation (2.38)

$$\mathbf{q} = \frac{\mathbf{q}^*}{\|\mathbf{q}^*\|} \quad \text{with } \mathbf{q}^* = (\hat{\mathbf{v}}_\ell \cdot \hat{k} + 1, \hat{\mathbf{v}}_\ell \times \hat{k}). \quad (5.6)$$

We can then shift the scaled and rotated point cloud so that its origin is on center $\tilde{\mathbf{t}}_\ell$. Any point $\mathbf{p} \in \mathcal{C}$ is then mapped to $\mathbf{p}' \in \mathcal{C}'$ under the combined operator as:

$$\mathbf{p}' = \bar{\mathbf{q}}(S \mathbf{p}) \mathbf{q} + \tilde{\mathbf{t}}_\ell \quad (5.7)$$

Having obtained a point cloud \mathcal{C}' uniformly sampling a thick cylindrical volume with axis tangential to the tangent subspace of manifold \mathcal{M} on point $\tilde{\mathbf{t}}_\ell$, we can now compute the SPH weighted mean of any quantity contained in the data set, over the volume sampled by \mathcal{C}' .

Consider now a point $\mathbf{p}' \in \mathcal{C}'$, we need to compute the weighted mean, under the SPH formalism, of a quantity V summing through all the particles $\mathbf{t}_j \in \mathcal{Q}$. As usual we use the the M-4 spline kernel W defined in equation (2.16) in Section 2.3.1. the exact weighted mean of quantity V at

point \mathbf{p}' is:

$$\langle V(\mathbf{p}') \rangle = \frac{\sum_{\mathbf{t}_j \in \mathbf{Q}} \frac{m_j}{\rho_j} V(\mathbf{t}_j) W(q_j, h_j)}{\sum_{j=1}^{|\mathbf{Q}|} \frac{m_j}{\rho_j} W(q_j, h_j)} \quad (5.8)$$

where $q_j = \|\mathbf{p}' - \mathbf{t}_j\|/h_j$. We highlight that the summation is carried out on the whole dataset \mathbf{t}_i . Given the finite support of the kernel W , practically only particles close to the manifold will contribute to $\langle V \rangle$, see Figure 5.7. The terms in the denominator are generally considered to be approximating unity when the particles in a data set are distributed uniformly; however, this is not often the case in practice. As mentioned in Section 2.3, each particle at position \mathbf{t}_j of an SPH data set samples a spherical volume of radius h_j . However, all particles are evolved following the equations of motion defined by the Lagrangian formulation of fluids. Thus, the distribution of particles in a data set at a given evolutionary stage is far from uniform, making the initial assumption incorrect. The role of the normalization term in the denominator of equation 5.8 is to eliminate the dependence of the interpolation to the particle's distribution. As such, it can not be disregarded when computing the interpolation of quantity V on any point in the volume.

After computing $\langle V(\mathbf{p}') \rangle$ for every $\mathbf{p}' \in \mathcal{C}'$ we can now evaluate the mean value of V over the concentric cylindrical shells built in the original manifold.

$$\langle V(r_{i-1}, r_i) \rangle = \frac{1}{|\mathcal{S}'^i|} \sum_{\mathbf{p}'_j \in \mathcal{S}'^i} \langle V(\mathbf{p}'_j) \rangle, \quad (5.9)$$

obtaining the mean of V over the cylindrical shell between (r_{i-1}, r_i) .

We can iterate the whole process for every center the manifold, obtaining for each linear segment the distribution of V in concentric cylindrical shells.

5.5.2 How do quantities vary along the tail manifold?

By considering both longitudinal profiles (defined along the tangent bundle of the manifold \mathcal{M} , see Figure 5.7) and radial profiles (obtained by the linear operator defined in equation (5.7) on point cloud \mathcal{C}), we obtain the plots shown in Figure 5.8. They represent a 1-D manifold detected with the crawling, the same as in Figure 5.7. In each panel, the vertical axis of the plot contains the radius of the cylindrical shells r and the horizontal axis the approximated geodesic distance (computed by summation of

the lengths of the individual linear segments) from the head of the manifold. The longitudinal axis in the figure goes from the jellyfish head (corresponding to 0 kpc) to the tail.

In Figure 5.8 we show the evolution of volumetric density ρ , neutral fraction, iron abundance [Fe/H] and temperature T . We notice how the central part of the manifold in the radial direction is denser as expected. The density is high enough to self-shield from the UV background keeping the gas neutral as shown in the second panel. This suggests that the tail would be visible when viewed in the 21 cm radio frequency. Longitudinally, towards the head (left-most part of the plot), density and neutral fraction are larger with respect to the end of the tail. This is natural given the amount of gas concentrated in the jellyfish head. The iron abundance distribution is instead characterized with locations of high metallicity, roughly corresponding to high density regions. They corresponds to regions of recent star formation where supernova feedback has taken place. This is in line with the hypothesis of galactic tails beaded with knots of star formation in the tail. Moreover, there is no strong gradient of [Fe/H] along the tail, suggesting a poor mixing of gas between the galactic tail and the cluster gas. This is confirmed by the almost uniform distribution of temperature in the tail, where the only high temperature region is a possible infiltration of cluster gas in the tail.

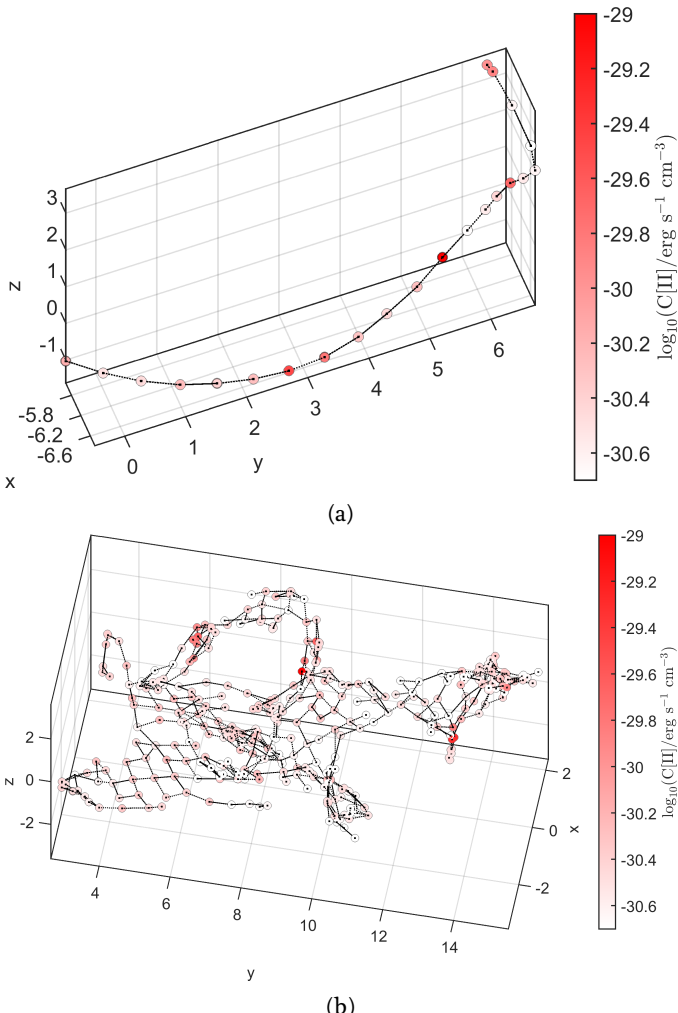


Figure 5.5: 1-D (a) and 2-D (b) manifolds extracted from the data set in Figure 5.2. The graphs' vertexes are colored based on the value of the SPH smoothed [C II] emission computed at the positions of the nodes.

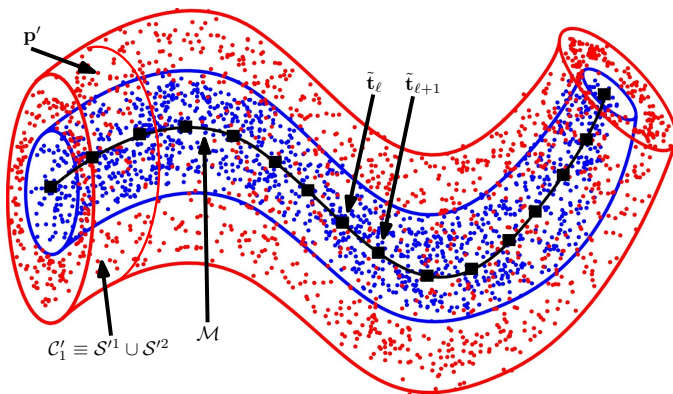


Figure 5.6: Schematic of the partition of the space around the manifold in two concentric cylindrical shells (S'^1, S'^2) of uniformly distributed sample points p'_i constituted by segmented cylinders (only one is shown on the left) build from one center to another of the manifold \mathcal{M} .

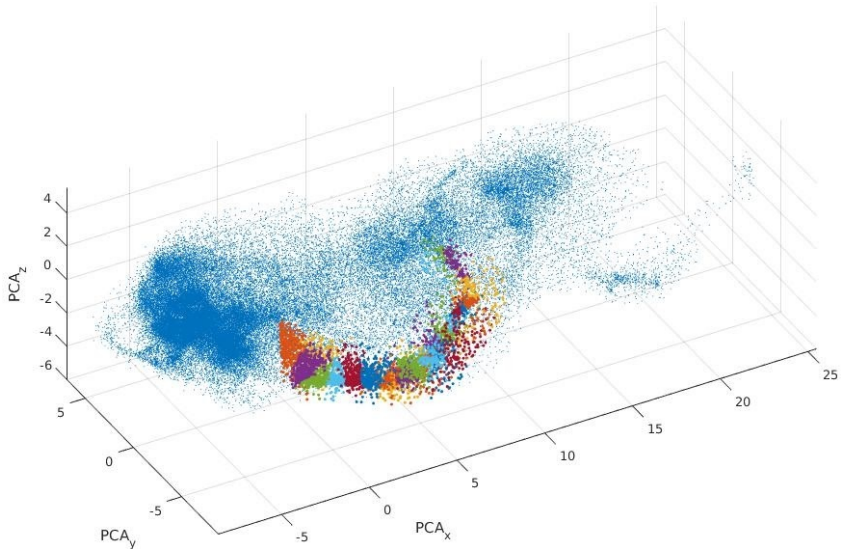


Figure 5.7: Points t_j around the identified manifold, coloured differently depending on the longitudinal partition they belong to.

5.5 Evolution of quantities along the jellyfish tails

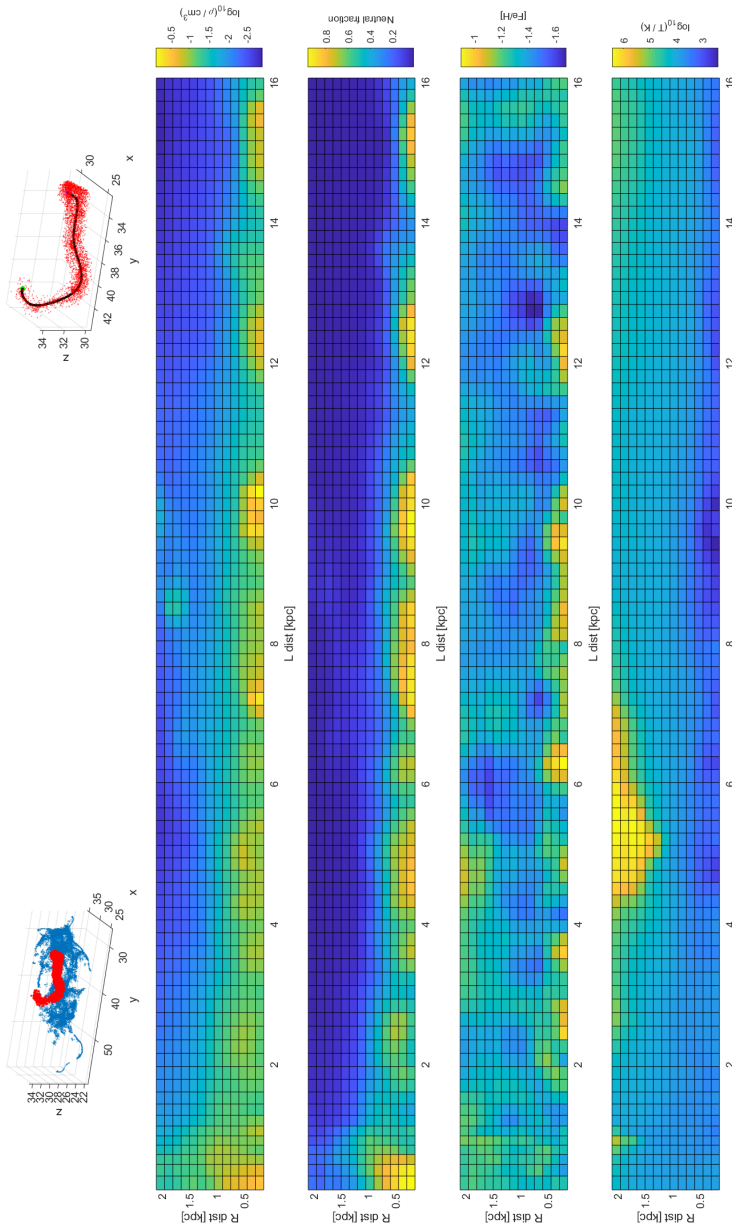


Figure 5.8: Longitudinal and radial profiles of different quantities for a long manifold constituting a tentacle of the tail of the jellyfish. In the top left corner, the position of the manifold in the diffused dataset is shown in red. In the top right corner a detailed view of the non diffused gaseous particle belonging to the manifold.

Conclusions and future work

6

We sum up here the main conclusions of the research carried out in this PhD effort, and we briefly give an overview of the ongoing research projects.

6.1 Conclusions

Relative to the scientific questions stated in Section 1.2, we can outline the following conclusions:

- I implemented the Moving Box technique in the existing N-body/SPH code used to simulate dwarf galaxies in isolation. We applied for the first time this technique (see Section 2.5) to a galaxy-cluster setup, being able to simulate gas-rich realistic late-type galaxies falling into a Fornax-like cluster (Chapter 2);
- analyzing the results of the simulations I found that the jellyfish phenomenon is a relatively short transitory phase of the galaxy along its orbit, and its likely a precursor of the transformation of a dwarf galaxy into an UDG (Chapter 3).
I created a catalogue of results of simulations that can be found online: <http://moria-fornax.herokuapp.com/>;
- I was able to propose an estimate of the the most likely position of an NGC 1427A-like galaxy in front of the cluster center, and its most likely flight direction (Chapter 4). Based on the idea that gaseous and stellar tails are impacted differently by environmental processes, using the simulation setup developed I was able to reproduce the peculiar morphology of NGC 1427A;
- I contributed to the development of novel low-dimensional manifold extraction technique from cloud points and applied the method to the analysis of the tails of a simulated jellyfish galaxy (Chapter 5). My direct contributions to the work are the idea of analysis of jellyfish tails, the development of independent code to test the manifold analysis, the scientific questions driving the application of the

6 Conclusions and future work

method, supervision on the implementation, the proposal of physical quantities to be analyzed from the simulation and their physical interpretation.

6.2 Ongoing research efforts

6.2.1 MUSE mock cube

Integral-Field Units (IFU) are powerful instruments which couple the discovery potential of imaging devices to the measuring capabilities of spectrographs. MUSE (Multi Unit Spectroscopic Explorer is an integral-field spectrograph operating in the visible wavelength range, currently mounted on the Very Large Telescope (VLT) of the European Southern Observatory (ESO) (Bacon et al., 2010; MUSE Consortium, 2021). As a way to compare simulations with observations and check the tools currently employed in the analysis of IFUs data cubes, we created a tool to produce MUSE-like data cubes from the MoRIA suite of simulations. Code is freely available from <https://github.com/elehcim/simifucube>. This work has been done in collaboration with the Heidelberg node of the SUNDIAL network.

We start by taking the star particles of a simulated snapshot. Similarly to Ibarra-Medel et al. (2019), depending on the age t_i and metallicity $[\text{Fe}/\text{H}]_i$ of each star particle i , we assign to it a spectrum from the EMILES library (Vazdekis et al., 2010), with intensity S_i for each emitted wavelength λ_e : in practice the spectrum can be written as $S_i(\lambda_e; [\text{Fe}/\text{H}]_i, t_i)$. We use the library of spectra modeled with a Chabrier IMF with slope 1.3 and BaSTI isochrones (Pietrinferni et al., 2013, Bag of Stellar Tracks and Isochrones). Other spectral libraries are easily configurable if needed. Depending on the redshift z and on the current line-of-sight velocity $V_{\text{los},i}$ of the particle, the spectrum should be Doppler shifted, obtaining the observed flux $F_i(\lambda)$:

$$F_i(\lambda) = \frac{S_i(\lambda_e(1+z+V_{\text{los},i}/c); [\text{Fe}/\text{H}]_i, t_i)m_i}{4\pi d}, \quad (6.1)$$

with $d = 20$ Mpc is the distance from the galaxy, equivalent to the Fornax cluster assumed distance and m_i the star particle mass.

After binning the wavelength dimension in $K = 10000$ channels j , for each frequency λ_j , at each spatial position (x, y) in the plane of the sky we compute the projected SPH interpolation along the z -axis of the observed spectra, producing a SPH map using eq. (2.19):

$$F(x, y, \lambda_j) = \sum_{i=0}^N \tilde{W}\left(\sqrt{(x-x_i)^2 + (y-y_i)^2}, h_i\right) F_i(\lambda_j), \quad (6.2)$$

where N is the number of star particles in the snapshot and (x_i, y_i) their projected position. Our tests have been carried out with a spatial grid of 80×80 spaxels.

Given the amount of frequency channels in the spectral library, we had to carefully optimize the routine to perform SPH projected interpolation. In fact, the code presented in the repository Mastropietro (2021) uses some PYNBODY (Pontzen et al., 2013) routines modified and optimized for spectral data, and heavily uses the SPECTRALCUBE tool (Ginsburg et al., 2014).

We then convolve each spaxel with the MUSE line spread function (LSF) (F_{udf10} , eq. (8) in Bacon et al., 2017). We finally add to the the datacube value a zero centered normal distributed contamination \mathcal{N} with dispersion σ :

$$F(x, y, \lambda_j) = F(x, y, \lambda_j) + \mathcal{N}(0, F(x, y, \lambda_j) \cdot \sigma) \quad (6.3)$$

We defined the contamination dispersion as the dispersion of the residuals of the fit for a typical galaxy (from Bidaran et al. (2020) dataset we take the VCC 1836 bin #70 with initial $S/N = 3$ and target $S/N = 40$). This resulted in a dispersion of $\sigma = 0.073$. Eventually, we create the STAT HDU in the datacube using DER_SNR algorithm (Stoehr et al., 2008). The noise model chosen in this stage is wavelength independent.

Bibliography

- Abramson A., Kenney J. D., 2014, AJ, 147, 63
- Bacon R., et al., 2010, in Ground-based and Airborne Instrumentation for Astronomy III. SPIE, p. 773508, doi:10.1117/12.856027, <https://ui.adsabs.harvard.edu/abs/2010SPIE.7735E..08B/abstract>
- Bacon R., et al., 2017, A&A, 608, A1
- Bate M. R., Burkert A., 1997, MNRAS, 288, 1060
- Bidaran B., et al., 2020, MNRAS, 497, 1904
- Binggeli B., Tarenghi M., Sandage A., 1990, A&A, 228, 42
- Binney J., Tremaine S., 2008, Galactic Dynamics: Second Edition. Princeton University Press, Princeton, NJ U
- Bishop C. M., Svensén M., Williams C. K. I., 1998, Neural Computation, 10, 215
- Borrow J., 2019, SPHERIC 2019
- Borrow J., Schaller M., Bower R. G., Schaye J., 2020, Sphenix: Smoothed particle hydrodynamics for the next generation of galaxy formation simulations (arXiv:2012.03974)
- Boselli A., Gavazzi G., 2006, PASP, 118, 517
- Boselli A., Boissier S., Cortese L., Gavazzi G., 2008, ApJ, 674, 742
- Bullock J. S., Boylan-Kolchin M., 2017, Annual Review of Astronomy and Astrophysics, 55, 343
- Bureau M., Mould J. R., Staveley-Smith L., 1996, ApJ, 463, 60
- Calura F., Bellazzini M., D'Ercole A., 2020, MNRAS, 499, 5873
- Canducci M., Tiňo P., Mastropietro M., 2022, Artificial Intelligence, 302, 103579
- Carleton T., Errani R., Cooper M., Kaplinghat M., Peñarrubia J., Guo Y., 2018, MNRAS, 485, 382
- Cellone S. A., Forte J. C., 1997, AJ, 113, 1239
- Chabrier G., 2003, PASP, 115, 763
- Chanamé J., Infante L., Reisenegger A., 2000, ApJ, 530, 96

Bibliography

- Cloet-Osselaer A., De Rijcke S., Schroyen J., Dury V., 2012, MNRAS, 423, 735
- Cloet-Osselaer A., De Rijcke S., Vandenbroucke B., Schroyen J., Koleva M., Verbeke R., 2014, MNRAS, 442, 2909
- Conselice C. J., 2003, ApJS, 147, 1
- Cooray A., Milosavljević M., 2005, ApJ, 627, L89
- Cortese L., Hughes T. M., 2009, MNRAS, 400, 1225
- Cortese L., et al., 2007, MNRAS, 376, 157
- De Looze I., Baes M., Bendo G. J., Cortese L., Fritz J., 2011, MNRAS, 416, 2712
- De Rijcke S., Van Hese E., Buyle P., 2010, ApJ, 724, L171
- De Rijcke S., Schroyen J., Vandenbroucke B., Jachowicz N., Decroos J., Cloet-Osselaer A., Koleva M., 2013, MNRAS, 433, 3005
- Di Cintio A., Brook C. B., Dutton A. A., Macciò A. V., Obreja A., Dekel A., 2017, MNRAS, 466, L1
- Dolag K., Reinecke M., Gheller C., Imboden S., 2008, New Journal of Physics, 10, 125006
- Dressler A., 1980, ApJ, 236, 351
- Dressler A., et al., 1997, ApJ, 490, 577
- Drinkwater M. J., Gregg M. D., Colless M., 2001, ApJ, 548, L139
- Easton R. L., 2010, Fourier Methods in Imaging, John Wiley & Sons, Ltd, Chichester, UK, doi:10.1002/9780470660102, <http://doi.wiley.com/10.1002/9780470660102>
- Ebeling H., Stephenson L. N., Edge A. C., 2014, ApJL, 781, L40
- Efstathiou G., 1992, MNRAS, 256, 43P
- Einasto J., 2010, Dark Matter (arXiv:0901.0632)
- Emsellem E., et al., 2007, MNRAS, 379, 401
- Emsellem E., et al., 2011, MNRAS, 414, 888
- Faucher-Giguère C. A., Lidz A., Zaldarriaga M., Hernquist L., 2009, ApJ, 703, 1416
- Geha M., Blanton M. R., Yan R., Tinker J. L., 2012, ApJ, 757, 85
- Gentile G., Salucci P., Klein U., Vergani D., Kalberla P., 2004, MNRAS, 351, 903
- Georgiev I. Y., Hilker M., Puzia T. H., Chanamé J., Mieske S., Goudfrooij P., Reisenegger A., Infante L., 2006, A&A, 452, 141

- Gingold R., Monaghan J., 1977a, MNRAS, 181, 375
- Gingold R. A., Monaghan J. J., 1977b, MNRAS, 181, 375
- Ginsburg A., Robitaille T., Beaumont C., ZuHone J., 2014, SpectralCube, doi:10.5281/zenodo.591639, <https://doi.org/10.5281/zenodo.591639>
- Gott III J. R., Jurić M., Schlegel D., Hoyle F., Vogeley M., Tegmark M., Bahcall N., Brinkmann J., 2005, ApJ, 624, 463
- Graf B., 2008, Quaternions and dynamics (arXiv:0811.2889)
- Gresho P. M., Chan S. T., 1990, Int. J. Numer. Methods Fluids, 11, 621
- Grossi M., 2018, Proc. Int. Astron. Union, 14, 319
- Gunn J. E., Gott J. R. I., 1972, ApJ, 176, 1
- Hamilton W. R., 1866, Elements of Quaternions. Cambridge University Press, Cambridge, doi:10.1017/CBO9780511707162, <http://ebooks.cambridge.org/ref/id/CBO9780511707162>
- Harris C. R., et al., 2020, Nature, 585, 357
- Hausammann L., Revaz Y., Jablonka P., 2019, A&A, 624, A11
- Heng K., 2014, Am. Sci., 102, 174
- Herrera-Camus R., et al., 2015, ApJL, 800, 1
- Hilker M., Bomans D. J., Infante L., Kissler-Patig M., 1997, A&A, 327, 562
- Huang K., 1987, Statistical Mechanics, second edn. Wiley and Sons
- Hubble E. P., 1929, ApJ, 69, 103
- Hunter D. A., Elmegreen B. G., 2004, AJ, 128, 2170
- Ibarra-Medel H. J., Avila-Reese V., Sánchez S. F., González-Samaniego A., Rodríguez-Puebla A., 2019, MNRAS, 483, 4525
- Iodice E., et al., 2016, ApJ, 820, 42
- Jeans J. H., 1902, Philos. Trans. R. Soc. London, 199, 1
- Karachentseva V. E., Karachentsev I. D., Sharina M. E., 2010, Astrophysics, 53, 462
- King I., 1962, AJ, 67, 471
- Koch A., Burkert A., Rich R. M., Collins M. L. M., Black C. S., Hilker M., Benson A. J., 2012, ApJ, 755, L13
- Kohonen T., 1982, Biological Cybernetics 43(1), 59–69, 43, 59

Bibliography

- Koleva M., De Rijcke S., Zeilinger W. W., Verbeke R., Schroyen J., Vermeylen L., 2014, MNRAS, 441, 452
- Lambert J. C., 2012, in ASP Conference Series, Vol.461, Astronomical Data Analysis Software and Systems XXI. pp 897–900, <https://ascl.net/1110.008>
- Lebanon G., 2005, PhD thesis, Carnegie Mellon University, Pittsburgh, PA, USA
- Lee-Waddell K., et al., 2018, MNRAS, 474, 1108
- Lee B., et al., 2017, MNRAS, 466, 1382
- Lisker T., Glatt K., Westera P., Grebel E. K., 2006, AJ, 132, 2432
- Loni A., et al., 2021, A&A, 648
- Lotz J. M., Primack J., Madau P., 2004, AJ, 128, 163
- Lucy L. B., 1977, AJ, 82, 1013
- MUSE Consortium 2021, ESO - MUSE, <https://www.eso.org/sci/facilities/paranal/instruments/muse.html>
- Maio U., Dolag K., Ciardi B., Tornatore L., 2007, MNRAS, 379, 963
- Mancera Pina P. E., Aguerri J. A., Peletier R. F., Venhola A., Trager S., Choque Challapa N., 2019, MNRAS, 485, 1036
- Mastropietro M., 2021, simifucube, doi:10.5281/zenodo.4975355, <https://doi.org/10.5281/zenodo.4975355>
- Mastropietro C., Moore B., Mayer L., Debattista V. P., Piffaretti R., Stadel J., 2005, MNRAS, 364, 607
- Mastropietro M., De Rijcke S., Peletier R. F., 2021, MNRAS, 504, 3387
- Mayer L., Governato F., Colpi M., Moore B., Quinn T., Wadsley J., Stadel J., Lake G., 2001, ApJ, 559, 754
- Mayer L., Mastropietro C., Wadsley J., Stadel J., Moore B., 2006, MNRAS, 369, 1021
- Mayer L., Kazantzidis S., Mastropietro C., Wadsley J., 2007, Nature, 445, 738
- McConnachie A. W., 2012, AJ, 144, 4
- Monaghan J. J., 1985, J. Comput. Phys., 60, 253
- Monaghan J. J., 2005, Reports Prog. Phys., 68, 1703
- Mora M. D., Chanamé J., Puzia T. H., 2015, AJ, 150, 93
- Mori M., Burkert A., 2000, ApJ, 538, 559
- Navarro J. F., Steinmetz M., 1997, ApJ, 478, 13

- Navarro J. F., Frenk C. S., White S. D. M., 1996, ApJ, 490, 493
- Nichols M., Revaz Y., Jablonka P., 2015, A&A, 582, A23
- Noh W. F., 1987, J. Comput. Phys., 72, 78
- Owers M. S., et al., 2019, ApJ, 873, 52
- Paolillo M., Fabbiano G., Peres G., Kim D., 2002, ApJ, 565, 883
- Papastergis E., Shankar F., 2016, A&A, 591
- Parzen E., 1962, The annals of mathematical statistics, 33, 1065
- Pearson K., 1901, The London, Edinburgh, and Dublin Philosophical Magazine and Journal of Science, 2, 559
- Pietrinferni A., Cassisi S., Salaris M., Hidalgo S., 2013, A&A, 558, 46
- Pillepich A., et al., 2018, MNRAS, 473, 4077
- Pillepich A., et al., 2019, MNRAS, 490, 3196
- Planck Collaboration et al., 2016, A&A, 594, A13
- Plummer H. C., 1911, MNRAS, 71, 460
- Poggianti B. M., et al., 2017, ApJ, 844, 48
- Poggianti B. M., et al., 2019, ApJ, 887, 155
- Pontzen A., Roškar R., Stinson G., Woods R., 2013, Astrophysics Source Code Library, ascl:1305.002
- Press W. H., Schechter P., 1974, ApJ, 187, 425
- Price D. J., 2012, J. Comput. Phys., 231, 759
- Ramatsoku M., et al., 2020, A&A, 640, A22
- Reback J., et al., 2020, pandas-dev/pandas: Pandas 1.0.3, doi:10.5281/zenodo.3715232
- Revaz Y., et al., 2009, A&A, 501, 189
- Riess A. G., et al., 1998, AJ, 116, 1009
- Rodriguez-Gomez V., et al., 2019, MNRAS, 483, 4140
- Roediger E., Brüggen M., 2008, MNRAS, 388, L89
- Roediger E., et al., 2015, ApJ, 806, 104
- Roman J., Trujillo I., 2017, MNRAS, 468, 703

Bibliography

- Rong Y., Mancera Pina P. E., Tempel E., Puzia T. H., Rijcke S. D., 2020a, MNRAS, 498, L72
- Rong Y., et al., 2020b, ApJ, 899, 78
- Ruggiero R., Lima Neto G. B., 2017, MNRAS, 468, 4107
- Ryden B., 2003, Introduction to cosmology. Addison Wesley, San Francisco
- Saifollahi T., Trujillo I., Beasley M. A., Peletier R. F., Knapen J. H., 2021, MNRAS, 502, 5921
- Sales L. V., Navarro J. F., Peñafiel L., Peng E. W., Lim S., Hernquist L., 2021, MNRAS, 494, 1848
- Sandage A., Binggeli B., 1984, AJ, 89, 919
- Schmidt M., 1959, ApJ, 129, 243
- Schoenberg I. J., 1946, Quarterly of Applied Mathematics, 4, 45
- Schröder A., Drinkwater M. J., Richter O.-G., 2001, A&A, 376, 98
- Schroyen J., de Rijcke S., Valcke S., Cloet-Osselaer A., Dejonghe H., 2011, MNRAS, 416, 601
- Schroyen J., De Rijcke S., Koleva M., Cloet-Osselaer A., Vandenbroucke B., 2013, MNRAS, 434, 888
- Schulze F., Remus R. S., Dolag K., Burkert A., Emsellem E., van de Ven G., 2018, MNRAS, 480, 4636
- Scott N., et al., 2018, MNRAS, 481, 2299
- Sedov L., 1946, Prikl. Mat. Mekh, 10, 241
- Sivanandam S., Rieke M. J., Rieke G. H., 2014, ApJ, 796, 89
- Smith R. J., et al., 2010, MNRAS, 408, 1417
- Smith R., et al., 2015, MNRAS, 454, 2502
- Springel V., 2005, MNRAS, 364, 1105
- Springel V., 2010, MNRAS, 401, 791
- Springel V., 2015, in Revaz Y., ed., Star Formation in Galaxy Evolution: Connecting Numerical Models to Reality: Saas-Fee Advanced Course 43. Swiss Society for Astrophysics and Astronomy. Springer, Heidelberg, pp 251–358 (arXiv:1412.5187), doi:10.1007/978-3-662-47890-5_3
- Steinhauser D., Schindler S., Springel V., 2016, A&A, 591, A51

Bibliography

- Stevens A. R. H., Diemer B., Lagos C. d. P., Nelson D., Obreschkow D., Wang J., Marinacci F., 2019, MNRAS, 490, 96
- Steyrleithner P., Hensler G., Boselli A., 2020, MNRAS, 494, 1114
- Stinson G., Seth A., Katz N., Wadsley J., Governato F., Quinn T., 2006, MNRAS, 373, 1074
- Stobie R. S., 1980, in Elliot D. A., ed., Proceedings of SPIE Vol. 0264, Applications of Digital Image Processing to Astronomy. SPIE, pp 208–212, doi:10.1117/12.959806
- Stoehr F., et al., 2008, in Astronomical Data Analysis Software and Systems XVII. p. 505, <https://ui.adsabs.harvard.edu/abs/2008ASPC..394..505S/abstract>
- Stott J. P., Smail I., Edge A. C., Ebeling H., Smith G. P., Kneib J., Pimbblet K. A., 2007, ApJ, 661, 95
- Ströger L.-G., et al., 2004, ApJ, 613, 200
- Su A. H., et al., 2021, A&A, 647, A100
- Taylor E. N., et al., 2011, MNRAS, 418, 1587
- The Astropy Collaboration et al., 2018, AJ, 156, 123
- Toloba E., et al., 2014, Astrophysical Journal, Supplement Series, 215, 17
- Toloba E., et al., 2015, ApJ, 799, 172
- Tolstoy E., Hill V., Tosi M., 2009, Annual Review of Astronomy and Astrophysics, 47, 371
- Valcke S., De Rijcke S., Dejonghe H., 2008, MNRAS, 389, 1111
- Van Dokkum P. G., Abraham R., Merritt A., Zhang J., Geha M., Conroy C., 2015, ApJL, 798, 45
- Vandenbroucke B., 2016, PhD thesis, Ghent University, <https://biblio.ugent.be/publication/7212143>
- Vandenbroucke B., De Rijcke S., 2016, Astron. Comput., 16, 109
- Vandenbroucke B., De Rijcke S., Schroyen J., Jachowicz N., 2013, ApJ, 771
- Vazdekis A., Sánchez-Blázquez P., Falcón-Barroso J., Cenarro A. J., Beasley M. A., Cardiel N., Gorgas J., Peletier R. F., 2010, MNRAS, 404, 1639
- Venhola A., et al., 2017, A&A, 608, A142
- Venhola A., et al., 2018, A&A, 620, A165
- Venhola A., et al., 2019, A&A, 625, A143
- Verbeke R., Vandenbroucke B., De Rijcke S., 2015, ApJ, 815

Bibliography

- Verbeke R., Papastergis E., Ponomareva A. A., Rathi S., De Rijcke S., 2017, A&A, 607, A13
- Virtanen P., et al., 2020, Nature Methods, 17, 261
- Vogelsberger M., et al., 2014, Nature, 509, 177
- Walo-Martín D., Falcón-Barroso J., Dalla Vecchia C., Pérez I., Negri A., 2020, MNRAS, 494, 5652
- Wang X., Tiño P., Fardal M. A., 2008, in Daelemans W., Goethals B., Morik K., eds, Machine Learning and Knowledge Discovery in Databases. Springer Berlin Heidelberg, Berlin, Heidelberg, pp 566–581
- Wang X., Tino P., Fardal M. A., Raychaudhury S., Babul A., 2009, in 2009 International Joint Conference on Neural Networks. pp 3267–3274, doi:10.1109/IJCNN.2009.5178637
- Wang J., Koribalski B. S., Serra P., van der Hulst T., Roychowdhury S., Kamphuis P., Chengalur J. N., 2016, MNRAS, 460, 2143
- Wang J., Xu W., Lee B., Du M., Overzier R., Shao L., 2020, ApJ, 903, 103
- Wechsler R. H., Bullock J. S., Primack J. R., Kravtsov A. V., Dekel A., 2002, ApJ, 568, 52
- Weinberger R., Springel V., Pakmor R., 2019, ApJ, 248, 32
- Wolf J., Martinez G. D., Bullock J. S., Kaplinghat M., Geha M., Muñoz R. R., Simon J. D., Avedo F. F., 2010, MNRAS, 406, 1220
- Wongwathanarat A., Janka H.-T., Müller E., Pllumbi E., Wanajo S., 2017, ApJ, 842, 13
- Wu S., Bertholet P., Huang H., Cohen-Or D., Gong M., Zwicker M., 2018, IEEE Transactions on Pattern Analysis and Machine Intelligence, 40, 2529
- Yagi M., Koda J., Komiyama Y., Yamanoi H., 2016, ApJS, 225, 11
- Yun K., et al., 2019, MNRAS, 483, 1042
- Zabel N., et al., 2019, MNRAS, 483, 2251
- Zehavi I., et al., 2011, ApJ, 736, 59
- Zwicky F., 1933, Helvetica Physica Acta, 6, 110
- Zwicky F., 1937, ApJ, 86, 217